AD-A035 775 STANFORD UNIV CALIF INST FOR PLASMA RESEARCH F/G 3/2
THERMAL INSTABILITY IN POST-FLARE PLASMAS.(U)
DEC 76 S K ANTIOCHOS N00014-75-C-0673
UNCLASSIFIED SU-IPR-679 NL

1 OF 2
AD A035775

(6) THERMAL INSTABILITY IN POST-FLARE PLASMAS.

by

(10) Spiro K. Antiochos*

(9) Technical rept.,

National Aeronautics and Space Administration

Grant NGL-05-020-272

Office of Naval Research

(15) Contract N00014-75-C-0673
✓NGL-05-020-272

(14) SUIPR Report No. 679

(11) December 1976

(12) 121 p.

Institute for Plasma Research
Stanford University
Stanford, California

*Also Department of Applied Physics

ACCESSION for
NTIS White Section
DDC Buff Section
UNANNOUNCED
JUSTIFICATION
BY
DISTRIBUTION/AVAILABILITY CODES
Dist. AVAIL. and/or SPECIAL
A

1473

332 630

AB

ABSTRACT

Satellite x-ray observations indicate that most solar flares produce a hot, $\geq 10^7$ K, dense plasma high up in the sun's corona. We believe that this gas originates from lower regions of the atmosphere, specifically the chromosphere, where it is heated by a flare and evaporated into the corona. Optical observations have shown that the post-flare plasma does not cool uniformly rather, small cold condensations form at the top of magnetic field arches while the bulk of the plasma remains at high temperature. Loop Prominence Systems are an example of this phenomenon. Dynamical processes connected with the flare event have been proposed as a mechanism for these types of active prominences.

We have investigated the cooling of post-flare plasmas, and attempted to explain the formation of loop prominences as due to a thermal instability. At temperatures between 10^5 to 10^7 K, the solar plasma is known to be unstable to thermal perturbations because the radiation losses of this gas increase with decreasing temperature. A simple perturbation analysis is insufficient to account for the evolution of the solar plasma, because observed differences of temperature and density exceed an order of magnitude. Additionally, the plasma is always in a non-equilibrium state, so that, we must solve numerically the equations of motion and heat transfer.

We have developed a one-dimensional model for active loop prominences. Magnetic fields present in post-flare regions are strong

PRECEDING PAGE BLANK-NOT FILMED

enough to dominate the plasma; hence, only motion and heat fluxes parallel to the field need to be considered. The relevant size scales and time scales are such that single-fluid MHD equations are valid. We have included in the model the effects of gravity, the geometry of the field and conduction losses to the chromosphere. A computer code for the solution of our set of equations has been constructed. Basically, we treat the system as an initial value problem (with certain boundary conditions at the chromosphere-corona transition region), and use a two-step time differencing scheme.

Our calculations indicate that the thermal instability mechanism is, by itself, sufficient to account for the behavior of active loop prominences. Under certain conditions, initial perturbations in the temperature and density profiles of small amplitude ($\leq 5\%$) and large size scale ($\geq 2 \times 10^9$ cm.) can grow into condensations with temperature and density differences of over an order of magnitude and size scales of less than 10^8 cm. In agreement with observations, the conditions that must be satisfied are such that Loop Prominence Systems are likely to occur only in large flares. The velocities, densities, and lifetimes that we obtain for the loop material are also in agreement with observations.

From our results we conclude that the non-uniform cooling of the post-flare corona can be understood as a direct consequence of the temperature and density dependence of the radiative losses from a high-temperature solar plasma.

ACKNOWLEDGMENTS

For supporting and directing my research and for critically reading this dissertation, I would like to thank Professor Peter A. Sturrock. I am also grateful to Professors Vahé Petrosian and Arthur Walker for reading and commenting on the thesis, and to Joshua Knight, Charles Newman and Ron Moore for helpful discussions during the course of this work.

Special thanks are due to Mrs. Chris Garner for her careful typing of the manuscript and for her personal help and encouragement; this dissertation is the first for both of us.

In addition, I wish to thank Mary Ellen Shields for sage advice and moral support.

Finally, I gratefully acknowledge financial support for this research from the National Aeronautics and Space Administration under Grant NGL 05-020-272 and the Office of Naval Research under Contract N00014-75-C-0673.

CONTENTS

		Page
1.	THERMAL INSTABILITY	1
	1.1 Introduction	1
	1.2 Linear Theory	4
2.	POST-FLARE REGIONS	9
	2.1 Solar Prominences	9
	2.2 Description of the Post-Flare Corona	10
	2.2.1 Magnetic Field	10
	2.2.2 Temperature	11
	2.2.3 Density	12
	2.2.4 Morphology of Loop Prominences	13
	2.3 Theories of Loop Prominence Systems	14
	2.3.1 Compression-Condensation Model	14
	2.3.2 Fast Particle Model	15
	2.3.3 Flare Evaporation Model	16
3.	MODEL OF A LOOP PROMINENCE	18
	3.1 Introduction	18
	3.2 Single-Fluid Assumption	18
	3.3 Radiative Losses	19
	3.4 MHD Equations	21
	3.5 Magnetic Field Structure	24
	3.6 One-Dimensional Equations	28
4.	NUMERICAL METHODS	31
	4.1 Introduction	31
	4.2 Boundary and Initial Conditions	33
	4.3 Shocks	39
	4.4 Computer Code	41
5.	COOLING OF FLARE LOOPS	47
	5.1 General Evolution of Loops	47

Page

5.2 Conductive Cooling Stage 50
5.2.1 Conductive Damping Rate 50
5.2.2 Static and Evaporative Cooling Rates 53
5.3 Instability Criteria 56
5.4 Radiative Cooling Stage 58
5.4.1 Comparison with Linear Theory 58
5.4.2 Analytic Model of a Condensation 62
5.4.3 Evolution of a Condensation 75
5.4.4 Effect of Perturbation Amplitude 82
5.5 Post-Cooling Stage 86

6. DISCUSSION 93

6.1 Comparison with Observations 93
6.2 Conclusions 96

Appendix A. FLUID EQUATIONS FOR A DIPOLE LOOP 98

Appendix B. FINITE DIFFERENCE EQUATIONS 103

REFERENCES 108

ILLUSTRATIONS

Figure		Page
1.1	Temperature dependence of the radiative losses from a low density solar plasma (from Cox and Tucker, 1969)	3
3.1	Geometry of our model loop	27
5.1	Evolution of the amplitude of a temperature and density perturbation that is damped by conduction . .	51
5.2	Comparison of analytic conductive cooling model with our numerical results. Plot of $(T/T_o)^{-5/2} - 1$ versus t	55
5.3	Graph of instability criteria, (2) and (3), and graph of temperature of instability onset, T_c, computed from our model	59
5.4	Geometry of our analytic condensation model	63
5.5	Evolution of the temperature ratio, ξ, for various α	69
5.6	Velocity of the condensation boundary as a function of ξ for various α	72
5.7	Temperatures of the hot, T_h, and cold, T_c, plasma as a function of ξ	73
5.8	Temperature profile of an "unstable" loop at various times in its evolution	77
5.9	Density profile of an "unstable" loop at various times in its evolution	78
5.10	Temperature profile of a "stable" loop at various times in its evolution	83
5.11	Density profile of a "stable" loop at various times in its evolution	84
5.12	Velocity profiles of a "stable" and an "unstable" loop at various times in their evolution	88
5.13	Density profile of an "unstable" loop at various times in the post-cooling phase of its evolution . .	90

Figure		Page
5.14	Density in an unstable loop as a function of Lagrangean coordinate, x , at the time when the condensation density is maximum	91
A.1	Profiles of the area of a loop due to a dipole source and of the component of gravity parallel to the loop	102

1. THERMAL INSTABILITY

1.1 Introduction

Parker (1953) first introduced the concept of thermal instability to explain the formation of cold condensations, $T \leq 10^4$ K, in the hot solar corona, $T \geq 10^6$ K (Tandberg-Hanssen, 1967). He examined the stability of a hydrogen plasma to a thermal perturbation and deduced that if the total energy losses minus energy gains decrease with T, then the plasma would be unstable. This is because a region slightly cooler than its surroundings will lose energy faster than the surroundings and, therefore, temperature differences will increase.

Parker also noted that there is a temperature range over which the radiation losses of an optically thin hydrogen plasma decrease with temperature. This is the temperature range over which the state of ionization of hydrogen changes rapidly, $10^4 \leq T \leq 10^5$. The emission is dominated by line and recombination radiation for these temperatures. Above this range, the emission is due mainly to free-free transitions; hence,

$$\mathcal{L} \propto n^2 T^{1/2} \quad , \tag{1.1}$$

where $\mathcal{L}$ is the radiative loss rate (Karzas and Latter, 1961). Below 10^4 K, the mean kinetic energy per particle is insufficient to excite neutral hydrogen above its ground state, and the emission decreases exponentially with decreasing T.

Defouw (1970b) has calculated the radiation from a model hydrogen plasma. He concludes that hydrogen is thermally unstable above 17,500 K. Thomas and Athay (1961) find that the solar chromosphere is unstable above

12,000 K. Cox and Tucker (1969) (Figure 1.1), Cox and Daltabuit (1971), Tucker and Koren (1971) and Raymond et al. (1976) have calculated the total radiation losses (including heavy elements), for the solar coronal plasma. From Figure 1.1 we note that there is a region, $10^5 \leq T \leq 10^7$, over which Λ decreases with T; hence, thermal instability is possible.

The original treatment of thermal instability by Parker (1953) was faulty because he did not take into account the dynamics of the plasma. Field (1965) in his excellent paper on the subject thoroughly analyzed the linear growth of thermal perturbations in a fully-ionized plasma. He not only included the dynamics, but also analyzed in detail effects due to conduction, magnetic fields, gravity, expansion and rotation. Goldsmith (1970) and Defouw (1970a,b,c) extended Field's results to include ionization effects and Hunter (1970) investigated thermal instability in a plasma with an arbitrary velocity profile.

We will deal only with thermal instability in post-flare coronal loops. The important effects in this case are due to conduction and magnetic fields. Since the field dominates the plasma, we need only consider the growth of instabilities in one dimension, along the field (Section 3.4). Field has derived the growth rates for plasma in a uniform magnetic field; however, solar fields are far from uniform (Harvey et al., 1972; Rust and Bar, 1973). This means that a constant flux tube in the solar corona will have a large change in cross-sectional area along its length. Hence, we derive below the growth equation (dispersion relation) for thermal perturbation in a loop of varying area, A(s). From the dispersion relation we can obtain criteria for a post-flare loop to be susceptible to thermal instability.

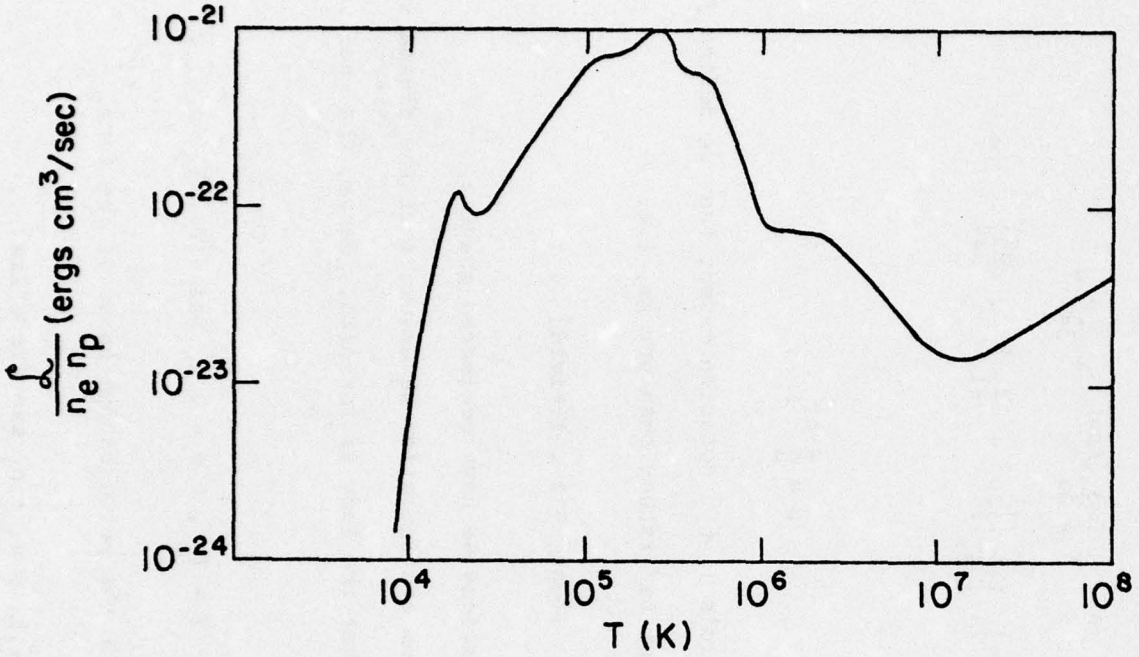

Figure 1.1 TEMPERATURE DEPENDENCE OF THE RADIATIVE LOSSES FROM A LOW DENSITY SOLAR PLASMA (Cox and Tucker, 1969).

1.2 Linear Theory

The basic equations for fully-ionized plasma in a flux tube are discussed in Section 3.4 and Appendix A. They are:

$$\frac{\partial}{\partial t}\rho + \frac{1}{A}\frac{\partial}{\partial s}(A\rho v) = 0 \quad , \tag{1.2}$$

$$\frac{\partial}{\partial t}(\rho v) + \frac{1}{A}\frac{\partial}{\partial s}(A\rho v^2) + \frac{\partial}{\partial s}p = 0 \quad , \tag{1.3}$$

$$\frac{\partial}{\partial t}\left(\frac{1}{2}\rho v^2 + \frac{p}{\gamma-1}\right) + \frac{1}{A}\frac{\partial A}{\partial s}\left(\frac{1}{2}\rho v^3 + \frac{\gamma}{\gamma-1}pv - \kappa\frac{\partial T}{\partial s}\right) + \mathcal{L} = 0 \tag{1.4}$$

and

$$p = \frac{R}{\mu}\rho T \quad , \tag{1.5}$$

where we have used Field's (1965) notation except that we define $\mathcal{L}$ as the energy loss rate per cm^3 rather than per gm, i.e.

$$\mathcal{L}(\text{our}) \equiv \rho \cdot \mathcal{L}(\text{Field}) \quad . \tag{1.6}$$

Note that in these equations we have neglected gravity.

For the equilibrium configuration we assume that the plasma is static and homogeneous, and that the loop is infinite. Hence, the equilibrium state is given by,

$$\rho = \rho_0 \ , \quad T = T_0 \ , \quad v = 0 \ , \quad \text{and } \mathcal{L}(\rho_0, T_0) = 0 \quad . \tag{1.7}$$

Following Field, we take the perturbation to be of the form,

$$\rho(s,t) = \rho_0 + \rho_1 \exp(\eta t + iks) \quad . \tag{1.8}$$

For simplicity we assume that the area is given by,

$$A(s) = A_0 \exp(k_A s) , \quad k_A = \text{const.} \tag{1.9}$$

Substituting the form (1.8) into equations (1.2) - (1.5), we obtain to first order:

$$\begin{pmatrix} \eta & (ik + k_A)\rho_0 & 0 & 0 \\ 0 & \eta\rho_0 & ik & 0 \\ \mathcal{L}_\rho & \frac{\gamma}{\gamma-1}(ik + k_A)p_0 & \frac{\eta}{\gamma-1} & \mathcal{L}_T + \kappa_0 k_1^2 \\ \frac{-1}{\rho_0} & 0 & \frac{1}{p_0} & \frac{-1}{T_0} \end{pmatrix} \begin{pmatrix} \rho_1 \\ v_1 \\ p_1 \\ T_1 \end{pmatrix} = 0 , \tag{1.10}$$

where

$$k_1^2 = k(k - ik_A) , \tag{1.11}$$

and

$$\mathcal{L}_\rho \equiv \frac{\partial}{\partial\rho}\mathcal{L}(\rho,T) , \quad \mathcal{L}_T \equiv \frac{\partial}{\partial T}\mathcal{L}(\rho,T) . \tag{1.12}$$

The dispersion relation is obtained from the requirement that the determinant of the coefficient matrix in equation (1.10) vanishes.

As pointed out by Field, the dispersion relation has three solutions: one mode corresponding to isobaric condensations and the other two corresponding to the growth of sound waves. In this paper we will only be interested in the growth of condensations. We note from equation (1.3) that if the speed of sound is large so that the acceleration term is negligible, then we can replace the term $(\eta\rho_0)$ in the second row of equation (1.10) by zero. This corresponds to the case of

isobaric condensations. Therefore, to isolate cases, we expand the determinant of the coefficient matrix about the second row, yielding:

$$-\eta^2\rho\left(\frac{\eta}{(\gamma-1)T}+\frac{\mathcal{L}_T+\kappa k_1^2}{p}\right)-\frac{\eta\gamma p k_1^2}{(\gamma-1)T}-k_1^2\rho\left(-\frac{\mathcal{L}_\rho}{T}+\frac{\mathcal{L}_T+\kappa k_1^2}{\rho}\right)=0\ , \quad (1.13)$$

where we have dropped the subscript "0". The first term in (1.13) is the contribution due to the acceleration term in the force equation. If this vanishes then the dispersion relation reduces to

$$\eta\left(\frac{\gamma p}{(\gamma-1)T}\right)=\frac{\rho\mathcal{L}_\rho}{T}-\mathcal{L}_T-\kappa k_1^2\ . \quad (1.14)$$

For instability, we need the real part of η to be positive. From equations (1.11) and (1.14), $R_e(\eta) > 0$ implies

$$\mathcal{L}_T-\frac{\rho}{T}\mathcal{L}_\rho<-\kappa k^2\ . \quad (1.15)$$

Equation (1.15) is identical to the one derived by Field (1965). The addition of a variable area has no effect on the growth of condensations other than to add an oscillatory factor to the time dependence. If conduction is negligible, then equation (1.15) reduces to

$$\frac{\partial\mathcal{L}}{\partial T}-\frac{\rho}{T}\frac{\partial\mathcal{L}}{\partial\rho}<0\ . \quad (1.16)$$

This relation was originally derived by Weymann (1960). Note that Parker's simpler condition, $\mathcal{L}_T < 0$, implies that the radiative loss function for free-free emission, equation (1.1), is stable; whereas, under condition (1.16) it is unstable. However, we find that in the corona, whenever the temperature is high enough so that bremsstrahlung dominates the radiation losses, the conductivity is usually so large that condition (1.15) implies stability.

We note from equation (1.15) that the effect of conduction is to increase the thermal stability of the plasma. This is to be expected, since conduction always acts to reduce temperature differences. For given values of n and T, equation (1.15) implies that there exists a maximum wavenumber, k_c, such that perturbations of larger wavenumber are damped by conduction. Letting

$$\lambda_c = 2\pi/k_c \tag{1.17}$$

and using the Cox and Tucker (1969) form for the cooling function,

$$\mathcal{L} = n^2\Lambda(T) \quad , \tag{1.18}$$

where $\Lambda \propto T^{-\alpha}$, and α is of order unity, we obtain for λ_c,

$$\lambda_c \approx 2\pi\sqrt{\frac{KT}{3n^2\Lambda}} \quad . \tag{1.19}$$

Hence, one of the criteria that a perturbation must satisfy in order for it to grow is that

$$\lambda \geq \lambda_c \quad . \tag{1.20}$$

Equation (1.19) provides a lower limit on the wavelength of an unstable perturbation. Field noted that the dispersion relation (1.13) also implies an upper limit on the wavelength of an unstable <u>density</u> perturbation. This is because the growth rate of a density perturbation cannot be faster than the speed of sound travel time across the perturbation;

$$\tau_s = 1/kc \quad . \tag{1.21}$$

Therefore, finite-speed-of sound effects will decrease the growth rate if the cooling time,

$$\tau_c \approx \frac{3}{2}\frac{p}{\mathcal{L}} \tag{1.22}$$

is less than τ_s. This implies another criterion on the wavelength of an unstable perturbation,

$$\lambda \leq \frac{3\pi pc}{n^2\Lambda} \ . \tag{1.23}$$

Note, however, that this restriction applies only to the growth of density perturbations. Temperature perturbations of arbitrary wavelength will grow on time scales of the cooling time as long as condition (1.20) is satisfied. In fact, we calculate in Section 5.4 that temperature variations in the post-flare corona grow at a much faster rate than density variations due to the finite speed of sound.

2. POST-FLARE REGIONS

2.1 Solar Prominences

Along with sunspots and flares, prominences are one of the most common manifestations of solar activity. In general, a prominence is simply a region of cold, dense plasma that is visible in Hα and is located at least partially in the corona. Since the corona usually has a temperature in excess of 10^6 K, there is over two orders of magnitude temperature difference between a prominence and its surroundings.

Prominences have a very wide range of morphology; however, it is possible to separate them into two categories: quiescent prominences which are large structures (size scales up to 10^{10} cm), that appear stable for months and occur in quiet regions; and active prominences which are short-lived events (lifetimes less than hours), and are believed to be flare related. (A thorough and detailed description of the observed properties of solar prominences is given by Tandberg-Hanssen (1974) in his book on the subject.) In this paper we will be interested mainly in active loop prominences. We include coronal rain and knots (Tandberg-Hanssen, 1974, p. 5) as part of this phenomenon.

Dodson (1961) first proposed that loop prominence systems are flare related events. A careful investigation of the association between loop prominence systems and flares was made by Bruzek (1964a). He concludes that they occur only after great flares and especially after flares that emit energetic protons (Bruzek, 1964b; Svestka, 1968). Teske (1971) found that loop prominence systems radiate in soft x-rays indicating that, in common with post-flare regions, they contain a high temperature plasma, $T \geq 10^7$ K. A similar observation was noted by Waldmeier (1973).

We believe that loop prominences are a direct result of thermal instability in hot, dense post-flare regions. They occur preferentially in these regions of the corona because the coronal density is greatly enhanced by a flare. The important features of flare regions and of loop prominences are briefly described in the following sections. A detailed description of the flare corona, including some of the recent Skylab data is available in the book by Svestka (1976).

2.2 Description of the Post-Flare Corona

2.2.1 Magnetic Field

The geometric structure of prominences and other features in the corona is almost wholly determined by the magnetic field. This is because the field is strong enough to prevent any mass or heat flow perpendicular to field lines (Section 3.4). Hence, temperature and density gradients perpendicular to the field tend to be much larger than those parallel. In addition, mass motion will be directed along field lines.

The observed geometry of the field is a loop or a series of loops; each loop is believed to represent a magnetic flux tube. This is true if a flare region is observed either in soft x-rays (Kahler et al., 1975; Vorpahl et al., 1975), or in Hα as a loop prominence system. The magnetic field strength in loop prominences appears to be large, as would be expected for flare regions. Zirin (1961) measured fields of up to 200 G, and Hyder (1964) obtained a value of 60 - 80 G for the field in a loop prominence. Similar values were observed by Roy (1972) and Rust and Bar (1973). Tandberg-Hanssen (1974, p. 43) estimates that the typical field in a loop prominence is from 20 - 100 G.

Several observers have compared the coronal field lines with those of a potential field computed from observations of the photospheric field, Rust and Roy (1971), Roy (1972) and Rust and Bar (1973). They find that the field in the post-flare corona can be well approximated as being potential, especially at large heights. This result is in agreement with the observation that the field in loop prominence systems is static. Bruzek (1964a) finds that individual loops do not alter their shape during the prominence event.

In summary, we find that the magnetic field in the post-flare corona is large, ~ 50 G, and appears to be current-free.

2.2.2 Temperature

Observations (Thomas and Teske, 1971) imply that all flares emit soft x-rays. The spectra of the soft x-ray bursts indicate that they are due to bremsstrahlung from a thermal plasma at temperatures $\geq 10^7$ K. Typically these bursts have rise times of order minutes and decay times of order tens of minutes. The peak in temperature is usually observed to occur before the peak in flux (Horan, 1971; Kahler et al., 1970), which implies that the density of the soft x-ray emitting plasma is rising while the temperature drops.

The dominant cooling mechanism for the hot coronal plasma is believed to be conduction to the chromosphere, Culhane et al. (1970), Moore and Datlowe (1975). A related process is the evaporation of chromospheric material. Although this has not been seen directly, it has been proposed by several observers as the mechanism by which the density in the flare corona is enhanced (Neupert, 1968; Hudson and Ohki, 1972; and Neupert et al., 1974).

The value of the temperature in flare regions is generally estimated either from the continuum or from lines in the soft x-ray spectrum. These measurements indicate that the maximum temperature is usually $(2-4) \times 10^7$ K, but that the flare corona is highly inhomogeneous (Neupert et al., 1974; Dere et al., 1974). This is not surprising since, if a flare region consists of several loops, adjacent loops are thermally insulated from one another by the magnetic field. In fact, observations indicate that loops of temperature $> 10^6$ K can be seen in the immediate vicinity of Hα loops, $T \sim 10^4$ K, (Fisher, 1971, 1974; McCabe, 1973). If conduction is indeed the dominant cooling process, then we can see that large temperature differences would naturally arise. Even if all the loops in a flare region were heated to the same initial temperature, small loops would cool before large ones since the conductive cooling rate varies as L^{-2}, where L is the loop length (Section 5.2.2).

2.2.3 Density

The density in soft x-ray emitting regions is not as accurately known as the temperature. From the observation of certain lines of highly ionized elements, e.g. Fe XXV, one can safely conclude that temperatures of at least 10^7 K are present; however, there does not seem to be any model independent method of obtaining values for the density. Part of the difficulty is that, like the temperature, there is no reason to expect a unique density for a post-flare region. From estimates of the emission measure, values for the density of $10^{10} - 10^{11}$ cm^{-3} are usually given, e.g. Cheng and Widing (1975). However, Craig and Brown (1976) point out that temperature inhomogeneities may lead to large errors in the deduced magnitudes of both

density and temperature. In general, one may say that from soft x-ray observations, n is at least 10^{10} cm^{-3} and may be as high as 10^{12} cm^{-3} in flare coronal regions (Svestka, 1976, p. 138).

In loop prominences visible in Hα the density may be more easily obtained because the plasma is usually optically thick in the hydrogen lines. From the Stark broadening of the Balmer lines, Hirayama (1972) obtains densities ranging from 10^{11} - 10^{12} cm^{-3}. Jefferies and Orrall (1961) use the scattering of photospheric light to calculate the electron density. They obtain a value of 2×10^{11} cm^{-3} in a loop prominence. In summary, we conclude that the density in Hα loops is measured to be $\geq 10^{11}$ cm^{-3}, while soft x-ray observations indicate that the density in a general post-flare region is $\geq 10^{10}$ cm^{-3}. Since loop prominence systems are only associated with large flares, it may well be that the higher value is more accurate for these particular flare regions.

2.2.4 Morphology of Loop Prominences

The evolution of a loop prominence system has been studied in detail by Bruzek (1964a). He finds that these systems first appear in Hα several minutes after flare onset as a low mound, heights $\leq 10^{9}$ cm. The system then evolves as a series of Hα loops appearing at successively higher heights reaching up to 1.5×10^{10} cm. The apparent rate of expansion of the system is of order a few km/sec; however, individual loops do not expand. The lifetime of a typical loop is approximately 30 minutes and the complete system may last well over 12 hours. Bruzek has observed certain systems lasting up to 3 successive days.

Individual loops generally appear to begin as a bright small knot at the top of the loop, although knots can sometimes form at the sides

as well (Bruzek and Kuperus, 1972). The knot then expands into a loop with material streaming down both legs. This part of the evolution is very similar to "coronal rain" (Tandberg-Hanssen, 1974, p. 29). The velocity of the material at the loop base is of order 10^2 km/sec, in agreement with free-fall velocities. The lifetime of a knot is of order 10 minutes; Bruzek and Kuperus (1972) quote 3 - 10 minutes, while Tandberg-Hanssen (1974, p. 5) states 15 minutes.

2.3 Theories of Loop Prominence Systems

2.3.1 Compression-Condensation Model

Although Parker (1953) originally proposed thermal instability as a mechanism for the formation of quiescent prominences, he discounted it as a possible explanation for active prominences because their lifetime is much smaller than the growth time of thermal perturbations at coronal densities, $\leq 10^9$ cm^{-3}. In addition, the size scale implied by equation (1.20) for coronal densities is much larger than active prominence size scales. Field's (1965) more exact analysis confirmed this result. Kleczek (1958) pointed out that if the coronal plasma were sufficiently compressed by magnetic fields, then the radiative cooling time may be decreased enough to agree with loop prominence time scales. Hence, a model based on an initial strong compression (from $n \approx 10^9$ cm^{-3} to $n \approx 10^{11}$ cm^{-3}) has been investigated by several authors: Kleczek (1958), Lust and Zirin (1960), Shklovskii (1965), Olson and Lykoudis (1967), and De (1973).

Several objections can be raised to this model. Jefferies and Orrall (1965b) pointed out that the amount of matter in a loop prominence system, $\sim 10^{16}$ gms, is too large to condense out of the corona, even in

a coronal condensation. Olson and Lykoudis (1967), themselves agree that the compression model cannot explain loops larger than $\sim 3 \times 10^9$ cm, while loops larger than 10^{10} cm have often been observed (Bruzek, 1964a). Teske (1971) argues that the compression model is not consistent with his observations of soft x-rays from loop prominence systems. Finally, this model requires large changes in the magnetic field in order to compress the plama. However, observations indicate that the field is static during a loop prominence event, in fact, several authors find that it is potential (Section 2.2.1). Therefore, we conclude from these arguments that the compression-condensation model is not a likely explanation for the formation of loop prominences.

2.3.2 Fast Particle Model

Jefferies and Orrall (1965a, 1965b) have proposed a model for loop prominence systems in which the prominence material is supplied by fast protons, $v_p \sim 10^8$ cm/sec. They argue that the large mass required for a loop system is stored as 10 keV protons on large loops extending into the outer corona. These particles are supposed to migrate down to lower field lines where they thermalize near the top of a loop to produce the bright knots that are observed.

The major objection to this proposal is that it is difficult to imagine how the protons can migrate across the field, and in such a way as to reproduce the evolution of a loop prominence system. Particles stored in the outer corona would have to migrate first down to the lowest loops and then to higher loops. Unless some mechanism whereby this may be done is proposed, the fast particle model cannot be truly evaluated.

2.3.3 Flare Evaporation Model

Goldsmith (1971) and Sturrock (1973) have proposed that the mass for a loop prominence system is due to chromospheric evaporation by flare heating. They argue that since soft x-ray observations indicate that the density in post-flare regions is greatly enhanced over usual coronal values, a loop prominence system may well be simply the final stage of the evolution of the dense flare corona. The appearance of loops at successively greater heights may be explained as due to the decrease in the conductive cooling rate with height.

The idea of chromospheric evaporation has another attractive feature in that one does not have to invoke magnetic field compression or other exotic mechanisms in order to obtain large enough densities for thermal instability to be effective. Goldsmith has calculated the response of a coronal loop to an isobaric perturbation in its initial temperature and density profile. He finds that for $T_0 = 5 \times 10^6$ K, and $n_0 = 10^{11}$ cm^{-3}, a 5% amplitude perturbation of wavelength, 3×10^9 cm does grow to produce temperature differences of over an order of magnitude. However, these large temperature differences last for only ≤ 100 sec, which is small compared to the lifetime of knots, ~ 10 minutes. In addition, his calculations do not include effects due to gravity, conduction to the chromosphere, or variation of cross-sectional area of the loop. Therefore, the initial cooling of the 10^7 K plasma, and its effect on the formation of condensations cannot be investigated and the dynamics of the cool, 10^4 K, plasma cannot be calculated. Hence, this model cannot be directly compared with the observations of loop prominences.

We believe that the general features of the evaporation model proposed by these authors are correct. In this model loop prominences

are a natural part of the cooling process and are not due to some unobserved phenomena. Therefore, in order to critically test the model, we calculate the evolution of a post-flare loop including all the effects described above; and compare our results with observations. The model of a loop prominence that we use for our calculation is described in detail in the following chapter.

3. MODEL OF A LOOP PROMINENCE

3.1 Introduction

In this chapter we describe a one-dimensional (only variations parallel to $\vec{B}$ are considered), single-fluid model of a loop prominence which we have analyzed numerically. The physical assumptions that have been made and their justification are discussed below.

3.2 Single-Fluid Assumption

The temperatures and densities used in the model are those observed for loop systems,

$$3 \times 10^4 \text{ K} \leq T \leq 10^7 \text{ K} \quad , \tag{3.1}$$

and $n \sim 10^{11}$ cm^{-3}. We assume that the plasma can be described by single-fluid equations. This approximation is valid only if the characteristic size scales and time scales of the fluid are larger than the mean free path and the relaxation time respectively. Spitzer (1962) has calculated the mean free path of electrons and protons in a fully ionized hydrogen plasma and the electron-proton relaxation time,

$$\lambda_f \approx 10^4 \, T^2 \, n^{-1} \text{ cm.} \quad , \tag{3.2}$$

and

$$\tau_{ep} \approx 20 \, T^{3/2} \, n^{-1} \text{ sec.} \tag{3.3}$$

The length and time scales over which significant changes can occur in a loop are the thermal instability size scale, λ_c, equation (1.19) and the cooling time τ_c, equation (1.22). For the values of T in (3.1), we find that λ_f/λ_c and $\tau_{ep}/\tau_c << 1$.

3.3 Radiative Losses

Since hydrogen comprises $\sim 90\%$ of the ions in the coronal plasma, the effects of the heavier trace elements are negligible except for their contribution to the radiation loss rate at temperatures above $\sim 3 \times 10^4$ K. At high temperatures, ($\geq 10^5$ K), the radiation cooling is due almost entirely to lines in heavy ions such as O^{5+}. These losses can be represented as a heat sink term in the energy equation, thus, we approximate the loop material by the fluid equations for a pure hydrogen plasma but with a cooling function, $\mathcal{L}$, which includes the radiative losses of the heavy elements.

The form of $\mathcal{L}$ used is that derived by Cox and Tucker (1969). In their calculations they assumed that the plasma is of cosmic abundances, is optically thin to all radiation, and is in statistical equilibrium with the states of ionization determined by a balance of radiative and dielectric recombination with collisional ionization. All the radiative and ionization processes considered vary as the electron density and ion density, hence the cooling function can be written as:

$$\mathcal{L}(n,T) = n_e \, n\Lambda(T) \text{ erg cm}^{-3} \text{ s}^{-1} \quad , \tag{3.4}$$

where $\Lambda(T)$ has been tabulated by Cox and Tucker, Figure 1.1.

The assumptions above are valid for loop plasma above $\sim 3 \times 10^4$ K where hydrogen is almost fully ionized, but they break down at temperatures below this. Once a significant amount of neutral hydrogen forms, the plasma will not be optically thin to hydrogen lines. The mean free path of a line photon is given by,

$$\lambda = 1/n_H \, \sigma \quad , \tag{3.5}$$

where σ is the cross-section for absorption. For Ly α, $\sigma \sim 10^{-14}$ cm^2, hence the mean free path is $\sim 10^3$ cm at densities of 10^{11} cm^{-3}. This means that if a slab of loop plasma only 1 km. thick were to cool to temperatures $\sim 10^4$ K, the optical depth of the slab would be $\geq 10^2$. Clearly, condensation in loops cannot be optically thin in at least Ly α, hence, in order to follow the cooling at low temperatures in detail one must include radiation transfer effects.

Another assumption that breaks down at low temperatures is that the state of ionization is in equilibrium. Consider a plasma that is cooling from a very high temperature, $> 10^6$ K, so that initially all the hydrogen is ionized. Assuming that the Cox and Tucker conditions are applicable, it will eventually cool to 1.6×10^4 K with percentage of ionization, $n_e/n \approx 50\%$. Now in order to justify using equilibrium equations to determine the ionization state, we must have the cooling time much greater than the recombination time, otherwise the temperature will change before equilibrium can be established. However, with the cooling rate and the recombination coefficient given by Cox and Tucker, we find that at $T \simeq 1.6 \times 10^4$ K,

$$\frac{\tau_c}{\tau_{rec}} = \left(\frac{3/2\ p}{\mathcal{L}}\right) \times nR_H = .06 \quad , \tag{3.6}$$

hence the assumption of statistical equilibrium is invalid at these temperatures.

The arguments above imply that in order to calculate the behavior of the plasma below the 3×10^4 K level, we would need to follow it on very small size and time scales and include radiation transfer. Therefore, mainly for ease of calculation, we assume in our model that the

temperature does not fall below 3×10^4 K. This assumption is not unjustified since we expect that for the physical conditions present in loops, the important heat loss mechanisms, conduction and radiation, essentially vanish by $\sim 10^4$ K. Radiation losses become small since the temperature is $\leq 1/10$ the threshold energy required to excite hydrogen from its ground state, and the number of free electrons is reduced due to recombinations. Also, optical depth effects result in a decrease of emission. Conduction becomes negligible at low temperatures because the coefficient of conduction for a fully ionized plasma varies as a high power of T (Spitzer, 1962):

$$\kappa = 10^{-6} T^{5/2} \text{ ergs cm}^{-1} \text{ K}^{-1} \text{ sec}^{-1} \quad . \tag{3.7}$$

By fixing a minimum temperature we do ignore the profile of the plasma between 10^4 - 3×10^4 K. However, we are primarily interested in determining whether the thermal instability mechanism can produce condensations in loops. As far as the hot loop plasma, $> 10^6$ K, is concerned, the difference between 10^4 and 3×10^4 K is negligible. The main error is that we effectively overestimate the pressure of a condensation, hence we can say that if condensations do form under our assumptions, they will certainly form in a more exact calculation and will be cooler and smaller.

3.4 MHD Equations

Since we restrict the loop temperature to $T \geq 3 \times 10^4$ K, the state of ionization $n_e/n > 99\%$, and we can take the plasma to be fully ionized. The single-fluid equations for a fully ionized hydrogen plasma in the presence of a gravitational field and a magnetic field are well known,

cf. Braginskii (1965). They are listed below:

the equation of continuity,

$$\frac{\partial}{\partial t}\rho + \nabla \cdot (\rho\vec{v}) = 0 \quad ; \tag{3.8}$$

the equations of motion,

$$\rho\left(\frac{\partial}{\partial t} + \vec{v}\cdot\nabla\right)\vec{v} + \nabla p + \nabla\cdot\ddot{\Pi} = \rho\vec{g} + \frac{1}{c}\vec{J}\times\vec{B} \quad ; \tag{3.9}$$

the heat equation,

$$\rho\left(\frac{\partial}{\partial t} + \vec{v}\cdot\nabla\right)\epsilon + p\nabla\cdot\vec{v} + \nabla\cdot\vec{q} + (\ddot{\Pi}\cdot\nabla)\cdot\vec{v} = -\mathcal{L} + \vec{J}\cdot\left[\vec{E} + \frac{\vec{v}}{c}\times\vec{B}\right] \; ; \tag{3.10}$$

and the equation of state,

$$p = \frac{2\rho}{m_H}kT \quad . \tag{3.11}$$

The quantity ϵ in (3.10) is the internal energy per gram of the plasma, and in our case,

$$\epsilon = \frac{3kT}{m_H} \quad . \tag{3.12}$$

The stress tensor $\ddot{\Pi}$ and the heat flux vector $\vec{q}$ can be broken up into two parts, one parallel and one perpendicular to the magnetic field,

$$\vec{q} = K_{\parallel}\nabla_{\parallel}T + K_{\perp}\nabla_{\perp}T \quad , \tag{3.13a}$$

and

$$\ddot{\Pi} = \eta_{\parallel}\ddot{W}_{\parallel} + \eta_{\perp}\ddot{W}_{\perp} \quad , \tag{3.13b}$$

where the elements of $\ddot{W}$ are terms like $\frac{\partial v_\alpha}{\partial x_\beta}$. For our model the

components of $\vec{q}$ and $\vec{\vec{\Pi}}$ perpendicular to $\vec{B}$ are negligible compared to those parallel. This is because the diffusion coefficients for a particular direction, $K_{\parallel,\perp}$ and $\eta_{\parallel,\perp}$ depend on the mean free path in that direction. Parallel to the field the relevant quantity is the collision mean free path, and perpendicular to the field the gyroradius is important. Braginskii (1965) obtains,

$$\frac{K_{\parallel}}{K_{\perp}} \sim (\omega_g \tau_{col})^2 \sim \frac{\eta_{\parallel}}{\eta_{\perp}} \quad , \tag{3.14}$$

where τ_{col} is the collision time and ω_g is the gyrofrequency. Taking $B \sim 10^2$ G, and $n \sim 10^{11}$ cm^{-3}, yields,

$$(\omega_g \tau_{col})^2 = 10^6 B^2 T^3 n^{-2} = 10^{-14} T^3 \quad . \tag{3.15}$$

For temperatures $T \geq 10^5$ K, the ratio of parallel to perpendicular diffusion is $\geq 10^4$, hence we can ignore perpendicular diffusion. For low temperatures, $\leq 10^5$ K, the mean free path is so short that both parallel and perpendicular diffusion are negligible.

The coefficient of viscosity, $\eta_{\parallel}$, is given by Spitzer (1962)

$$\eta_{\parallel} = 10^{-16} T^{5/2} \text{ gm cm}^{-1} \text{ sec}^{-1} \quad . \tag{3.16}$$

For our values of density, temperature, and size scale, the Reynolds number for the plasma is,

$$R_u = \frac{\rho v L}{\eta_{\parallel}} \geq 10^3 \quad . \tag{3.17}$$

This large value for R_u means that the viscosity results in a negligible dissipation of momentum and energy, i.e. the plasma is approximately inviscid. In the numerical calculations we introduce an artificial

viscosity in order to take care of the possible formation of shocks, however we ignore the ordinary plasma viscosity.

3.5 Magnetic Field Structure

In our model it is assumed that all quantities vary along $\vec{B}$ only; hence, one-dimensional equations can be used. Justification for this assumption is provided by the following arguments.

The magnetic field in a post-flare region is observed to have sufficient strength to dominate the plasma. This may not be true immediately after a flare; since, if the plasma thermal energy is derived from magnetic energy, then probably they are initially of comparable magnitude. However, as the plasma cools from initial temperatures of $\sim 3 \times 10^7$ K to $< 10^7$ K the magnetic field begins to dominate. For our temperatures and densities the field strengths reguired are, $B \geq 10$ G, a value well within the magnitudes observed (Section 2.2.1).

Since the plasma is fully ionized, the conductivity is high enough to insure that the "frozen in" condition is valid, i.e. the magnetic flux through any area moving with the plasma remains constant. In our case the plasma pressure is not sufficient to transport the field; hence, the plasma is constrained to move only along field lines like beads on a rigid wire. It was shown in the previous section that the only significant components of the stress tensor $\vec{\vec{\Pi}}$ and the heat flux $\vec{q}$ are also parallel to $\vec{B}$. Therefore, the equations of motion (3.9) reduce to a single equation for mass flux along $\vec{B}$, and the heat equation (3.10) involves heat flux only along $\vec{B}$ as well.

In order to obtain a one-dimensional model we must assume that the relevant variables T, v and n do not vary over some area, A, perpendicular to $\vec{B}$. The observed morphology of loop prominences (Bruzek, 1964a) suggests that they form along field lines, the loop consisting of a flux tube with cross-sectional radius r_0 small compared to the loop length. For r_0 sufficiently large then the arguments above imply that the tube is effectively insulated from the rest of the corona, since during the lifetime of a loop very little heat or mass is exchanged between the loop and its surroundings. This will be true when the cooling time τ of a loop is much less than the time scale for significant transverse conduction, $\tau_\perp$. The determining factor is $\tau/\tau_\perp$, where

$$\tau_\perp = \frac{p r_0^2}{K_\perp T} = 10^{-4}\ B^2\ T^{1/2}\ n^{-1}\ r_0^2 \quad , \tag{3.18}$$

and $\tau \approx 10^3$ sec. from observations. Hence for $B \approx 30$ G, $T \approx 10^7$ K, and $n \approx 10^{11}$ cm^{-3}, $\frac{\tau}{\tau_\perp} = 1$ for $r_0 = 10^6$ cm. If the tube radius is less than 10^6 cm. then conduction across the tube is dominant; and, the temperature will be approximately constant over the cross-sectional area of the tube. However, this means that a significant amount of heat may be exchanged between the tube and the surrounding corona. Conversely, if the radius r_0 is greater than 10^6 cm., then the tube is effectively insulated from the outside but significant temperature variations can occur across the tube.

Loop prominences have radii, $r_0 \sim 10^8$ cm., and so we expect the latter case to hold. Hence, there could be small scale irregularities across loops, but structures of this size scale, $\leq 10^6$ cm., would be

very difficult to observe. In our model we assume that there are no small scale irregularities; therefore, the loop is both insulated and constant on a cross-sectional area. This assumption allows us to use one-dimensional equations. Of course, there is a boundary between the loop and the surroundings over which large temperature differences occur; however, the discussion above indicates that the width of this boundary is small compared to the width of loop prominences. Since we do not specify the magnitude of the area of the tube in our equations, the calculations also apply to the case where the tube area is small enough to insure that no small scale irregularities are present, but the tube is also insulated from the surrounding plasma. This situation might be possible if the field is non-potential.

Figure 3.1 illustrates the geometry of our model loop. We assume a dipole source imbedded a distance D below the top of the chromosphere, and consider a flux tube of height above the source R that lies in a plane perpendicular to the solar surface. We could easily consider the tube to be inclined at some angle from the vertical. This would only reduce the effective gravitational acceleration $\vec{g}$ by some constant factor, cos φ, and would not appreciably affect our results. In general, loop prominences are not observed to occur at large angles from the vertical.

Letting s be distance along the loop measured from the top, we have that all variables, including the cross-sectional area A, are functions of s only. The effect of the magnetic field on the plasma is accounted for by including A and by permitting only heat and mass transfer along s. Each flux tube is uniquely characterized by two parameters: the

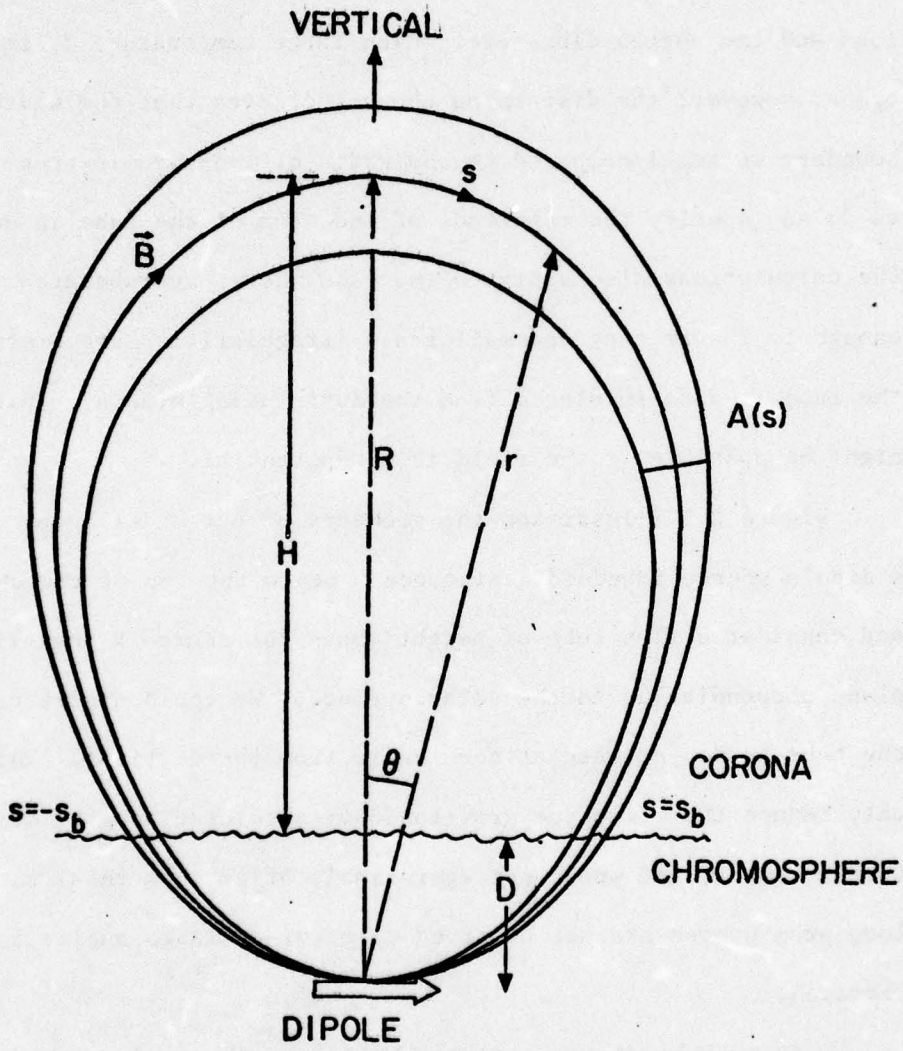

Figure 3.1 GEOMETRY OF OUR MODEL LOOP

size R and the compression factor Γ which is defined as the ratio of field strength at the chromosphere ($s = \pm s_b$) to that at the top ($s = 0$).

$$\Gamma = B(s_b)/B(s = 0) = A(s = 0)/A(s = s_b) \tag{3.19}$$

3.6 One-Dimensional Equations

Modifying the MHD equations (3.8) - (3.10) to fit our one-dimensional model and neglecting viscosity, we obtain the following set of equations:

$$\frac{\partial n}{\partial t} + \frac{1}{A(s)} \frac{\partial}{\partial s} (Anv) = 0 \quad , \tag{3.20}$$

$$n\left(\frac{\partial}{\partial t} + v \frac{\partial}{\partial s}\right) v + \frac{1}{m_H} \frac{\partial}{\partial s} p - n g_{\parallel}(s) = 0 \quad , \tag{3.21}$$

and

$$n\left(\frac{\partial}{\partial t} + v \frac{\partial}{\partial s}\right) \epsilon + \frac{p}{A} \frac{\partial}{\partial s}(Av) - \frac{1}{A} \frac{\partial}{\partial s}\left(AK \frac{\partial T}{\partial s}\right) + n^2 \Lambda(T) = 0 \quad . \tag{3.22}$$

The derivation of equations (3.20) - (3.23), including the viscosity term is given in Appendix A. In these equations v is the velocity along the field, and $g_{\parallel}$ is the component of the gravitational field along $\vec{B}$. The variable n is the number density of ions (mostly protons in our case); hence the mass density,

$$\rho = (m_e + m_p)\, n = m_H n \quad , \tag{3.23}$$

the pressure,

$$p = (n_e + n_p)\, kT = 2nkT \quad , \tag{3.24}$$

and the internal energy per ion,

$$\epsilon = \frac{3}{2}\frac{p}{n} = 3kT \quad . \tag{3.25}$$

The area of the tube is given by A(s); however, from the equations above we note that the magnitude of A is unimportant, only relative values enter. Therefore, without loss of generality we set the area at the top to unity,

$$A(s = 0) = 1 \quad . \tag{3.26}$$

Equations (3.20) - (3.25) are sufficient to determine our four variables v, t, n and p as functions of t and s. A and $g_{\parallel}$ are known functions of s; they are completely determined by our choice of magnetic field. In Appendix A the dependence of A and $g_{\parallel}$ on s is derived. Defining,

$$v = \sin\theta \quad , \tag{3.27}$$

where θ is the angle from the vertical (Figure 3.1). We obtain

$$s = \frac{R}{2}\left\{v\sqrt{3v^2 + 1} + \frac{1}{\sqrt{3}}\ln\left(\sqrt{3}\,v + \sqrt{3v^2 + 1}\right)\right\} \quad , \tag{3.28}$$

$$A(v) = (1 - v^2)^3\sqrt{3v^2 + 1} \quad , \tag{3.29}$$

and

$$g_{\parallel}(v) = g_{\odot}\,3v\sqrt{\frac{1 - v^2}{3v^2 + 1}} \quad . \tag{3.30}$$

Although $g_{\parallel}$ and A are not expressed explicitly in terms of s, their numerical value for a particular s can easily be obtained using equations (3.28) - (3.30). Since the heights of the loops we consider are small compared to a solar radius, equation (3.30) does not include

the effect of a changing gravitational potential with height.

The only other variables in our equations, the conductivity K and the radiative loss rate Λ, are functions of T only. K is given by equation (3.7) and Λ has been tabulated by Cox and Tucker (1969), Figure 1.1.

4. NUMERICAL METHODS

4.1 Introduction

We wish to solve equations (3.20) - (3.22) along with suitable initial and boundary conditions. In order to facilitate the computation, we first convert to Lagrangean coordinates. There are two reasons for doing this: first, we eliminate all "convective" terms (of the form $v \frac{\partial f}{\partial s}$); second, we are able to treat parts of the plasma of varying density with the same accuracy. If thermal instability occurs, then we expect to obtain variations in density of several orders of magnitude over the length of a loop. This variation is impossible to follow with a grid of fixed intervals in s unless the grid is very fine. With a reasonable grid (~ 64 points over the length of the loop), a condensation may occupy less than one grid interval. One way to circumvent this difficulty is to choose a grid so that equal intervals contain equal amounts of plasma; the spatial positions of these grid points are no longer fixed and will have to be calculated along with the other variables.

Hence, we change independent variables from s, the distance along the loop measured from the top to x(s), the amount of plasma in the loop from the top to position s at t = 0, i.e.

$$x \equiv \int_0^s n(s,0)\, A(s)\, ds \quad . \tag{4.1}$$

Therefore,

$$x_m = \int_0^{s_b} n(s,0)\, A(s)\, ds \tag{4.2}$$

is the total number of ions in one half of the loop. We note that if the density is initially uniform then x(s) is proportional to the

volume of the loop between the top and the point s.

A new variable, S(x,t), must now be introduced. It denotes the Eulerian position of that slab of plasma labeled "x". Converting equations (3.20) - (3.22) to Lagrangean formulation and rearranging, we obtain:

$$\frac{\partial}{\partial t} v(x,t) = - \frac{1}{m_H A(S)} \frac{\partial}{\partial x} p(x,t) + g_{\parallel}\Big(S(x,t)\Big) \quad , \tag{4.3}$$

$$\frac{\partial}{\partial t} S(x,t) = v(x,t) \quad , \tag{4.4}$$

$$\frac{\partial}{\partial t} T(x,t) = - \frac{p(x,t)}{3k} \frac{\partial}{\partial x} \Big(A(S)\, v(x,t)\Big) - \frac{n(x,t)\, \Lambda(T)}{3k}$$

$$+ \frac{2 \cdot 10^{-6}}{21 \cdot k} \frac{\partial}{\partial x} \left(A^2\, n \frac{\partial}{\partial x} T^{7/2}\right) \quad , \tag{4.5}$$

with

$$p = 2knT \quad , \tag{4.6}$$

and

$$n(x,t) = \left[A(S) \frac{\partial S}{\partial x}\right]^{-1} \quad . \tag{4.7}$$

Equations (4.3) - (4.7) are in the form that we use for numerical calculations. We assume a grid of equal intervals in x, which is equivalent to dividing up the loop into slabs of equal mass. The behavior of the loop plasma is then simulated by following the evolution of these slabs as determined by equations (4.3) - (4.5).

4.2 Boundary and Initial Conditions

In order to determine the correct boundary conditions for the system (4.3) - (4.7), we first note that there are actually only two distinct dependent variables: the position of the plasma S and the temperature or internal energy T. Equations (4.3), (4.6) and (4.7) can be used to eliminate v, p and n, resulting in one partial differential equation of second order in time for S and one of first order in time for T. The spatial terms, however, are highly nonlinear. The highest x derivative for both S and T are of second order. We essentially have a hyperbolic equation for S and a parabolic equation for T in the two independent variables x and t. Suitable boundary conditions for such a system are Cauchy conditions for S and Dirichlet for T on an open region in the x,t plane. In particular, as initial conditions we specify T, S and $\frac{\partial S}{\partial t}$ on $t = 0$, and as spatial boundary conditions we specify T and S at both ends of the loop for all t.

From the geometry of the loop, Figure 3.1 and from observations, it appears reasonable to assume that the loop is symmetric about the vertical axis. This implies that T must be a symmetric function of x and S antisymmetric; hence we need solve the equations only for $x_m \geq x \geq 0$. At $x = 0$, i.e. the top of the loop, the boundary conditions must be $\frac{\partial}{\partial x} T(0,t) = 0$ and $S(0,t) = 0$.

The conditions at the base of the loop are determined from physical consideration. We are interested in the cooling phase of flares, specifically when radiative losses dominate the cooling. During this phase we do not expect to have significant heating or evaporation of chromospheric material; therefore, we take the temperature at the base

of our model to be that in the upper chromosphere, $T(S_b) \approx 3 \times 10^4$ K, and to remain constant during our calculation. We do include the conduction of heat from the loop to the base; however, we assume that this energy can be radiated away by the base without appreciably affecting its temperature.

This situation may appear inconsistent since on the one hand, we have that the cooling rate of the base is high enough to radiate all of the energy conducted down from the loop yet, on the other hand, the rate is so slow that the base temperature does not change during the cooling time of the loop. The resolution to this inconsistency is in the behavior of the radiative losses at low temperatures. As discussed in Section 3.3, the loss rate decreases very rapidly for low temperatures. Assuming the Cox and Tucker loss rate, we obtain for $n \sim 10^{13}$ cm^{-3} and $T \sim 3 \times 10^4$ K

$$n_e n\Lambda(T) \sim 10^4 \text{ ergs cm}^{-3} \text{ s}^{-1} \quad .$$

This radiative rate is high enough to dissipate an incoming energy flux of 10^9 ergs cm^{-2} s^{-1} in a thickness of only 1 km. But at $T \sim 10^4$ K, $n_e n\Lambda(T) \leq 10^{-2}$ ergs cm^{-3} s^{-1}, which implies a cooling time, $\tau_c \sim \frac{3nkT}{n_e n\Lambda} \geq 10^5$ s. Therefore, the base plasma is "trapped" between 10^4 - 3×10^4 K; the cooling rate at the lower temperature is too low to allow a significant decrease, while the losses at the upper value are too high to permit an increase in temperature. The exact profile of the base temperature is unimportant to our model; hence, for convenience we take it to be constant at 3×10^4 K.

As a boundary condition on S, the position of the base is assumed to be fixed during the cooling process. This is a good approximation since the gravitational scale height of the chromosphere is very small compared to the size of typical loops. At $T \sim 10^4$ K, $H_g = \frac{kT}{m_H g} \sim 400$ km; therefore, the chromospheric material will move very little in response to pressure changes in the loop plasma.

The initial conditions for our model loop are somewhat arbitrary. Order of magnitude values of the temperature and density are set by observations, $T \sim 10^7$ K and $n \sim 10^{11}$ cm^{-3}; however, the detailed profiles are not known. As conditions on the velocity and pressure, we assume that the plasma is initially at rest,

$$v(s, 0) = 0 \quad , \tag{4.8}$$

and in hydrostatic equilibrium,

$$\left.\frac{\partial p}{\partial s}\right|_{t = 0} = m_H \, n \, g_{\parallel} \quad . \tag{4.9}$$

Neither of these assumptions is probably valid immediately after the loop fills with evaporated chromospheric material; however, we expect these conditions to be achieved in a time short compared to the cooling time, $\geq 10^3$ secs. For loop heights of $\sim 3 \times 10^9$ cm. the travel time across the loop at the sound speed is only $\sim 10^2$ s; hence, plasma motion will cancel unbalanced pressure gradients before appreciable cooling can take place. This motion will in turn be damped by thermal conduction; the dissipation time for wavelengths $\leq 3 \times 10^8$ cm. is ≤ 30 seconds. Oscillations of long wavelengths, $\geq 10^9$ cm., corresponding to a fundamental mode of the tube could persist; however, our calculations

(Section 5.4.3) indicate that they do not significantly affect the formation of condensations.

The important parameters of the initial temperature profile are the average temperature, which is determined from soft x-ray observations, and the heat flux to the chromosphere. Only an upper bound can be placed on the latter; the downward heat flux should not be more than the total radiative rate during maximum flare brightness. (This argument, of course, assumes that a significant portion of the flux is not dissipated by evaporation.) Since flares are not usually seen in white light, we can place an upper bound of $\sim 10^{10}$ ergs cm^{-2} s^{-1} on the heat flux into the chromosphere; however, our calculations (Section 5.2), indicate that the flux is usually much less than this value.

Assuming that the heat flux is of the same order as the chromospheric Hα flux, $F \sim 10^{7}$ ergs cm^{-2} s^{-1}, we obtain for the temperature scale height;

$$H_T = \left(\frac{1}{T}\frac{dT}{ds}\right)^{-1} = 10^{-6}\,\frac{T^{7/2}}{F} \quad , \tag{4.10}$$

hence $H_T = 3 \times 10^{11}$ cm. at $T = 10^{7}$ K. Since this scale height is much larger than the size of a loop, only a very slight temperature difference over the loop length is needed to carry the flux. Also, the scale height has a strong dependence on T. For low temperatures, $T \leq 10^{6}$ K, equation (4.10) yields $H_T \leq 10^{8}$ cm., which is much less than typical loop lengths. From the arguments above, we expect that most of the loop volume will be at $\sim 10^{7}$ K, with only a small fraction of the plasma at lower temperature. Therefore, we approximate the profile by assuming that initially the temperature is uniform at $\sim 10^{7}$ K, i.e.

$$T\,(s, 0) = \text{const.} \tag{4.11}$$

Equation (4.9) can now be used to determine the pressure profile,

$$p(s, 0) = p_0 \exp\left[-\frac{m_H}{2kT}\int_0^s g_{\parallel}(s)\, ds\right] . \qquad (4.12)$$

However, for $T \sim 10^7$ K, the gravitational scale height

$$H_g = \frac{2kT}{m_H g_{\parallel}} \gtrsim 10^{11} \text{ cm.} \quad , \qquad (4.13)$$

which is much larger than the loop length. Hence, equation (4.12) can be well approximated by

$$p(s, 0) = p_0 = \text{const.} \qquad (4.14)$$

Equation (4.11) and (4.14) imply that

$$n(s, 0) = \text{const.} \qquad (4.15)$$

Using the initial density profile (4.15) and equation (4.1), we can express the initial conditions (4.8), (4.11) and (4.15) in terms of x. In this case, the procedure is trivial; all three initial profiles are uniform in x. They have the obvious advantage of being very simple. Perturbation can easily be introduced into these profiles. There is the difficulty, however, of matching them with the boundary conditions at the base. Since the base is at 3×10^4 K while the loop is at 10^7, we, essentially, have replaced the steep gradient in T by a discontinuity. Therefore, we must modify the boundary conditions at the base.

The important quantity is the heat flux out the loop. We use the following method to determine it. Assume that the loop has been divided into a number of equal mass intervals. The position S_b and the temperature T_b of the base are known and assumed to be constant in time; also, the

mean position and temperature of the plasma in the lowest slab, S_f and T_f, are known at some time t. The outward heat flux is then calculated by assuming that the flux between S_b and S_f is independent of x, i.e. we assume that for fixed t the heat flux across the final slab is a constant heat flux determined by its temperature and width. Thus,

$$F_b = \frac{2 \cdot 10^{-6}}{7} \left(T_f^{7/2} - T_b^{7/2} \right) \left(\int_{S_f}^{S_b} \frac{dS}{A(S)} \right)^{-1} , \qquad (4.16)$$

where we have used the Spitzer conductivity. If the radiative losses of the plasma between S_f and S_b are small, then the expression (4.16) is valid. If the losses are large, then we are overestimating the outward heat flux since a significant portion of it will be radiated away before reaching the base. In our calculations, $S_f - S_b$, is usually small enough so that the first situation is realized. In any case, the maximum error is only of the order of a factor of 2 in the total energy losses of the last slab. Also, our loss rate function $\Lambda(T)$ is probably only of that order of accuracy. Since we are primarily interested in the behavior of the plasma at the top of a loop, where condensations form, we do not expect that the use of equation (4.16) introduces a significant error.

In summary, we have that equations (4.3) - (4.7) are to be solved on the open region,

$$0 \leq x \leq x_m \text{ , and } t \geq 0 \text{ ,}$$

with given initial conditions

$$T(x, 0) \text{ , } S(x, 0) \text{ and } \frac{\partial}{\partial t} S(x, 0) \left(= v(x, 0) \right) \text{ ,} \qquad (4.18)$$

and spatial boundary conditions

$$\frac{\partial}{\partial x} T(0, t) = 0 \ , \ T(x_m, t) = 3 \times 10^4 \ K \ ,$$
$$S(0, t) = 0 \text{ and } S(x_m, t) = S_b = \text{const.} \tag{4.19}$$

Note that equation (4.4) and the conditions above imply that

$$v(0, t) = v(x_m, t) = 0 \ . \tag{4.20}$$

4.3 Shocks

A sticky problem in the numerical solution of hydrodynamic equations such as (4.3) - (4.5) is the handling of shocks; no fast method for treating them exactly exists. We use the standard procedure (e. g. Goldsmith, 1970) of introducing the van Neumann-Richtmeyer artificial viscosity term in the equations. This term is a pseudo-viscous pressure. In equations (4.3) and (4.5) the pressure p is replaced by (p + q) where q is defined as

$$q = \begin{cases} (a \, \Delta x)^2 \, n m_H \left(\frac{\partial v}{\partial x}\right)^2 & \text{if } \frac{\partial v}{\partial x} < 0 \\ 0 & \text{if } \frac{\partial v}{\partial x} \geq 0 \end{cases} \tag{4.21}$$

where Δx is the grid spacing and a is a dimensionless constant, $a \sim 1.5$ - 2, which determines the thickness of the shock.

The effect of introducing this term in the fluid equations has been investigated in detail (Richtmeyer and Morton, 1967). A true shock shows up as a jump in the values of n, T and v with a width of $\sim a^2$ intervals and with approximately correct values for the size of the jump and the speed of the shock through the fluid. Because $\left(\frac{\partial v}{\partial x}\right)^2$ is

small outside of the shock, q does not affect the behavior of the plasma away from the shock. In addition, since q is defined to vanish for positive velocity gradients, it has no effect on free expansion. Tests on the artificial viscosity by various authors (Richtmeyer and Morton, 1967) indicate that, in general, it seems a fairly accurate (and fast) way of accounting for shocks.

There are two places in our model where we expect that shocks might form, and hence, q becomes important. One is at the boundary of a condensation where large pressure gradients form. The size scale h of a knot is determined by a balance between radiative cooling and conductive heating,

$$h \approx \frac{10^{-3}\ T^{7/4}}{n\sqrt{\Lambda(T)}} \quad . \tag{4.22}$$

The time scale for growth of a knot is the cooling time,

$$\tau = \frac{3kT}{n\Lambda} \quad . \tag{4.23}$$

In order to maintain pressure equilibrium, plasma must move fast enough to keep up with pressure changes,

$$v \approx h/\tau_c \approx 4 \times 10^{12} \sqrt{\Lambda}\ T^{3/4} \quad . \tag{4.24}$$

As long as these velocities are damped quickly (i.e. in a time short compared to the cooling time) then they remain subsonic.

$$M = \frac{v}{c} = 4 \times 10^{8} \sqrt{\Lambda}\ T^{1/4} \quad , \tag{4.25}$$

and $M < 1$ for $3 \times 10^4 \leq T \leq 5 \times 10^6$ K. However, since conduction is the only

dissipative process present, then these velocities will not be damped because whenever condensations occur, the radiative cooling time must be short compared to the conductive cooling time. Hence, velocities generated while the plasma is hot will persist and result in shocks. At $T \sim 10^6$ K, equation (4.24) gives $v = 30$ km s^{-1}, which is supersonic at $T = 3 \times 10^4$ K. In Section 5.4.2, we examine a simple analytic model for the growth of condensations and find that shocks may indeed form at the boundary between the cold and hot regions. Our numerical calculations also support this result.

Shocks also form when cool, freely-falling material impacts onto the chromosphere. Downward velocities on the order of $\sim 10^7$ cm s^{-1} are observed; these are well above the sound speed at chromospheric temperatures. In our model, the artificial viscosity q dissipates the streaming energy of the falling material. The usual dissipation mechanisms, conduction and viscosity vary as high powers of T and are negligible at low temperatures. However, the velocities of the cool plasma are obviously damped by some means since this plasma is not observed to bounce back into the corona after impacting the chromosphere. We believe that the most likely source of this dissipation is shocks.

4.4 Computer Code

In order to obtain numerical solutions for the system (4.3) - (4.7), including the artificial viscosity, we use a two-step, second order difference scheme similar to the ones described by Richtmeyer and Morton, 1967. We have three partial differential equations to solve for the variables v, S and T. They can be written as:

$$\frac{\partial}{\partial t} V = F\left(V, \frac{\partial V}{\partial x}, \frac{\partial^2 V}{\partial x^2}\right) , \tag{4.26}$$

where V is a three component vector (v, s, T) and F is a nonlinear function of V and its spatial derivatives. The pressure and number density are given as explicit functions of V by equations (4.6) and (4.7); hence, they can be obtained directly. Assuming that $V(x, t)$ is known, $V(x, t + \Delta t)$ can be obtained by a Taylor series expansion,

$$V|_{t + \Delta t} = V|_t + \Delta t\left(F|_t + \frac{\Delta t}{2} \frac{\partial F}{\partial t}|_t\right) + O(\Delta t^3) \quad . \tag{4.27}$$

But,

$$F|_{t + \frac{\Delta t}{2}} = F|_t + \frac{\Delta t}{2} \frac{\partial F}{\partial t}|_t + O(\Delta t^2) \quad , \tag{4.28}$$

hence

$$V|_{t + \Delta t} = V|_t + \Delta t\, F|_{t + \frac{\Delta t}{2}} + O(\Delta t^3) \quad . \tag{4.29}$$

From equation (4.28) we note that $F|_{t + \frac{\Delta t}{2}}$ is needed only to first order accuracy in Δt; therefore we first generate provisional values of $\tilde{V}|_{t + \frac{\Delta t}{2}}$ defined by:

$$\tilde{V}|_{t + \frac{\Delta t}{2}} \equiv V|_t + \frac{\Delta t}{2} F|_t = V|_{t + \frac{\Delta t}{2}} + O(\Delta t^2) \quad , \tag{4.30}$$

and define

$$\tilde{F}|_{t + \frac{\Delta t}{2}} \equiv F\left(\tilde{V}|_{t + \frac{\Delta t}{2}}\right) = F\left(V|_{t + \frac{\Delta t}{2}}\right) + O(\Delta t^2) \quad . \tag{4.31}$$

Since F is a smooth, well-behaved function of V, we can expand the right-hand side of equation (4.31) to obtain

$$\tilde{F}\Big|_{t + \frac{\Delta t}{2}} = F\Big|_{t + \frac{\Delta t}{2}} + O(\Delta t^2) \quad . \tag{4.32}$$

The scheme consists of first generating $\tilde{V}\Big|_{t + \frac{\Delta t}{2}}$ from (4.30) and then calculating $\tilde{F}\Big|_{t + \frac{\Delta t}{2}}$; then $V\Big|_{t + \Delta t}$ is obtained from

$$V\Big|_{t + \Delta t} = V\Big|_{t} + \Delta t \, \tilde{F}\Big|_{t + \frac{\Delta t}{2}} + O(\Delta t^3) \quad . \tag{4.33}$$

Equation (4.33) follows immediately from equations (4.29) and (4.32).

The boundary conditions $S(x, 0)$, $v(x, 0)$ and $T(x, 0)$ are used to initiate the calculation and the spatial boundary conditions are used to compute the velocities and heat flux at the ends of the space grid. To facilitate the computation, we rewrite equation (4.7) as

$$n(x, t) = \left[\frac{\partial}{\partial x} AI(s)\right]^{-1} \quad , \tag{4.34}$$

where

$$AI(s) = \int_0^s A(s) \, ds \quad . \tag{4.35}$$

Three known functions of S, $g_{\|}(S)$, $A(S)$ and $AI(S)$, appear in the equations and two of T, $\Lambda(T)$ and $T^{1/2}$. Rather than evaluate these five functions directly (this requires too much computer time), we first tabulate them for ~ 800 semi-logarithmically spaced values of S and T, and use linear interpolation to estimate their value for a particular S or T. The estimated values are accurate to better than 1%.

The fineness of the x grid, Δx, and the time increments Δt are determined by the requirements that they be smaller than length scales

and time scales of interest and that the difference scheme remain stable. The equations that we wish to solve are highly nonlinear. Unfortunately, very little is known about the stability or convergence of finite difference schemes for such systems. The only accurate method known to determine stability is, of course, trial and error. However, we calculate stability criteria for several linear approximations to our system and hope that these restrictions are sufficient to assure convergence.

If we neglect the heat loss terms, the area factor and gravity, our equations reduce to those of a perfect fluid. Our scheme then becomes equivalent to the Lax-Wendroff scheme (Richtmeyer and Morton, 1967), which has as its stability criterion

$$\Delta t_1 < \min_j \frac{\Delta S_j}{(|v|_j + C_j)} \quad , \tag{4.36}$$

where ΔS_j is the Eulerian width of the grid spacing Δx at the jth grid point, and C_j is the speed of sound at this point. The index j runs over all the intervals in the x grid. If we approximate the heat equation (4.5) by a simple diffusion equation

$$\frac{\partial T}{\partial t} = \kappa \frac{\partial^2 T}{\partial s^2} \quad , \tag{4.37}$$

then the stability criterion is

$$\Delta t_2 < \min_j \frac{(\Delta s)_j^2}{\kappa_j} \quad . \tag{4.38}$$

Since the radiative term is also important, we introduce another restriction

$$\Delta t_3 < \min_j p_j / \mathcal{L}_j \quad , \tag{4.39}$$

where p_j is the pressure at the jth grid point and $\mathcal{L}_j$ is the radiative

losses there. Combining these three criteria, we adjust the time increment at each time t so that

$$\Delta t < \text{Min } (\Delta t_1, \Delta t_2, \Delta t_3) \quad . \tag{4.40}$$

The spatial grid spacing, Δx, is kept fixed throughout a run in order to assure proper centering of the difference equations. From symmetry arguments, Section 4.2, only half the loop need be included. We use 33 points for the x-grid; hence, for a loop of height 2×10^9 cm., the average width of each grid interval is 700 km. The width of a particular interval, i.e. of a particular slab of plasma, depends on the density and area at that point; from equation (4.7) we have:

$$\Delta s \approx \frac{\Delta x}{nA(s)} \quad . \tag{4.41}$$

Equation (4.41) implies that in regions where the density is high or the area large, such as in a condensation at the top of the loop, the Eulerian spacing of the grid is finer. As mentioned previously, this is the main advantage to using a Lagrangean coordinate system.

For the temperatures, densities and sizes of typical loops, and with 32 slabs for the x grid, we find that the time increment Δt, as determined by equation (4.41), ranges from $\Delta t \sim .05$ - .25 sec. To follow a typical loop from the 10^7 K temperature level until the time when most of the plasma has cooled and fallen onto the chromosphere requires $\sim$ 1 - 3 minutes of computer time on Stanford's IBM 370/168. A large fraction of this time is taken up during the initial conductive cooling stage of the loop when criterion (4.38) dominates. Unfortunately, the time for a run, τ_R, varies as a high power of the grid spacing. If

equation (4.38) is the important criterion, then $\tau_R \propto (\Delta x)^{-3}$; thus, we are severely limited in the possible fineness of the x grid. Details of our difference scheme along with a copy of the code are given in Appendix B.

5. COOLING OF FLARE LOOPS

5.1 General Evolution of Loops

From our computer calculations the following picture emerges of the evolution of a post-flare loop. The evolution can be divided into three distinct stages characterized by the behavior of the temperature profile. In the first stage – immediately after flare heating ends – the temperature is high enough so that conduction to the chromosphere dominates the energy losses. We expect that evaporation may also be an important cooling mechanism during this phase. During the first stage, the plasma is stable against the growth of thermal perturbations; hence, a smooth temperature profile develops. The scale height is so large that the loop is approximately isothermal, and the cooling rate varies as a high power of the temperature. These results also hold if evaporation is included (Antiochos and Sturrock, 1976b).

As the temperature decreases the effectiveness of conduction drops rapidly due to the strong temperature dependence of the thermal conductivity, equation (3.7), and eventually radiation begins to dominate the energy losses. The loop then enters the second stage of its development, during which radiation is the primary cooling mechanism. It is during this phase that thermal instabilities can occur; hence, the evolution of the loop during the second stage is highly complex involving large temperature gradients and plasma velocities. We find that the details of the evolution, in particular whether condensations form, are highly sensitive to the initial configuration of the loop plasma when it first enters the radiative cooling stage.

Since the density in post-flare regions is high, radiative losses are large and the temperature throughout a loop quickly drops to chromospheric values, $T \sim 10^4$ K. Once it reaches this value the temperature changes very little during the subsequent development of the plasma because the heat losses at low temperatures are insignificant. We define this phase of the evolution, during which the plasma remains isothermal at $\sim 10^4$ K, as the third stage. In this phase large density gradients and velocities are generated due to pressure forces and the effect of gravity.

In our model, the end point of the evolution is the establishment of a gravitational scale height atmosphere at 3×10^4 K. This does not agree with the true solar atmosphere since we have not included coronal heating in the calculations. For our large initial densities, the energy loss rate of the loop plasma is much larger than the estimated value of the coronal heating rate, $\leq 10^6$ ergs cm^{-2} s^{-1}, (Moore, 1972). However, once the loop plasma cools to chromospheric values and begins to fall onto the chromosphere, then the density in the upper part of the loop decreases until coronal heating once again becomes important. Therefore, we terminate our calculations when the density at the top of the loop drops by more than an order of magnitude from its initial value.

The time scales for the three stages of evolution are given by: (i) the conductive cooling time at high temperatures, $T \sim 10^7$ K; (ii) the radiative cooling time at $T \sim 10^6$ K; and (iii) the free-fall time along the loop. For typical loops, $n = 5 \times 10^{10}$ cm^{-3} and $H = 3 \times 10^9$ cm, these times are:

$$\text{(i)} \quad \tau_i = \frac{3/2\ pH^2}{\sigma T^{7/2}} \approx 10^3 \text{ s} \ , \tag{5.1}$$

$$\text{(ii)} \quad \tau_{ii} = \frac{3/2\ p}{n^2 \Lambda} \approx 10^2 \text{ s} \ , \tag{5.2}$$

$$\text{(iii)} \quad \tau_{iii} = \sqrt{\frac{2H}{g_\odot}} \approx 10^3 \text{ s} \ . \tag{5.3}$$

We note that the time scale for stage (ii) is shorter than the lifetimes of condensations in loop prominences $\sim$ 10 minutes; hence, the bright Hα knots cannot be due simply to a temperature difference along the loop, instead they must represent a density difference. Our calculations verify this hypothesis. We find that due to the thermal instability of the plasma, large temperature differences form; but, these die out quickly $\leq 10^2$ s. However, the temperature gradients give rise to density enhancements which persist for long times $\sim 10^3$ s, because the speed of sound is small at low temperatures. For example, in order for a condensation at 10^4 K to expand to a size of 10^9 cm at the sound speed, the time required is 10 min., which is of the same order as the lifetime of Hα knots.

In summary, we find that the evolution of post-flare loops is in three stages:

(i) conductive cooling (with or without evaporation) at high temperatures, $\sim 10^7$ K,

(ii) radiative cooling at lower temperatures, $\sim 10^6$ K,

(iii) the dynamics of isothermal plasma at chromospheric temperatures, $\sim 3 \times 10^4$ K.

The stability of a particular loop is, of course, determined by the second stage. In the rest of this chapter we describe each of these

stages in detail, and determine under what conditions will thermal instability significantly affect the evolution of loop plasma.

5.2 Conductive Cooling Stage

5.2.1 Conductive Damping Rate

During the initial phase of flare cooling the temperature is high enough so that the conduction term dominates in the dispersion relation, equation (1.14). Therefore, we expect perturbations to be damped on a time scale,

$$\tau_D \approx \frac{3/2\ p}{\kappa T(\frac{2}{\lambda})^2} \quad , \tag{5.4}$$

since τ_D is the time scale for temperature differences over lengths $\lambda/2$ to be significantly reduced by conduction. We tested this result by examining the behavior of a perturbation of small wavelength but with a finite amplitude. The perturbation was chosen to be initially isobaric with an amplitude of 9.75% and a wavelength $\lambda = 2 \times 10^9$ cm. The loop was assumed to be due to a point dipole source, with a height above the chromosphere of 3×10^9 cm and a compression factor $\Gamma = 10$. For this choice of height and Γ, the loop length turns out to equal 4 wavelengths of the perturbation. The initial average temperature and density assumed were $T = 10^7$ K and $n = 5 \times 10^{10}$ cm^{-3}.

In Figure 5.1, the evolutions of the amplitudes of the temperature and density variations are shown. We note that the damping time for the temperature perturbation is ~ 5 sec., which is in good agreement with eq. (5.4); however, the evolution of the density is very different from that of the temperature. The initial response of the density profile lags behind that of the temperature due to the inertia of the

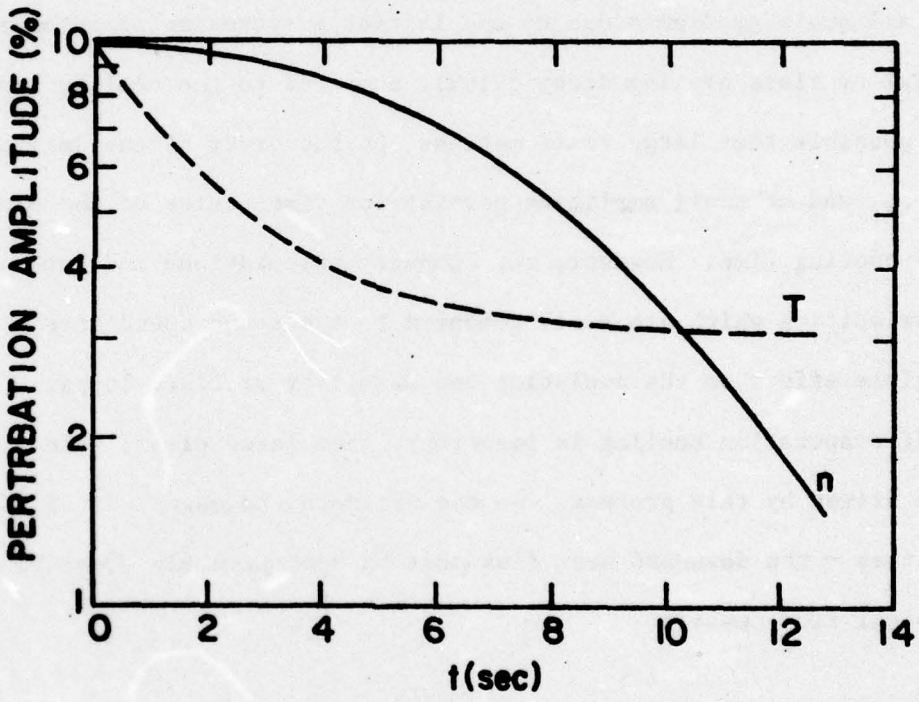

Figure 5.1 EVOLUTION OF THE AMPLITUDE OF A TEMPERATURE AND DENSITY PERTURBATION THAT IS DAMPED BY CONDUCTION. The solid line refers to the density perturbation and the broken line refers to the temperature perturbation.

plasma. The maximum velocity generated by the resulting pressure gradients is $\sim 3 \times 10^6$ cm s^{-1}, which is an order of magnitude less than the sound speed.

By t = 14 sec. we note from Figure 5.1 that the amplitude of the perturbation has dropped by over 60%, whereas, the thermal energy of the loop has decreased due to conduction out the base and radiation by less than 1%. The short damping time implies that we are justified in assuming an isothermal and static initial state for the loop plasma. All small scale gradients due to the initial evaporation of chromospheric material by flare heating decay quickly compared to the cooling time. It is possible that large scale motions, on the order of the length of the loop, and of small amplitude persist for time scales on the order of the cooling time. However, our computer calculations indicate that velocities which are small compared to the sound speed have negligible effect on the evolution and stability of flare loops.

If evaporation cooling is important, then large plasma velocities may be driven by this process. We can estimate the magnitude of these velocities – the downward heat flux must be approximately equal to the mechanical flux upwards,

$$pv \approx F \quad . \tag{5.5}$$

Taking the heat flux to be of order 10^8 - 10^9 ergs cm^{-2} s^{-1} for large and small loops, respectively, and the pressure $\sim 10^1$ - 10^2 ergs cm^{-3}, we obtain,

$$v \approx 10^7 \text{ cm } s^{-1} \quad . \tag{5.6}$$

Since the sound speed at 10^7 K is 50 km s^{-1}, the Mach number is $M = v/c = .2$, and the ratio of kinetic to thermal energy is only .04. In addition, we expect that since the heat flux $F \propto T^{7/2}$, the Mach number $M \propto T^3$, if the pressure is constant, or $M \propto T^2$, if density is constant. In either case we note that the Mach number varies as a high power of T; hence, even if the evaporation velocities are comparable to the sound speed when the loop temperatures are high, these velocities will be negligible when the temperature drops low enough so that radiative cooling dominates.

5.2.2 Static and Evaporative Cooling Rates

The first stage cooling of flares has been investigated by several authors: Culhane et al. (1970), Strauss and Papagiannis (1971), and Zaumen and Acton (1974). In their models they assumed that a loop has uniform cross-section; however, Antiochos and Sturrock (1976a) point out that for magnetic fields typical of flare loops (Rust and Bar, 1973), the variation of area along the loop has a significant effect on the cooling. Antiochos and Sturrock have calculated the evolution of the temperature and density profiles both for static and evaporative (1976b) models; they assume that gravitational and radiative effects are negligible and that all velocities are small so that pressure gradients are unimportant. With these assumptions the MHD equations simplify sufficiently so that analytic solutions may be obtained.

For completeness we state the important results of the calculations by Antiochos and Sturrock below. In the case of static cooling of a dipole loop, the temperature profile is given by

$$T(\theta,t) = T(0,0)(1 + t/\tau)^{-2/5} \left[1 - \left(\frac{\nu(1 - \nu_b^2)}{\nu_b(1 - \nu^2)}\right)^2\right], \qquad (5.7)$$

where ν has been defined in equation (3.27) and the subscript "b" refers to values at the base of the loop. The cooling time τ is given by

$$\tau = 10^6 \, p(0) \left(T(0,0)\right)^{-7/2} R^2 \frac{\nu_b^2}{(1 - \nu_b^2)^2} \quad , \qquad (5.8)$$

where R is the radius of the loop, Figure (3.1). The parameter ν_b is directly related to the compression factor Γ — the dependence of τ on Γ is given in Figure 2 of Antiochos and Sturrock (1976a). For the case of evaporative cooling, the results are similar except that the temperature varies as $(1 + t/\tau)^{-2/7}$ and at low temperatures the heat flux varies linearly with T rather than being constant as in the static case.

We ran our code for a dipole loop with $\Gamma = 10$ and $R = 2.5 \times 10^9$ cm, in order to compare our model with the results above. The initial temperature and density were chosen as 1.05×10^7 K and 2.5×10^{10} cm^{-3}, respectively. With these values the cooling time given by equation (5.8) is 200 sec. In Figure 5.2 we plot $\left(\frac{\bar{T}(t)}{\bar{T}(0)}\right)^{-5/2} - 1$ versus t, where $\bar{T}$ is the average temperature of the loop in our computer run. We note that the graph is linear in agreement with equation (5.7) and that the cooling time is 170 sec. which also agrees with theory. The loop size and plasma density were deliberately chosen to be small so that radiative cooling would be negligible. We find that the plasma loses 32% of its thermal energy in 270 sec., with 88% of the loss due to conduction and the rest via radiation.

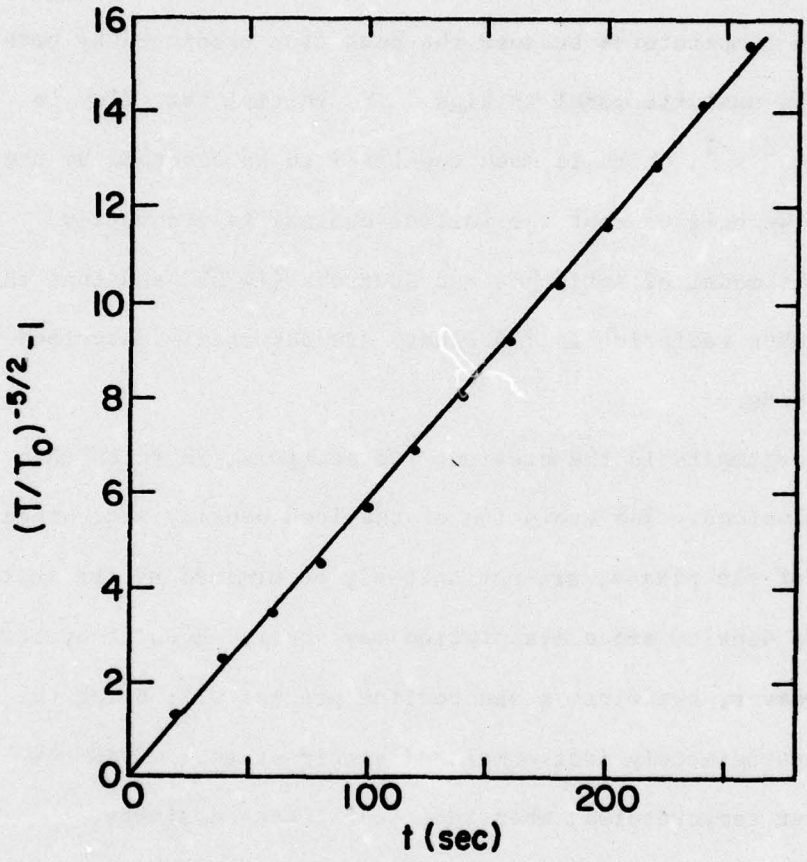

Figure 5.2 COMPARISON OF ANALYTIC CONDUCTIVE COOLING MODEL WITH OUR NUMERICAL RESULTS. PLOT OF $(T/T_0)^{-5/2}-1$ VERSUS t.

These results indicate that in the limit of small radiative losses and plasma velocities our numerical code does reproduce the analytic calculations. Of course, this cannot be used as an argument to prefer static over evaporative cooling since our model assumes no evaporation. In fact, we expect that evaporation is probably the dominant cooling process at high temperatures because the heat flux predicted by both our code and the analytic model is high. The initial heat flux is 2×10^9 ergs cm^{-2} s^{-1}, which is much too large to be absorbed by the chromosphere. We believe that the initial cooling is accurately described by the model of Antiochos and Sturrock (1976b) and that the later stages, when radiation is important, are accurately described by our numerical code.

From the arguments in the previous two sections, we reach the following conclusions. The evolution of the loop density and, hence, the stability of the plasma, are not uniquely determined by the initial temperature and density since evaporation may occur. Even if evaporation is present, however, the first stage cooling process will bring the loop into an approximately isothermal and static state. Given the density at lower temperatures, when radiation losses dominate, the stability may be determined. In the next section we discuss necessary criteria on the density and temperature profiles for the formation of condensations.

5.3 Instability Criteria

Using our model of flare loops, we have determined criteria under which thermal instabilities in a coronal plasma can grow. The term instability is not strictly applicable to our model since the plasma

is never in an equilibrium state but is continuously evolving; however, we use it to denote situations in which the cooling is highly non-uniform. By the term "unstable loop", we mean that a condensation observable in Hα and of small size scale forms. Specifically, we require that the condensation be at least an order of magnitude brighter in Hα than the rest of the loop and have a lifetime of the order of minutes. These condensations correspond to the bright knots in Hα that are often observed to form at the tops of loop prominences (Section 2.2.4).

We find that the following conditions are necessary for a loop to be unstable (according to the definition above):

(1) Since both the growth time of thermal perturbations and the lifetime of a loop are of the order of the radiative cooling time, only perturbations of finite amplitude can lead to observable effects. However, we find that the amplitude required is quite small, of order 5%.

(2) From linear theory (Section 1.2), we require that the growth rate due to radiative cooling dominates the damping rate due to conduction. Hence from equations (1.19) and (1.20) we require,

$$n\lambda \geq 4 \times 10^{-3} \, T^{7/4} \, \Lambda^{-1/2} \, cm^{-2} \quad , \tag{5.9}$$

where λ is the wavelength of the perturbation and Λ is the radiative loss function.

(3) In order for a density perturbation to grow, the cooling time must be long compared to the speed of sound travel time across the perturbation; hence from equation (1.23),

$$n\lambda \leq 4 \times 10^{-11} \, T^{3/2} \, \Lambda^{-1} \, cm^{-2} \quad . \tag{5.10}$$

(4) Additionally, we find that for temperatures and size scales relevant to loop prominences, the number density in a loop must be greater than approximately 10^{10} cm^{-3}. For densities less than this value the radiative cooling time is so long that gravitational effects and conduction to the chromosphere dominate the cooling process, stopping the growth of condensations. Also, for low densities coronal heating becomes important and, hence, our model is no longer accurate.

The conditions enumerated above agree well with observations that loop prominences occur only after flares when the coronal density is enhanced and only on large loops of size scales $\geq 10^9$ cm. In Figure (5.3) we graph the relations (2) and (3). Inequality (2) is valid in the region to the left of the broken line labeled (ii) and inequality (3) is valid to the right of the line labeled (iii). In the region between line (ii) and (iii) isobaric perturbations will grow. If conditions (1) and (4) are satisfied as well, then observable condensations will result.

5.4 Radiative Cooling Stage

5.4.1 Comparison with Linear Theory

We define the second stage of the cooling process to be that phase during which radiation is the dominant energy loss mechanism. At the onset of instability, we expect that the linear theory may approximately describe the evolution. In order to compare our nonlinear model with this theory, we followed with our code the evolution of an initial perturbation in the temperature and density profile of a loop. The loop was chosen in each case to be that due to a dipole field with a compression factor, $\Gamma = 10$. The perturbation was chosen in each case to be initially

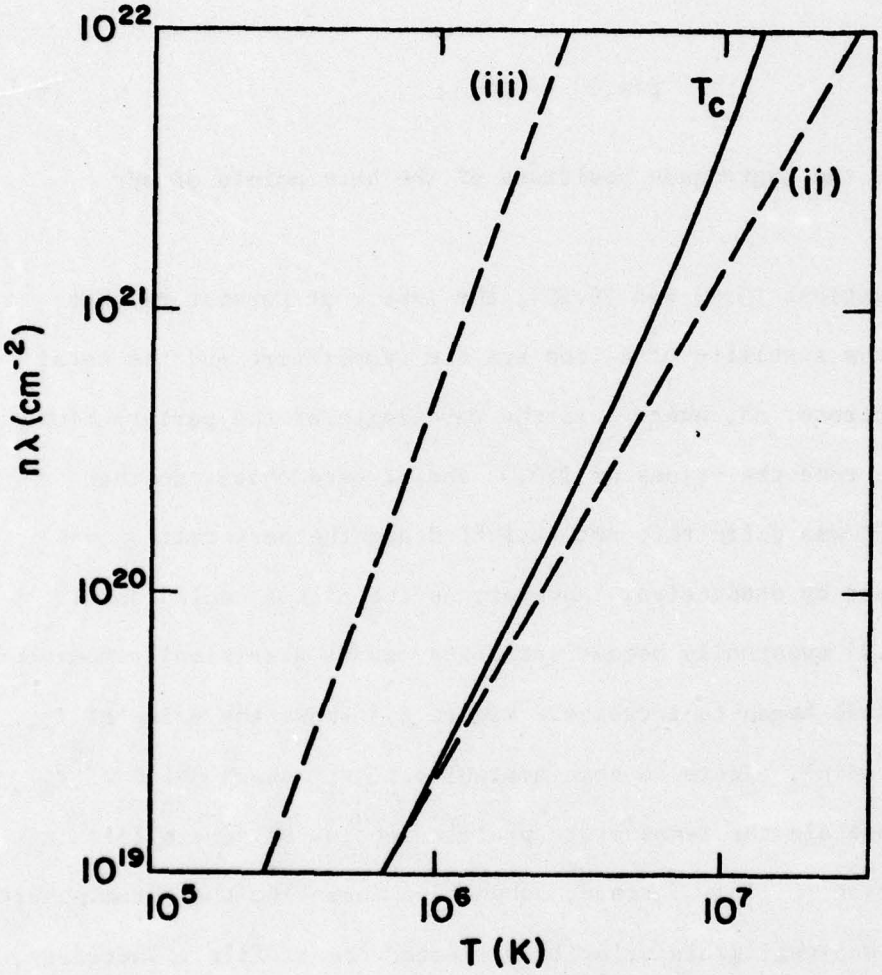

Figure 5.3 GRAPH OF INSTABILITY CRITERIA, (2) AND (3), AND GRAPH OF TEMPERATURE OF INSTABILITY ONSET, T_c COMPUTED FROM OUR MODEL.

isobaric, with an amplitude of 10% and a wavelength equal to the length of the loop, i.e. we assumed as initial conditions:

$$T(x,0) = T(0,0)\left\{1 - .1\cos\left(\frac{\pi x}{x_m}\right)\right\} \tag{5.11}$$

and

$$p(x,0) = p(0,0) \quad , \tag{5.12}$$

where $\pm x_m$ are the Lagrangean positions of the base points of our model loop.

From conditions (5.9) and (5.10), the important parameters that characterize the stability of a loop are the temperature and the total number of electrons, $n\lambda$, where λ is the wavelength of the perturbation. In each of the runs the values of $T(0,0)$ and $n\lambda$ were chosen so that condition (5.9) was definitely not satisfied and the perturbation was initially damped by conduction. However, as the plasma cooled and T decreased, (5.9) eventually became satisfied and at a critical temperature T_c, the amplitude began to increase. Figure 5.3 shows the value of T_c as a function of $n\lambda$. There is some ambiguity in the exact value of T_c since in no case did the temperature profile retain the simple form given by equation (5.11). Instead, conductive losses to the chromosphere and small but non-negligible velocities altered the profile. Therefore, we assumed that the temperature and density variations were due to two parts,

$$\left.\begin{aligned} \frac{\Delta T}{T} &= \left(\frac{\Delta T}{T}\right)_a + \left(\frac{\Delta T}{T}\right)_i \\ \frac{\Delta n}{n} &= \left(\frac{\Delta n}{n}\right)_a + \left(\frac{\Delta n}{n}\right)_i \end{aligned}\right\} \tag{5.13}$$

where $\left(\frac{\Delta T}{T}\right)_a$ and $\left(\frac{\Delta n}{n}\right)_a$ indicate variations due to adiabatic motions of the plasma and $\left(\frac{\Delta T}{T}\right)_i$, $\left(\frac{\Delta n}{n}\right)_i$ indicate the amplitude of the isobaric perturbation. Since for adiabatic motions

$$\left(\frac{\Delta T}{T}\right)_a = \frac{2}{3}\left(\frac{\Delta n}{n}\right)_a \quad , \tag{5.14}$$

the perturbation amplitude is given by

$$\left(\frac{\Delta T}{T}\right)_i = -\left(\frac{\Delta n}{n}\right)_i = \frac{3}{5}\frac{\Delta T}{T} - \frac{2}{5}\frac{\Delta n}{n} \quad . \tag{5.15}$$

Hence, we define T_c as the average temperature in the loop at which the value of $\left(\frac{\Delta T}{T}\right)_i$, as given by equation (5.15), began to increase.

In general the results of our computer calculations agree well with theory. We find that T_c is approximately independent of n or λ as long as the product $n\lambda$ is constant. From Figure 5.3 we note that the effect of the nonlinearities in our model is to increase the stability of the loop especially at high temperatures. This is to be expected since for the initial perturbation with the longest possible wavelength, and, hence, the fastest growth rate (equation 5.11), the temperature maximum occurs at the base of the loop. Conduction cooling to the chromosphere decreases the temperature near the base, thereby decreasing both the amplitude and the length scale of the temperature variations. We find that loops with a large compression factor Γ can support a perturbation with a relatively larger wavelength because heat losses to the chromosphere are reduced; hence, they are more susceptible to instability, i.e. T_c increases with Γ. Once instability sets in, however, the evolution of the plasma is insensitive to Γ.

In all cases we find that pressure balance is maintained for only a short, initial part of the cooling. As can be seen in Figure 5.3, the

temperature T_c occurs near the line labelled at which condition (5.10) breaks down and the perturbation can no longer remain isobaric. Therefore, significant velocities soon develop. In the next section we investigate the growth of these velocities using an analytic model of a growing condensation.

5.4.2 Analytic Model of a Condensation

We have constructed a simple analytic model to follow the growth of a condensation into the nonlinear regime. The model is valid during the initial growth when pressure equilibrium is maintained, i.e.

$$\nabla p \approx 0 \quad . \tag{5.16}$$

Equation (5.16) will be valid as long as the speed of sound and the gravitational scale height are large compared to relevant velocities and size scales. This model can be used to calculate the temperature at which velocities resulting from the difference in cooling rates between the cold and the hot plasma become appreciable and, hence, pressure equilibrium breaks down. In addition, we can obtain estimates of the magnitude of this velocity and determine if shocks form. Of course, these results can also be obtained using our full computer code; however, we find that the analytic model is useful both to check the computer calculation and to clarify the important features of the nonlinear instability.

We assume that the temperatures are low enough so that heat conduction is negligible compared to radiative losses. Therefore the hot and the cold regions, Figure 5.4, may be taken to be separated by a boundary of negligible width. Within each region the temperature

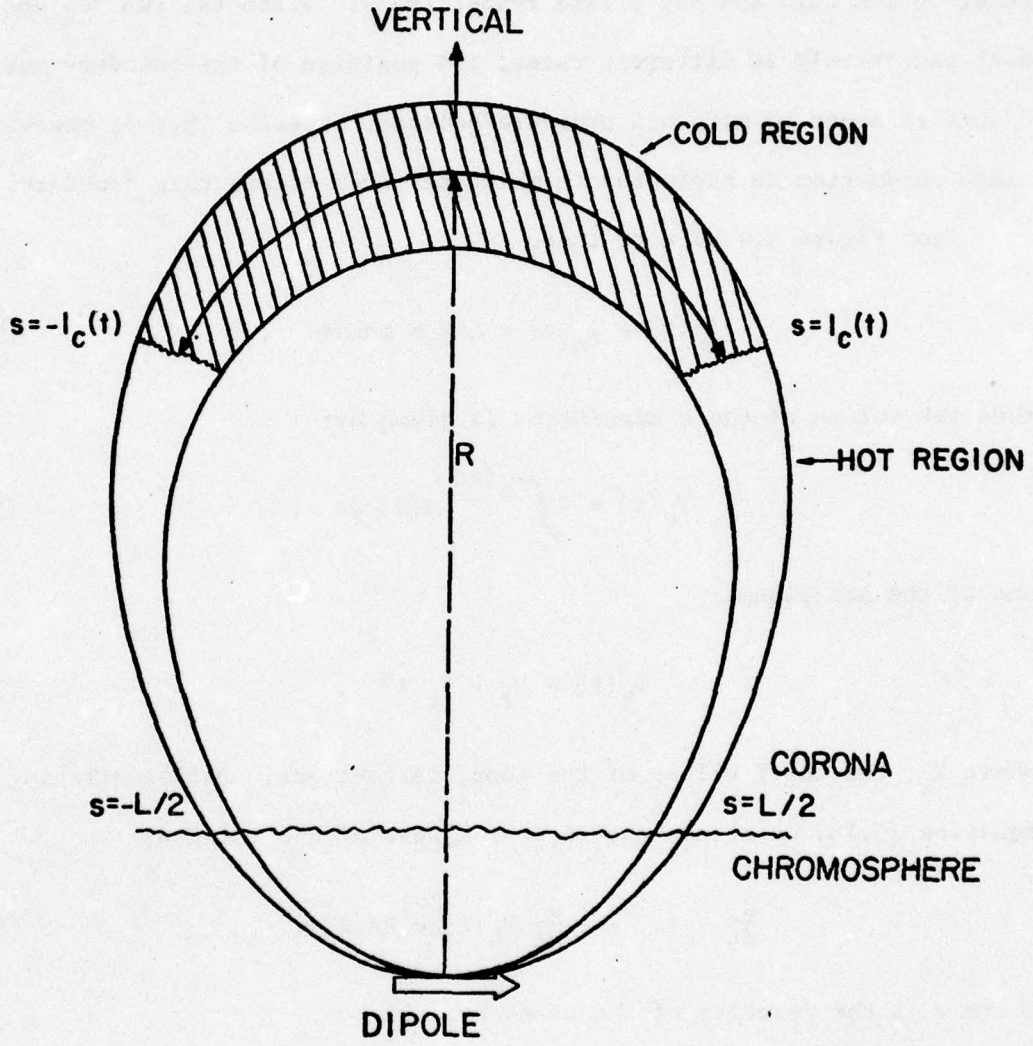

Figure 5.4 GEOMETRY OF OUR ANALYTIC CONDENSATION MODEL.

and density are assumed to be approximately uniform and given by, $\left(T_c(t),\ n_c(t)\right)$ and $\left(T_h(t),\ n_h(t)\right)$ where the subscripts "c" and "h" refer to the cold and hot plasma respectively. Since the two regions cool radiatively at different rates, the position of the boundary must change in order to maintain pressure balance, equation (5.14); however, since conduction is neglected no material moves across this boundary.

From Figure 5.4 we note that,

$$\ell_c(t) + \ell_n(t) = L/2 = \text{const.} \quad , \tag{5.17}$$

thus the volume of the condensation is given by:

$$V_c(t) = 2\int_0^{\ell_c(t)} A(s)\, ds \quad , \tag{5.18}$$

and of the hot plasma:

$$V_h(t) = V_T - V_c(t) \quad , \tag{5.19}$$

where V_T, the total volume of the loop, is constant. Differentiating equation (5.18) we obtain the rate of change of the volumes:

$$\frac{d}{dt} V_c(t) = -\frac{d}{dt} V_h(t) = 2A(\ell_c)v \quad , \tag{5.20}$$

where v is the velocity of the boundary,

$$v = \frac{d}{dt} \ell_c(t) \quad . \tag{5.21}$$

Since the temperature and density are uniform over each region, we can integrate the mass equation over the volume of the condensation:

$$\int_{V_c} \frac{d}{dt} n_c(t)\, d^3V + \int_{V_c} n_c(t)\, \nabla \cdot \vec{v}\, d^3V = 0 \quad . \tag{5.22}$$

Using the divergence theorem on the second term of equation (5.22) and substituting equation (5.20) yields,

$$V_c(t) \frac{d}{dt} n_c(t) + n_c(t) \frac{d}{dt} V_c(t) = 0 \quad , \tag{5.23}$$

therefore,

$$n_c(t)\, V_c(t) = \text{const.} \tag{5.24}$$

Equation (5.24) is equivalent to the assumption that there is no mass transfer between the hot and cold regions. This can only be true if the cold plasma cools faster than the hot, i.e. the temperature must be in the unstable regime of the cooling curve. Once the temperature enters the stable regime, the profile must eventually become uniform throughout the loop.

The heat equation can be integrated in a similar manner as the mass equation; yielding

$$\frac{3}{2} V_c \frac{dp}{dt} + \frac{5}{2} p \frac{d}{dt} V_c = - \Lambda_0 n_0^2 T_0^{-\alpha} V_c \quad , \tag{5.25}$$

where we have assumed a radiative loss function of the form,

$$\mathfrak{L}(n,T) = \Lambda_0 n^2 T^{-\alpha} \quad . \tag{5.26}$$

Defining,

$$\lambda_c(t) = V_c(t)/V_T \tag{5.27a}$$

and

$$\lambda_h(t) = V_h(t)/V_T \quad , \tag{5.27b}$$

we obtain the following set of equations:

$$\left.\begin{aligned} &\lambda_c(t) + \lambda_h(t) = 1 \\ &n_{c,h}(t)\,\lambda_{c,h}(t) = N_{c,h} = \text{const.} \\ &\frac{3}{2}\lambda_{c,h}\frac{d}{dt}p + \frac{5}{2}p\frac{d}{dt}\lambda_{c,h}(t) = -\Lambda_0 n_{c,h}^2 T_{c,h}^{-\alpha}\lambda_{c,h} \\ &p = 2kn_{c,h}T_{c,h} \end{aligned}\right\} \tag{5.28}$$

The seven independent equations in the system (5.28) are enough to uniquely determine the variables (n_c, T_c, λ_c), (n_h, T_h, λ_h) and p for given initial conditions.

The quantity that is of interest is

$$\xi(t) \equiv T_c(t)/T_h(t) \quad , \tag{5.29}$$

the ratio of cold to hot temperature. (The amplitude of the perturbation is equal to $(1 - \xi)/(1 + \xi)$.) After some manipulation, the two heat equations in (5.28) can be decoupled and integrated to yield,

$$F(\xi) = F(\xi_0) - \beta(\xi_0)t/\tau \quad , \tag{5.30}$$

where

$$F(\xi) = \int\left[1 - \xi^{\alpha+2}\right]^{-\frac{8(\alpha+1)}{3(\alpha+2)}} \xi^{\alpha+1}\,(\eta + \xi)^{\frac{2\alpha-1}{3}}\,d\xi \quad , \tag{5.31}$$

$$\beta(\xi_0) = \frac{2}{5}\left[1 - \xi_0^{\alpha+2}\right]^{-\frac{5(\alpha+1)}{3(\alpha+2)}} \xi_0^{\alpha+2}\,(\eta + \xi_0)^{\frac{2\alpha-1}{3}} \quad , \tag{5.32}$$

$$\tau = \frac{p(0)}{\Lambda_0 \, n_c^2(0) \, T_c(0)} \quad , \tag{5.33}$$

and

$$\eta = N_H / N_c \quad . \tag{5.34}$$

There are two adjustable parameters in our solution, η, the ratio of the total number of cold particles to hot and, ξ_0, the initial temperature ratio $\xi(0)$. We are interested in initial perturbations of small amplitude and large wavelengths; hence,

$$.9 \leq \xi_0 < 1 \quad \text{and} \quad \eta \approx 1 \quad . \tag{5.35}$$

For example, an initial perturbation with an amplitude of 5% and a wavelength equal to the length of the loop corresponds to $\xi_0 = .9$ and $\eta = 1$.

In deriving equations (5.30) and (5.31), we assumed that the exponent, α, of T in the radiative loss function (equation (5.26)), is a constant. From Cox and Tucker's (1969) results, Figure 1.1, we note that α is actually a function of T; however, we can approximate the cooling function by segments with constant α as in Moore and Fung (1972) and Goldsmith (1971). Since the cooling function is probably only accurate to at best a factor of two, the approximation of constant α will not affect the general results of our model.

The time dependence of ξ can be determined from equation (5.30) and (5.31); however, they break down for $\alpha = -2$ as can be seen from the form of (5.31). This is to be expected since we assumed that the loop is unstable to the growth of the condensation, but for a cooling function

of the form given by equation (5.26), Field's (1965) criterion,

$$\frac{\partial \mathcal{L}}{\partial T} - \frac{n}{T}\frac{\partial \mathcal{L}}{\partial n} < 0 \tag{5.36}$$

is not satisfied for $\alpha \leq -2$. Thus, our solution is only valid for $\alpha > -2$. For certain α equation (5.31) can be integrated directly:

$$F(\xi) = \begin{cases} \dfrac{1}{1+\eta}\ \ell n\left(\dfrac{\eta+\xi}{1-\xi}\right) & \text{for } \alpha = -1 \\ \dfrac{2}{5}\left[1-\xi^{5/2}\right]^{-1} & \text{for } \alpha = 1/2 \\ \dfrac{1}{5}\left[1-\xi^{4}\right]^{-5/4}(\eta+\xi^{5}) & \text{for } \alpha = 2 \end{cases} \tag{5.37}$$

From the Cox and Tucker curve we find that $1/2 \leq \alpha \leq 2$ in the unstable temperature regime, $10^5 \leq T \leq 10^7$.

In Figure (5.5) we plot ξ as a function of t/τ for each of the three values of α in equation (5.37) and for $\eta = 1$, $\xi_0 = .9$. We note from Figure (5.5) that for $\xi \leq 10^{-1}$, ξ is a very rapidly decreasing function of t. Since the plasma tries to maintain pressure balance between the hot and cold regions, we will find that the sharp decrease in ξ implies equally rapid changes in the density and hence, supersonic velocities result. The results in Figure (5.5) are not sensitive to the value of η or ξ_0. Defining t_f as the value of t when $\xi = 0$, we find from equation (5.30), (5.32) and (5.37) that for $\alpha = 1/2$, $t_f = 1$, independent of η or ξ_0. For $\alpha = 2$, $t_f \to$ const. as $\eta \to \infty$ or 0, or as $\xi_0 \to 1$. For $\alpha = -1$, t_f diverges for $\eta \to 0$ or $\xi_0 \to 1$, but only logarithmically. (Also, we are mainly interested only in positive values of α.)

To obtain the time dependence of the other variables, we express

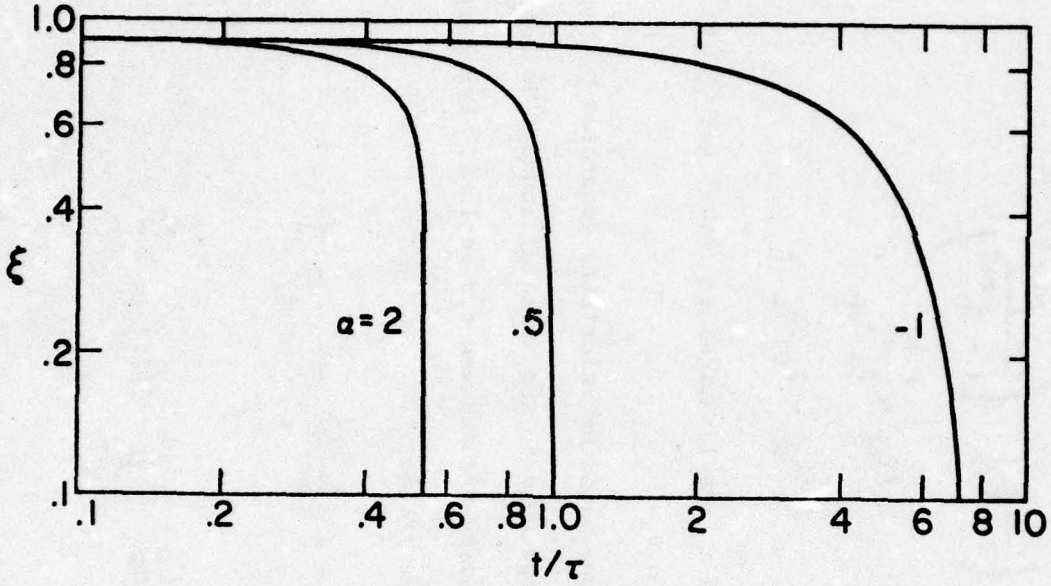

Figure 5.5 EVOLUTION OF THE TEMPERATURE RATIO, F FOR VARIOUS α. The initial amplitude $\xi_0 = .9$ and the ratio of hot to cold plasma, $\eta = 1$.

them in terms of ξ:

$$\lambda_c = \xi/(\eta + \xi) \quad , \tag{5.38}$$

$$p/p_0 = \left(\frac{\eta + \xi}{\eta + \xi_0}\right)^{5/3} \left(\frac{1 - \xi^{\alpha+2}}{1 - \xi_0^{\alpha+2}}\right)^{-\frac{5}{3(\alpha+2)}} \quad , \tag{5.39}$$

$$T_c/T_{c0} = \frac{p\ \lambda_c}{p_0\ \lambda_{c0}} \quad , \tag{5.40}$$

$$n_c/n_{c0} = \lambda_{c0}/\lambda_c \quad . \tag{5.41}$$

The equations for T_h and n_h are identical to (5.40) and (5.41) except that "c" is replaced by "h".

Our model breaks down when the velocities generated by the unequal cooling rates become comparable to the speed of sound. We calculate v, the velocity of the boundary between the two regions. Using equations (5.20), (5.27) and (5.38) yields,

$$v = -\frac{L\ \langle A \rangle}{2A(\ell_c)} \frac{\eta}{(\eta + \xi)^2} \frac{d\xi}{dt} \quad , \tag{5.42}$$

where we have defined,

$$\langle A \rangle = \frac{2}{L}\int_0^{L/2} A(s)\ ds = \frac{V_T}{L} \quad . \tag{5.43}$$

Defining,

$$v_{th} = \frac{L}{2\tau} \quad , \tag{5.44}$$

and using equations (5.30) - (5.32) we obtain,

$$\left|\frac{v}{v_{th}}\right| = \frac{2}{5}\,\frac{\langle A\rangle}{A(\ell_c)}\,\frac{\left[1-\xi^{\alpha+2}\right]^{\frac{8}{3}\frac{\alpha+11}{(\alpha+2)}}}{\left[1-\xi_0^{\alpha+2}\right]^{\frac{5}{3}\frac{(\alpha+1)}{(\alpha+2)}}}\,\frac{\xi_0^{\alpha+2}}{\xi^{\alpha+1}}\,\frac{\eta(\eta+\xi_0)^{\frac{2\alpha-1}{3}}}{(\eta+\xi)^{\frac{2\alpha+5}{3}}} \quad . \tag{5.45}$$

If the loop is of constant cross-section then, of course, $\frac{\langle A\rangle}{A(\ell_c)} = 1$. In general, we expect this factor to be less than unity since A increases as λ_c (and hence ξ) decreases. For example, a dipole loop with a compression factor $\Gamma = 30$ and a volume for the condensed region, $\lambda_c = 1/10$, implies $\frac{\langle A\rangle}{A(\ell_c)} = .46$. Therefore, the variable area factor acts to decrease the velocity, improving the validity of our model. A lower limit on the size of the area ratio is

$$\frac{\langle A\rangle}{A(\ell_c)} \geq \frac{A(s = L/2)}{A(s = 0)} = \Gamma^{-1} \quad , \tag{5.46}$$

however, this ratio is usually much larger than Γ^{-1}. In the subsequent discussion we assume that $\frac{\langle A\rangle}{A(\ell_c)} \approx 1$.

We have plotted in Figure 5.6 $\left|\frac{v}{v_{th}}\right|$ as a function of ξ for $\eta = 1$ and $\xi_0 = .9$, and for several values of α. Assuming typical loop parameters, $T \sim 5 \times 10^6$ K, $n \sim 5 \times 10^{10}$ cm^{-3}, and $L \sim 10^9$ cm implies that $\frac{c}{v_{th}} \approx 10$; hence, our model will begin to break down at approximately this value for $\frac{v}{v_{th}}$. From Figure 5.6 we note that $\frac{v}{v_{th}} = 10$ corresponds to a value of ξ ranging from .4 - .2 for $.5 \leq \alpha \leq 2$. These values of ξ correspond to a perturbation amplitude of 43% - 67%. The temperatures, T_c and T_h, can be calculated for a particular ξ using equations (5.38) - (5.40). In Figure 5.7, T_c/T_{c0} and T_h/T_{h0} are plotted as functions of ξ for $\eta = 1$ and $\xi_0 = .9$. We note that for the values of ξ at which our model begins to break down, the condensation temperature has decreased by approximately a factor of 6 from its original value while the hot temperature has

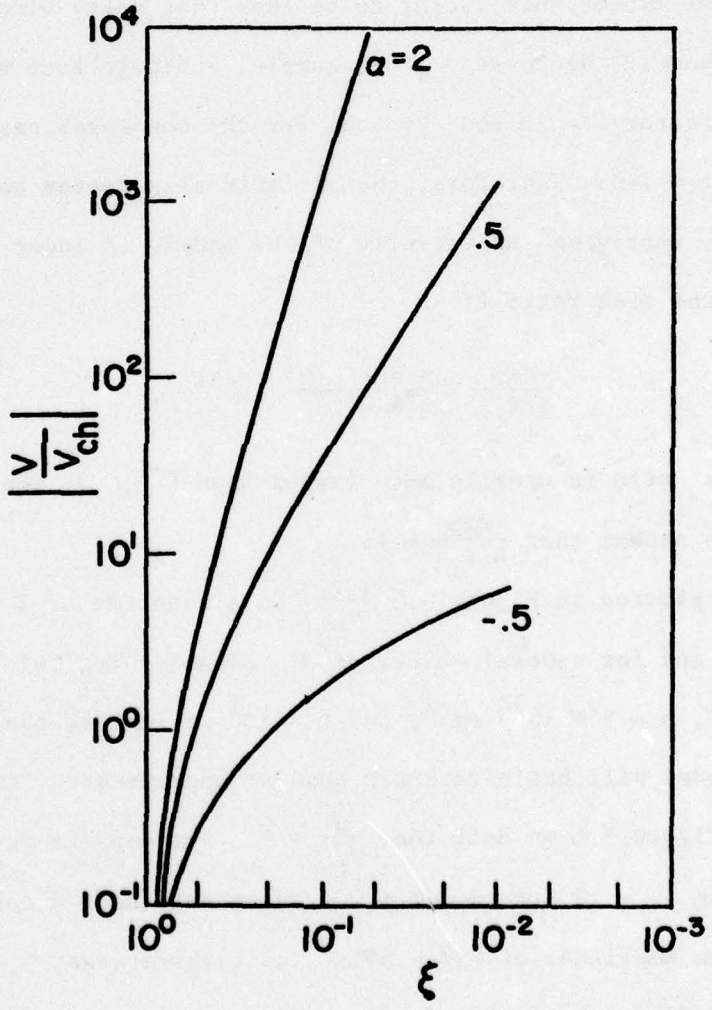

Figure 5.6 VELOCITY OF THE CONDENSATION BOUNDARY AS A FUNCTION OF ξ FOR VARIOUS α. The initial amplitude $\xi_0 = .9$ and the ratio of hot to cold plasma, $\eta = 1$.

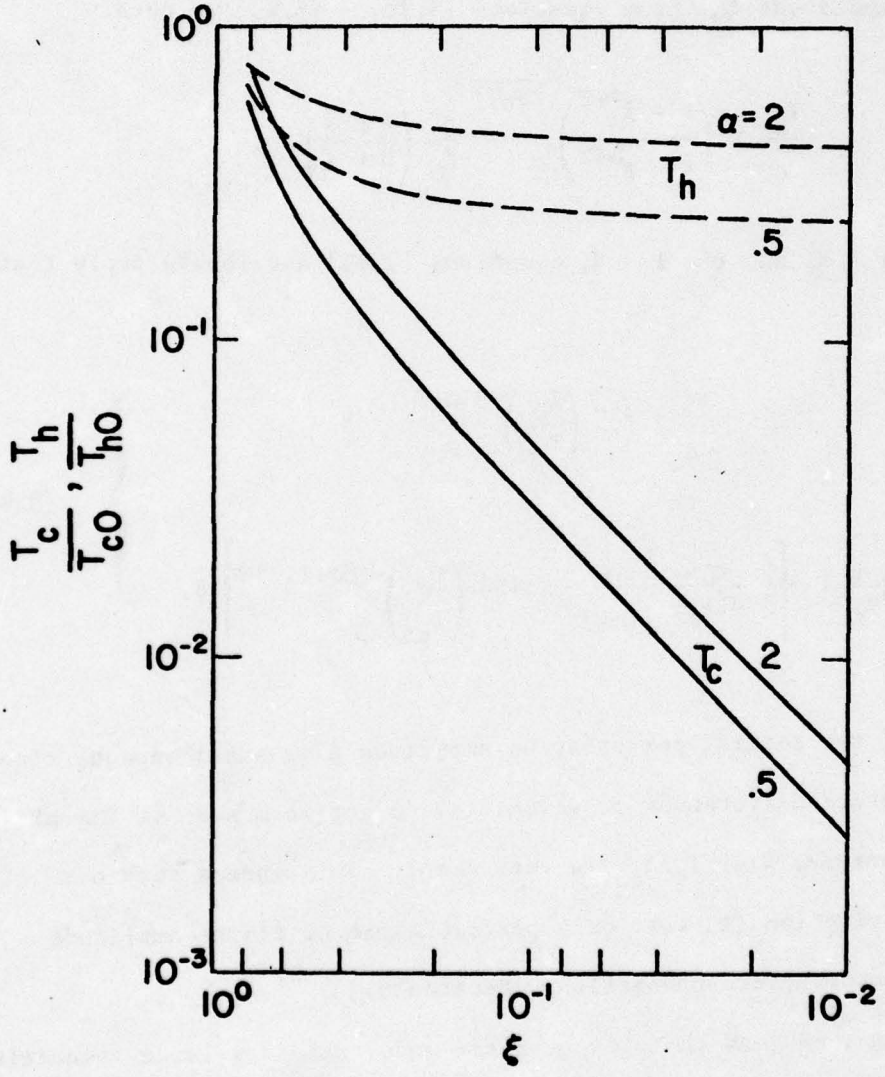

Figure 5.7 TEMPERATURES OF THE HOT, T_h, AND COLD, T_c, PLASMA AS A FUNCTION OF ξ. The solid lines refer to T_c and the broken lines refer to T_h.

dropped by a factor of 2. Since the plasma must cool over several decades in temperature (from 10^7 K to 10^4 K), we expect that large velocities (and probably shocks) will be present during most of the cooling.

It is instructive to examine the dependence of these results on the initial amplitude ξ_0. From equations (5.38) - (5.40) we obtain,

$$\frac{T_c}{T_{c0}} = \left(\frac{1 - \xi_0^{\alpha+2}}{1 - \xi^{\alpha+2}}\right)^{\frac{5}{3(\alpha+2)}} \frac{\xi}{\xi_0} \left(\frac{\eta + \xi}{\eta + \xi_0}\right)^{\frac{5}{3}} . \tag{5.47}$$

Letting $\delta = 1 - \xi_0$ and $\epsilon = 1 - \xi$, equations (5.45) and (5.47) imply that as $\delta \to 1$,

$$\left.\begin{aligned} \epsilon &\to \left(\frac{T_c}{T_{c0}}\right)^{-3(\alpha+2)/5} \delta \\ \text{and} \\ \left|\frac{v}{v_{th}}\right| &\to \left[\frac{2}{5} \frac{\langle A \rangle}{A(\ell_c)} \frac{\eta}{(\eta+1)^2} (\alpha+2) \left(\frac{T_c}{T_{c0}}\right)^{-(8\alpha+11)/5}\right] \delta . \end{aligned}\right\} \tag{5.48}$$

Therefore, if the initial perturbation amplitude δ is small enough, significant temperature differences or velocities do not form even if the plasma cools considerably, i.e. T_c/T_{c0} is very small. This agrees with our instability criterion (1) that only perturbations of finite amplitude can grow to observable condensations (Section 5.3).

In summary, we find that the analytic model predicts large velocities at the boundary between a condensation and the hot plasma in a loop. The growth rates of the temperature differences and the velocity are given by equations (5.30) and (5.45), and are plotted in Figures 5.5 and 5.6. For fairly small perturbation amplitude, $\sim 5\%$, the velocity becomes comparable

to the sound speed quite early in the cooling process – before the condensation temperature decreases by an order of magnitude. Therefore, our full computer code is necessary to investigate the behavior of the condensation at low temperatures.

5.4.3 Evolution of a Condensation

As discussed in the previous section, large velocities soon build up due to the non-uniform cooling. With our code we can follow the details of the temperature, density, and velocity profiles. In this section we investigate the evolution of an unstable loop throughout its radiative cooling stage. Although we only discuss the results for a particular loop in this section, the general features of the evolution turn out to be the same for all unstable loops. The only sensitive adjustable parameter is the amplitude of the initial perturbation; we describe its effect on the evolution in the following section.

The temperature and density profiles for a typical unstable loop at different times of its evolution are shown in Figures 5.8 and 5.9. The initial profiles were assumed to be of the form:

$$T(0,x) = T(0,0)\left(1 - .05\cos\left(\frac{\pi x}{x_m}\right)\right) , \qquad (5.49a)$$

and

$$n(0,x) = n(0,0)\left(1 + .05\cos\left(\frac{\pi x}{x_m}\right)\right) , \qquad (5.49b)$$

where x is the Lagrangean coordinate and $\pm x_m$ are the positions of the foot-points of our model. Equations (5.49a) and (5.49b) imply that the perturbation is approximately isobaric, centered at the top of the loop (x = 0), and of wavelength equal to the loop length. Since the

conduction damping rate varies inversely as the square of the wavelength, equation (5.4), we expect perturbations of the maximum possible wavelength to be most susceptible to thermal instability. The initial values were: $T(0,0) = 4 \times 10^6$ K and $n(0,0) = 5 \times 10^{10}$ cm^{-3}. The loop was taken to be that due to a dipole field with a compression factor of $\Gamma = 10$ and a total length of 80,000 km, which implies a maximum height above the chromosphere of 30,000 km. These parameters were chosen so that $T(0,0) \approx T_c$, the initial temperature for the onset of instability (Section 5.4.1).

From Figure 5.8 we note that by t = 480 sec the amplitude of the temperature variations has grown significantly; the temperature of the hot plasma has dropped to 1/3 of its original value, and the ratio of cold to hot temperatures, $\xi = .37$. However, the ratio of minimum to maximum density (Figure 5.9) at this time is only .73; hence, the temperature perturbation has begun to run away from the density variations. The plasma velocities are still small, the maximum velocity is $- 1.5 \times 10^6$ cm s^{-1} (directed up the loop) which implies a Mach number, $M = 10^{-1}$.

We find that the condensation now enters a very rapid cooling stage, so that ξ decreases drastically. This behavior is in agreement with our analytical calculations in the previous section. By t = 490 sec the top 5,000 km of the loop have dropped to chromospheric temperature, 3×10^4 K. At this time the loop top becomes visible in Hα. Comparing the temperature profile at t = 480 and t = 490 sec, we see that it requires < 10 sec for the condensation to cool from $\sim 5 \times 10^5$ K to its minimum temperature. (We fix the temperature so that it cannot drop below 3×10^4 K – Section 3.3). The rapid cooling is due to the strong

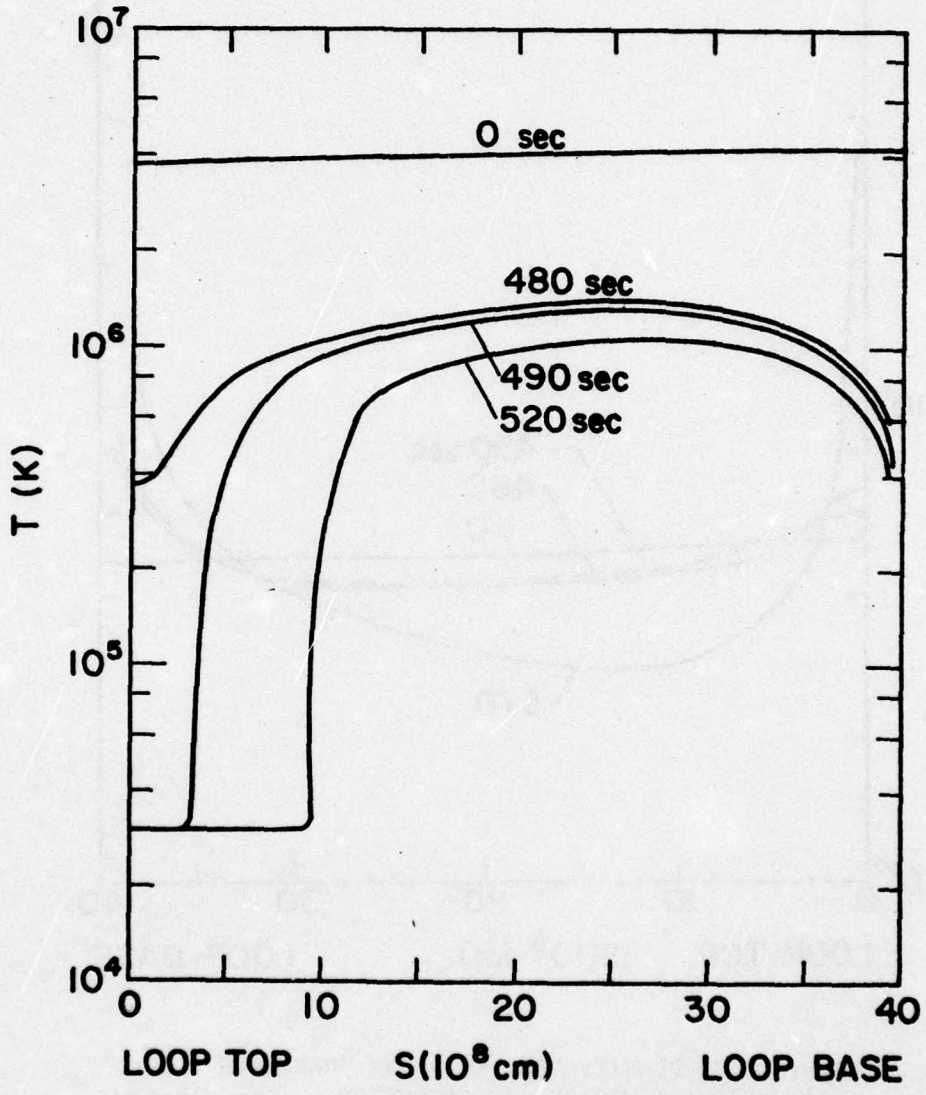

Figure 5.8 TEMPERATURE PROFILE OF AN "UNSTABLE" LOOP AT VARIOUS TIMES IN ITS EVOLUTION.

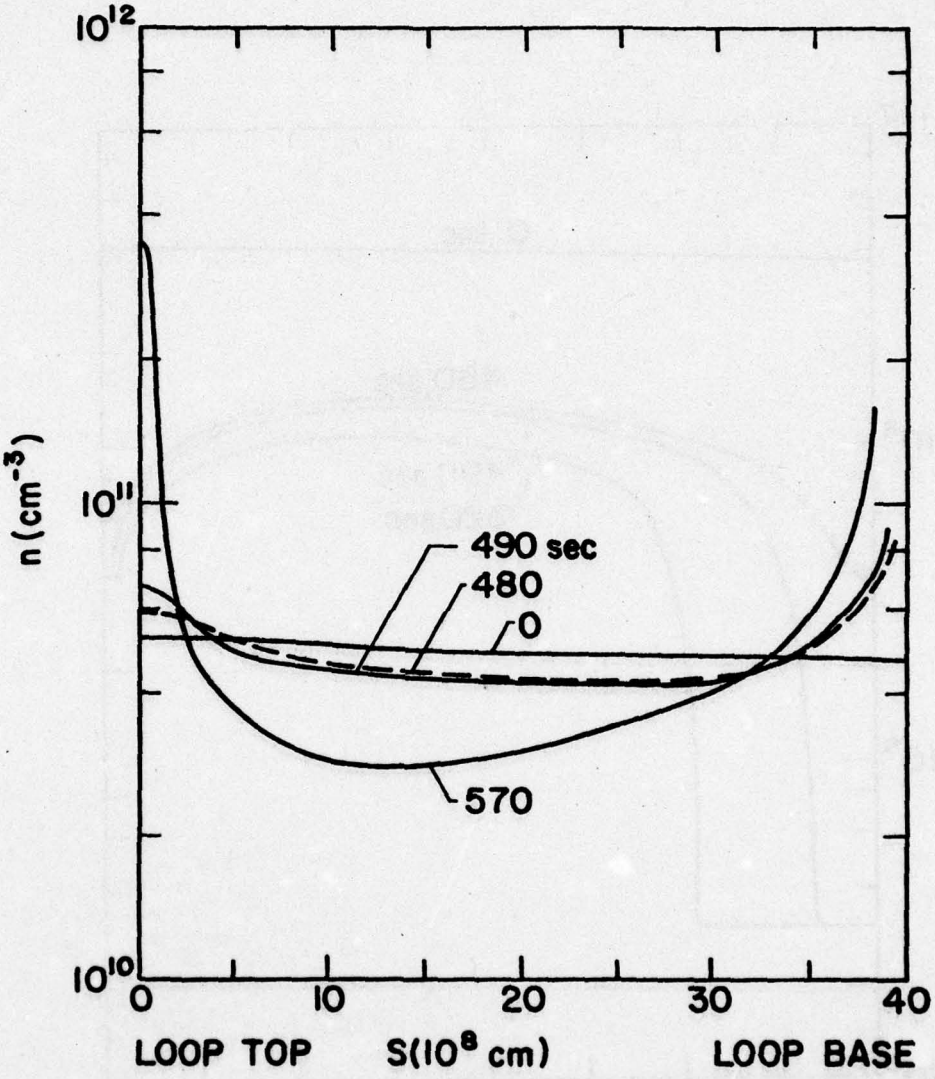

Figure 5.9 DENSITY PROFILE OF AN "UNSTABLE" LOOP AT VARIOUS TIMES IN ITS EVOLUTION. (For clarity the profile at t = 480 sec. is indicated by a broken line.)

radiative losses at low temperatures; the Cox and Tucker loss function peaks at about 2×10^5 K. For $T = 5 \times 10^5$ K and $n = 5 \times 10^{10}$ cm^{-3}, the theoretical cooling time $\tau = \frac{3/2\ p}{n^2 \Lambda} \approx 1$ sec.

On the other hand, the density does not change greatly between the times t = 480 to t = 490 sec, Figure 5.9. Hence, large pressure gradients result. This is to be expected since the velocities are too small to move a large mass of plasma in only 10 sec. The analytic model predicts that for these small values of ξ, $\leq 10^{-2}$, the velocities should be highly supersonic; however, that model neglects inertial effects while our computer calculations indicate that they are important. The maximum velocity at t = 490 sec is - 4.2×10^6 cm/sec, which is only slightly supersonic, but it is a factor of 3 increase over the value at t = 480 sec. Therefore, while the evolution of the loop is far from isobaric, it is also not isochoric; instead, we find that the dynamics of the plasma is critical in determining whether a long-lived condensation can result.

As the plasma continues to cool, the region at 3×10^4 K continues to expand until the complete loop reaches this temperature. This occurs at t = 530 sec. We note that it takes about 90 sec from the time that the top of the loop first drops to 3×10^4 K until all the plasma cools to this value. If the loop were of constant density, then in Hα the evolution of a condensation would appear to follow the temperature evolution. Since the length of the loop is 80,000 km, this would imply an average expansion velocity of the condensation at 450 km/sec, which is larger than observed velocities (Section 2.2.4). However, this is not the case because the density profile does not remain uniform, instead, large variations develop as a result of the non-uniform cooling.

We find that the maximum upward velocity during this phase of the cooling occurs at $t = 520$ sec at a point 9×10^8 cm from the top and is equal to -7.1×10^6 cm/sec. From Figure 5.8, we can see that the position of this velocity is at the boundary of the condensation. The speed of sound in the cold region is 3×10^6 cm/sec; hence, a weak shock occurs at the boundary, $M = 2$. The boundary density is approximately 4×10^{10} cm^{-3}; therefore, the mechanical energy flux into the condensation is of order 10^6 ergs cm^{-2} sec^{-1}. However, the radiative loss rate for the densities in the condensation is so high, $n^2\Lambda \geq 10^{-1}$ ergs cm^{-3} sec^{-1}, that the mechanical energy flux is easily dissipated without significant effect on the temperature of the condensation.

In Figure 5.9, we show the density profile at $t = 570$ sec, when the temperature profile is uniform at 3×10^4 K. As a result of the dynamics, a large density gradient has developed at the top of the loop. The density over most of the loop volume is approximately 3×10^{10} cm^{-3}; however, a small, $< 10^8$ cm, clump of plasma has formed at the top with densities an order of magnitude higher. The clump contains 25% of the total mass of loop plasma. Since the radiative losses vary as n^2, the compression at the top would appear to be as much as 2 orders of magnitude brighter in Hα than the sides of the loop (assuming the loop is observed at the solar limb).

We believe that this compression corresponds to the bright knots in Hα observed at the beginning of a loop prominence event, Section 2.2.4. The time scale for temperature variations, ≤ 90 sec, is too short to account for the long-lived knots, ≥ 10 min. But, the time scale for the density variations does turn out to be of the order of minutes, Section

5.5. Hence, we find that even though the Hα bright knots are a result of the thermal instability of coronal plasma, they are not a direct manifestation of this process. Instead, the knots are mainly due to the compression of loop plasma by velocities generated during the non-uniform cooling. As a result, their size scale is not set by the wavelength of the initial perturbation, which is of the order of the length of the loop, but is determined by the details of the plasma dynamics.

The results described in this section are relatively insensitive to the particular parameters of a loop. The main criterion that must be satisfied by a specific perturbation in order for it to develop into an observable knot is that its amplitude at the onset of instability be $\gtrsim 5\%$. The importance of the plasma dynamics follows from the fact that the cooling time is much less than the speed of sound travel time across the loop at low temperatures. For the plasma in a condensation to be compressed significantly, the velocity generated by the cooling must be supersonic. If it is subsonic then, of course, the plasma streaming energy is less than the thermal energy; hence large pressure (density) enhancements will not form.

We can estimate the dependence of the velocities on the density and wavelength of the initial perturbation. The velocity generated by pressure gradients of order p/λ, acting on a time scale, $p/n^2\Lambda$, is:

$$v \approx \frac{p^2}{m_H n^3 \Lambda \lambda} \quad . \tag{5.50}$$

Letting T_c be the temperature at instability onset, equations (5.50) and (5.9) yield

$$v \propto (n\lambda)^{1/7} \Lambda^{-3/7} \quad . \tag{5.51}$$

In the temperature range of interest, $T \sim 10^6$ K, we can approximate, $\Lambda \propto T^{-1}$, hence,

$$v \propto (n\lambda)^{1/3} \quad . \tag{5.52}$$

Equation (5.52) implies that the velocity generated by the non-uniform cooling and, therefore, the formation of a condensation is only weakly dependent on n or λ. Our computer calculations confirm this result.

5.4.4 Effect of Perturbation Amplitude

In agreement with the analytic model, we find that the evolution of the loop plasma is strongly dependent on the amplitude of the thermal perturbation at the onset of instability, T_c. If the amplitude is too small, then large temperature differences do not last for a long enough time to produce significant density variations.

This is illustrated by Figures 5.10 and 5.11 in which are plotted the temperature and density profiles of a loop with the same parameters as the ones used in the previous section, except that the initial amplitude has been halved to 2.5%. Large temperature differences occur in this case as well; at t = 510 sec, the loop top is at 3×10^4 K while the sides are at 10^6 K. However, the temperature variations last for less than 40 sec. By t = 550 sec, the temperature throughout the loop is at 3×10^4 K.

Comparing Figures 5.8 and 5.10, we note that similar temperature profiles occur in the loop with the 5% amplitude and in that with the 2.5% amplitude. But the density profiles at the time when all the

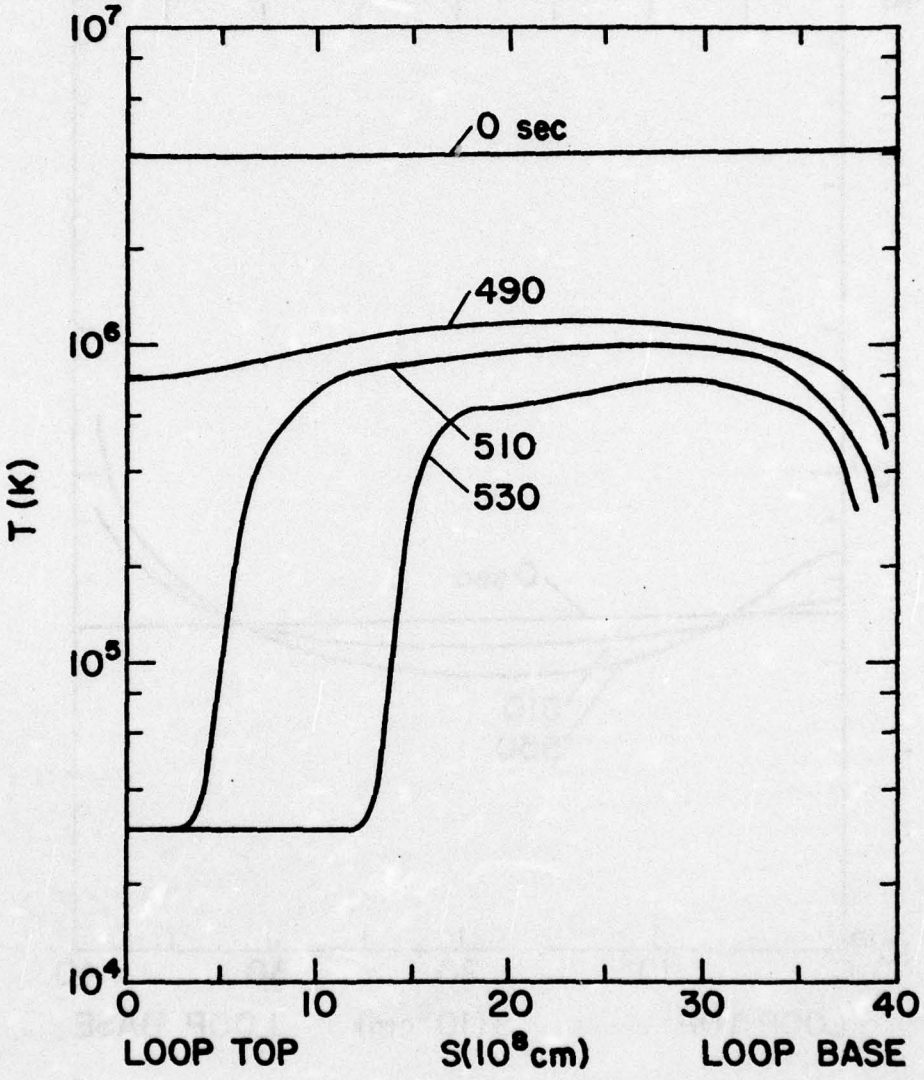

Figure 5.10 TEMPERATURE PROFILE OF A "STABLE" LOOP AT VARIOUS TIMES IN ITS EVOLUTION.

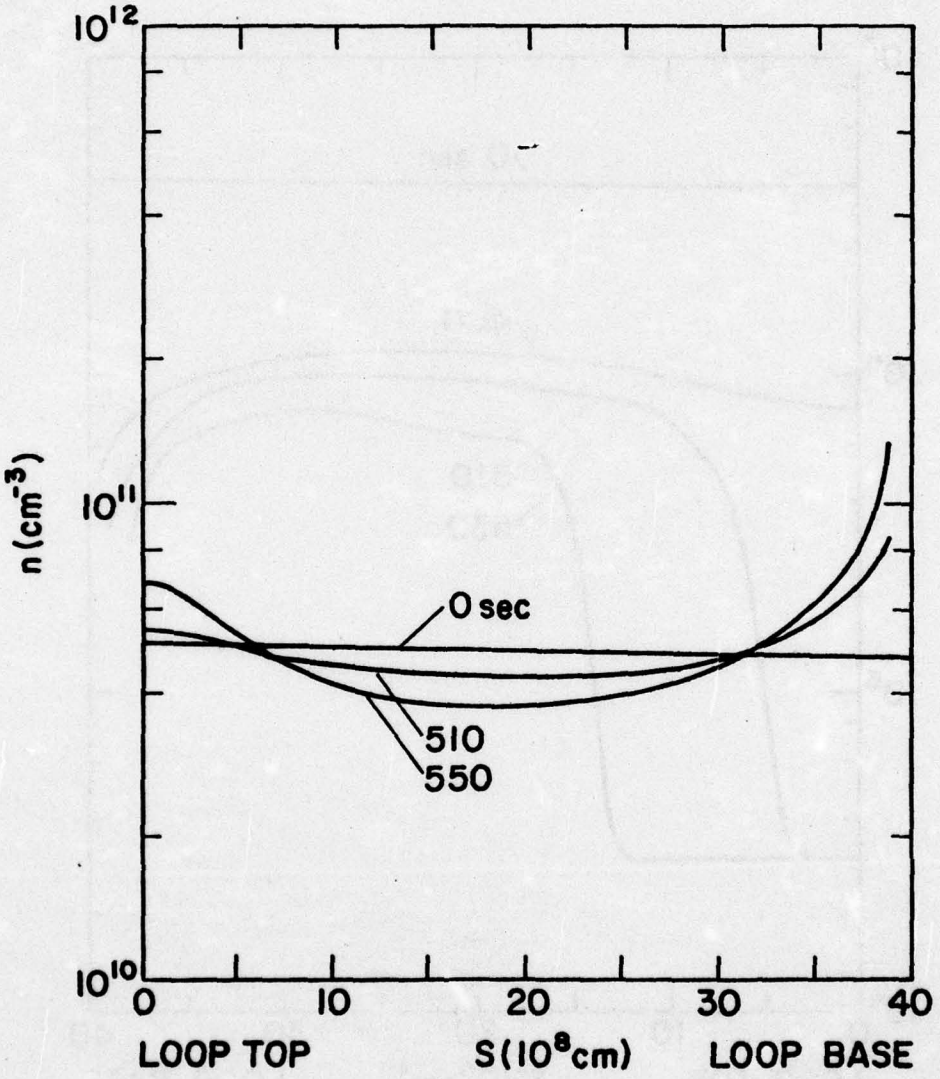

Figure 5.11 DENSITY PROFILE OF A "STABLE" LOOP AT VARIOUS TIMES IN ITS EVOLUTION.

plasma in each loop reaches 3×10^4 K are very different. Comparing Figure 5.9 and 5.11, we note that the density profile, for the loop with the 2.5% perturbation amplitude, at t = 550 sec is much smoother than the profile at the corresponding time, t = 570 sec, in the case of the 5% amplitude. For the loop with the smaller amplitude, the density at the top is less than twice that at the sides and the compressed region is of much larger size scale. This loop would not appear to have a very bright, compact knot in Hα; it would appear to be of approximately uniform brightness instead. It would correspond to a loop prominence event that does not begin as a bright knot.

For initial amplitudes larger than 5%, the evolution of the loop does not change qualitatively from the 5% case. The knot appears brighter, smaller and lasts longer, but the overall behavior is the same. For example, assuming a perturbation amplitude at instability onset of 10% in a loop with the same parameters as before, results in relatively larger density ratios between the compressed region and the sides, ($\gtrsim$ 50 instead of 10). In this case the temperature variations last for 180 sec, which is a significant fraction of the lifetime of knots.

The maximum velocities in the 10% case occur at the condensation boundary as in the previous cases. They attain a value of -1.4×10^7 cm/sec, implying a Mach number of M = 4. For the case of a 5% amplitude, we obtained M = 2, and for the 2.5% case, the maximum velocity is 3.2×10^6 cm/sec, i.e. M $\approx$ 1. Hence, the velocity is approximately proportional to the perturbation amplitude (for small amplitudes) as expected from the analytic model, equation (5.48).

5.5 Post-Cooling Stage

We define the third stage of the evolution of a post-flare loop to be that phase during which the temperature remains approximately constant at 3×10^4 K, Section 5.1. This evolution is, of course, determined by the pressure and velocity profiles that are present at the end of the radiative cooling stage and by gravity. We find that there are two possible general forms that the third stage evolution can take, depending on whether thermal instabilities have occurred.

If the loop is stable, i.e. no condensations form, then as noted in the previous section the density profile is approximately uniform at the time that the cooling ends. In addition, the velocities generated by the cooling process are small, $\ll c$. Hence, the subsequent behavior of the plasma is dominated by gravity. Since the gravitational scale height, $\frac{kT}{m_H g_\odot}$, at chromospheric temperatures is much less than the size of typical loops, the loop plasma begins to fall freely. The exact motion is complicated due to the variation of the gravitational force along the length of the loop; however, as one would expect, we find that the maximum velocities occur at the base of the loop. They are of the order of the free-fall velocity, and the time scale for their growth is of the order of the free-fall time. For a loop of height, $H = 3 \times 10^9$ cm, the free-fall velocity is $v_f = \sqrt{2 g_\odot H} = 10^7$ cm/sec, and the free-fall time is $H/v_f \approx 300$ sec.

If, on the other hand, the loop is unstable and a condensation forms, then we find that large pressure gradients are created which have an important effect on the velocity profile. Supersonic velocities form near the top of the loop well before gravitational effects become

significant, and at heights where the free-fall velocity is small. They are a result of the rapid expansion of the compressed region. In this section we describe in detail the post-cooling evolution of the unstable loop discussed in Section 5.4.3 and compare it with the evolution of a stable loop.

The radiative cooling stage ends at t = 570 sec for the unstable loop with the 5% perturbation amplitude, Section 5.4.3. The density profile at this time is shown in Figure 5.9 and the velocity profile in Figure 5.12. The velocities are residual from the non-uniform cooling stage; hence, within 25,000 km of the top they are directed up the loop. Near the base they are directed downward due to material having condensed onto the chromosphere. The velocity profile indicates that the condensation continues to be compressed (and brighten in Hα) for some time after the cooling ends.

Figure 5.9 implies the existence of large pressure gradients which act to reverse the upward velocities. Since the temperature is uniform, the pressure profile is, of course, directly proportional to the density. The time required to reverse the velocity is of order

$$\tau = \frac{\rho v \lambda}{p} \quad , \tag{5.53}$$

where λ is the width of the compressed region, $\leq 10^8$ cm in our case. From Figure 5.12, the upward velocity is approximately - 6×10^6 cm/sec; hence, $M \approx 2$ and equation (5.53) yields, $\tau = 60$ sec. This time is shorter than the time scale over which gravity is effective.

In agreement with this estimate for τ, we find that the velocities reverse direction at t = 620 sec (50 sec after the cooling ends). The

AD-A035 775 STANFORD UNIV CALIF INST FOR PLASMA RESEARCH F/G 3/2
THERMAL INSTABILITY IN POST-FLARE PLASMAS.(U)
DEC 76 S K ANTIOCHOS N00014-75-C-0673
UNCLASSIFIED SU-IPR-679 NL

2 OF 2
AD A035775

END

DATE FILMED
3-77

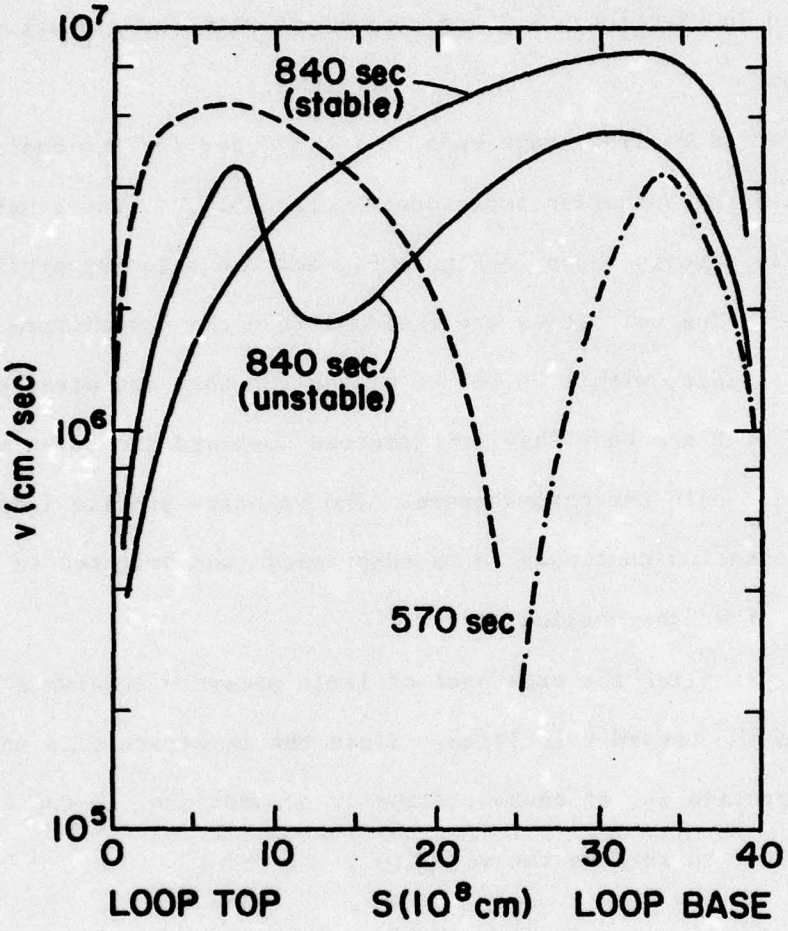

Figure 5.12 VELOCITY PROFILES OF A "STABLE" AND AN "UNSTABLE" LOOP AT VARIOUS TIMES IN THEIR EVOLUTION. The broken lines refer to the velocity profile of the unstable loop at the onset of the post-cooling stage, t = 570 sec. The broken line with no dots indicates negative velocities, directed up the loop, the line with dots indicates positive velocities, directed down the loop.

compression reaches its maximum density, 6×10^{11} cm^{-3}, and its minimum width, $\leq 5 \times 10^{7}$ cm, at this time, Figure 5.13. We note that the minimum density in the loop is approximately 2×10^{10} cm^{-3} at a position 1.3×10^{9} cm from the top. Therefore, the brightness in Hα of the compressed region should be almost 3 orders of magnitude larger than that of the sides of the loop; however, since the condensation is optically thick in Hα, radiative transfer effects limit its brightness.

We also plot the density profile at t = 620 sec as a function of Lagrangean coordinate, x, Figure 5.14. Note that this profile is much smoother than the corresponding one in Figure 5.13 – the compressed region is clearly visible and is of almost uniform density. Over 30% of the loop plasma is in the condensation; however, it occupies less than 10^{-2} of the loop volume. Figures 5.13 and 5.14 clearly illustrate the necessity of using Lagrangean coordinates for our computer calculations. If we were to attempt to follow the density in Eulerian coordinates, we would need a grid spacing finer than 10^{7} cm, which implies using almost 10^{3} points over the length of the loop. In fact, we only use 64 points with the Lagrangean grid.

The density profiles of the loop at t = 620, 720, 840 and 960 sec are plotted in Figure 5.13. The rapid expansion of the condensation can clearly be seen; the velocity of the condensation boundary is approximately 5×10^{6} cm/sec which is supersonic.

We plot the velocity profile at t = 840 in Figure 5.12 and, for comparison, we also plot the profile at t = 840 sec for a loop with the same geometry but with no initial perturbation, i.e. a completely stable loop. Below 10^{9} cm from the top, the velocities in the stable

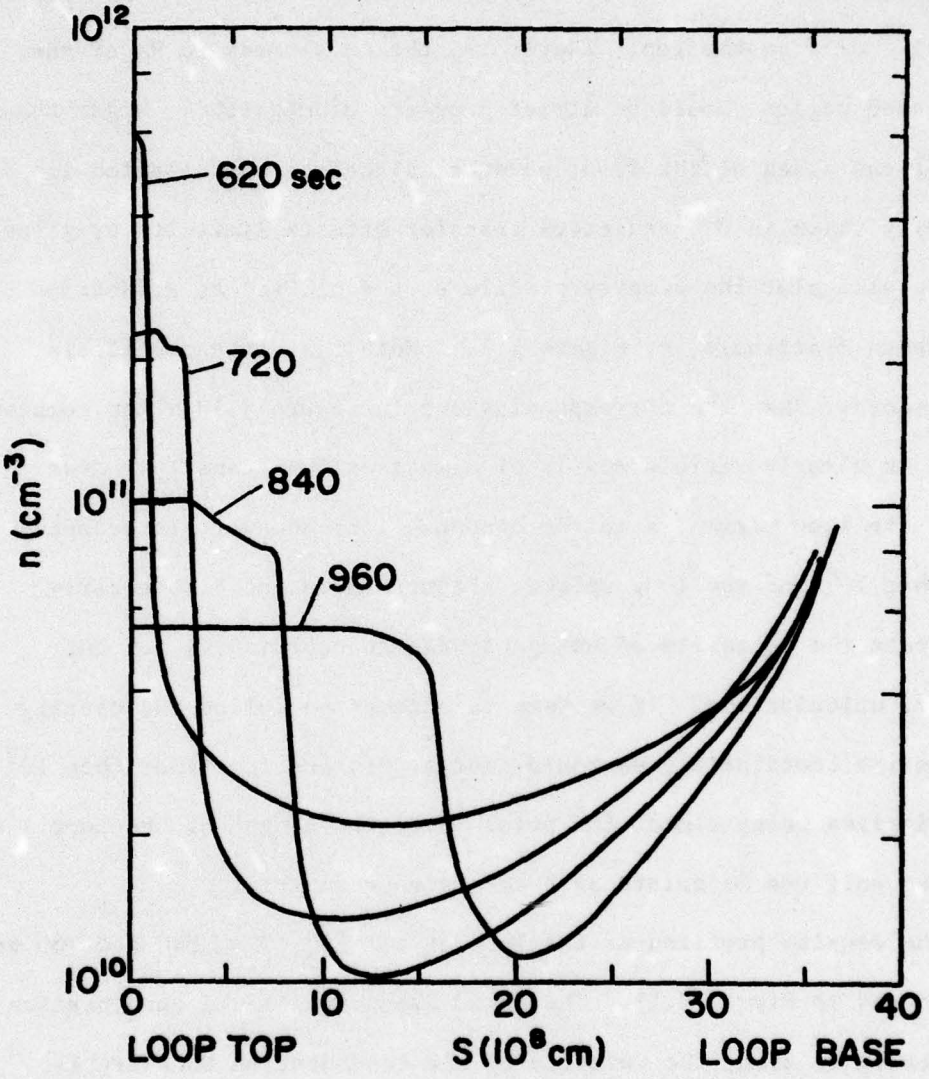

Figure 5.13 DENSITY PROFILE OF AN "UNSTABLE" LOOP AT VARIOUS TIMES IN THE POST-COOLING PHASE OF ITS EVOLUTION.

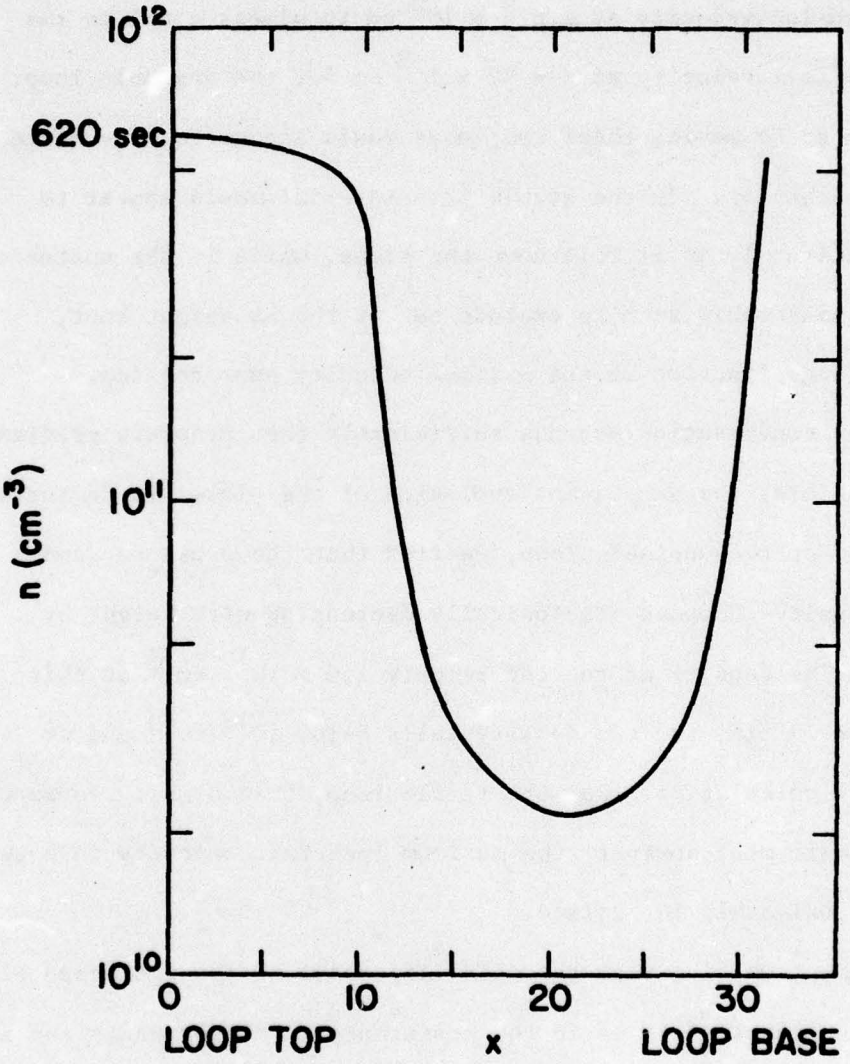

Figure 5.14 DENSITY IN AN "UNSTABLE" LOOP AS A FUNCTION OF LAGRANGEAN COORDINATE, x, AT THE TIME WHEN THE CONDENSATION DENSITY IS MAXIMUM.

loop are larger than the ones in the unstable case. This is because no upward velocities are generated during the radiative cooling stage in the stable case. On the other hand, within 10^9 cm of the top, the velocities in the unstable loop are higher due to the expansion. The maximum expansion velocity at $s = 8 \times 10^8$ cm is almost equal to the maximum free-fall velocity at $s = 32 \times 10^8$ cm for the unstable loop. If viewed in an Hα movie, these two loops would appear to have quite a different behavior. In the stable loop material would appear to accelerate uniformly as it fell down the sides, while in the unstable loop, the plasma would seem to explode out of the Hα bright knot, reaching a large fraction of its maximum velocity near the top.

Once the condensation expands sufficiently that pressure gradients become negligible, the subsequent evolution of the plasma is dominated by gravity. For the unstable loop, we find that the pressure (and hence the density) becomes monotonically decreasing with height by $t = 20$ min. The density at the top is only 1.9×10^{10} cm^{-3} at this time. By $t = 23$ min, the top density falls below 10^{10} cm^{-3} and we terminate our calculation. For the stable loop, this density is reached sooner at $t = 18$ min; however, the maximum free-fall velocity in both cases is approximately 10^7 cm/sec.

In summary, we find that the main difference in the evolution of a stable and unstable loop is in the appearance of bright knots and in the acceleration of cold plasma near the top. Since we somewhat arbitrarily fixed the temperature at 3×10^4 K, the details of our results on the post-cooling phase of flare loops may be inaccurate, but we believe that the important features are correct. We compare these features with observations in the following section.

6. DISCUSSION

6.1 Comparison with Observations

If we compare the results in the previous chapter on the evolution of an unstable loop with the description of loop prominences given in chapter 2, we note that they are in good agreement. For the case of the loop with a 5% initial perturbation amplitude, the average density in the condensation during its lifetime is $\geq 10^{11}$ cm^{-3}, and its size is small compared to the size of the loop, $\leq 5 \times 10^{8}$ cm. In Hα it would appear as a bright knot. The plasma velocities near the condensation are large; there is a shock at the boundary during its formation and a large expansion velocity during its decay. This agrees with Jefferies and Orrall's (1965a) observation of large streaming velocities at the top of active loop prominences. Defining the lifetime of a knot as the time interval from the instant it first appears in Hα to when it expands to a size of half the loop length; we find that the lifetime in our case is approximately 8 minutes. Bruzek and Kuperus (1972) quote the lifetime of a knot as 3 - 10 minutes.

The maximum velocity that we obtain at the loop base, 115 km/sec, equals the free-fall velocity. The average velocity is slightly lower, $\leq$ 100 km/sec, in agreement with observations. There is a shock at the base where the falling matter impacts with the chromosphere; however, the radiative losses are sufficient to dissipate the mechanical energy flux. In an unstable loop, large velocities appear near the top (at the knot boundary) due to pressure gradients; whereas, in a stable loop material accelerates uniformly down the sides. We calculate the total lifetime of a loop event as approximately 30 minutes. Bruzek (1964a)

gives the observed lifetime of typical loops as 30 - 60 minutes. Of course, these time scales and velocities will vary depending on the size and density of a loop, equations (5.2) and (5.3). For lower densities and larger loop heights, the radiative cooling time and the free-fall time increase. However, the long lifetime of loop prominence systems, $\leq 10^5$ sec, does not appear to be due to a cooling effect. Even if all conductive losses are suppressed by a large magnetic field compression factor Γ, the radiative losses alone for densities of $\sim 10^{10}$ cm^{-3} and temperatures of $\sim 10^7$ K imply a cooling time of only 10^3 sec. Hence, the long lifetime of a loop system is most likely due to a long-lived flare heating process.

In general we find that the temperature, densities and velocities measured in a loop prominence are accurately reproduced by our model. From this, we conclude that the thermal instability mechanism by itself is sufficient to account for a loop prominence event. The appearance of knots and their subsequent evolution can be understood as being due to the temperature and density dependence of the cooling function (Figure 1.1) for the coronal plasma. Our only important assumption is the form of the temperature and density profiles during the radiative cooling stage. If a perturbation of small but finite amplitude is present a condensation will form. If, on the other hand, the profiles are uniform as we would expect from the discussion in Section 5.2.1, then no knots appear and the evolution of the loop plasma will more closely resemble that of coronal rain.

We have given no justification for choosing the particular form of the perturbation in equation (5.49), except that it is the one with

the largest wavelength and, hence, the fastest growth rate. In accordance with observations, condensations may form at the sides of loops if the perturbation profiles are suitably chosen; however, these knots are not as dense or as long-lived as those centered at the top. Unfortunately, the observations are not accurate enough to determine the temperature and density profiles of a loop to within 5%; hence we cannot directly check our assumption. The soft x-ray emission is observed to be greater at the tops of loops (Cheng and Widing, 1975; Pallavacini et al., 1975), but that would be expected due to the area factor even if the temperature were slightly lower there.

There is reason to expect that the temperature will be higher at the sides of a flare loop if the heating is due to high energy electrons as in the models proposed by Sturrock (1968), Petrosian (1973) and others (Svestka, 1976, Section 3.2). In these models the bulk of the flare energy is carried down the field lines by non-thermal electrons and deposited in the chromosphere or lower corona. Hence, the temperature should initially be higher near the base of a loop. If the electrons have non-zero pitch angles and are trapped in the flux tube, then again, we would expect higher temperatures at the sides of a loop. The electrons spend more time near their mirror points than near the top of a loop, since their velocity parallel to the field is highest at the top. This process also has the attraction that if a loop is symmetrical about the top, then the heating due to trapped energetic electrons will have the same symmetry; hence any temperature perturbation will be symmetrical about the top in agreement with our assumption in equation (5.49).

We intend to investigate these possibilities in detail by including a heating function in our code to represent flare heating. We also

intend to modify the boundary conditions to permit an upward mass flux at the base of the loop. This will allow us to study the evaporation of chromospheric material, and, perhaps, to determine the form of flare heating.

6.2 Conclusions

To summarize, we restate the main conclusions of our calculations here:

1. For typical post-flare loops, the conductive damping time at high temperature, $\geq 10^7$ K, is so short that all temperature and pressure gradients are damped quickly compared to the cooling time. Hence the analytic models proposed by Antiochos and Sturrock (1976a, b) adequately represent the initial cooling.

2. The inclusion of the area factor does not alter the linear growth rate of thermal perturbations, equation (1.14).

3. The effect of the nonlinearities is to increase the stability of the plasma, Figure 5.3.

4. Observable condensations will grow if criteria 1 - 4 in Section 5.3 are satisfied. The important requirement is that the perturbation amplitude at the onset of instability be $\geq 5\%$.

5. Shocks form at the boundary of knots during their compression phase. Large velocities are generated by their subsequent expansion.

6. The appearance of bright knots is mostly due to density variations along the loop, since temperature variations last for only a short time, ≤ 100 sec.

7. The evolution of loop prominences can be understood as simply due to thermal instability in chromospheric material that has been

evaporated into the corona by a flare. Mechanisms such as strong compression by magnetic fields or the migration of energetic protons across field lines are not required.

8. The radiative cooling time for temperatures and densities typical of post-flare loops is too short to account for the long lifetime of loop prominence systems; hence, a long-lived (time scales of the order of several hours), flare heating process is required.

APPENDIX A

FLUID EQUATIONS FOR A DIPOLE LOOP

We wish to derive the fluid equations for the case of a flux tube. Since we assume that the field dominates the plasma, we can most easily incorporate the effects of the field by letting the field lines define a curvilinear coordinate system. This is always possible if the field is potential (Morse and Feschback, 1953, p. 14).

Let (x^1, x^2, x^3) denote the coordinate system, where $x^1 = s$, the distance along the field. We are only interested in an individual loop whose cross-sectional area is very small compared to the radius of curvature of the field. Thus, we can approximate the metric in the loop by:

$$g_{ij} = \begin{pmatrix} 1 & 0 & 0 \\ 0 & A(x^1) & 0 \\ 0 & 0 & A(x^1) \end{pmatrix} \tag{A1}$$

To obtain the fluid equations in terms of our coordinate system, we first rewrite them in covariant form. They are:

$$\frac{\partial n}{\partial t} + (nv^i)_{\|i} = 0 \quad , \tag{A2}$$

$$\frac{\partial (nm_H v_i)}{\partial t} + (nm_H v_i v^i + p\delta_i^j + \Pi_i^j)_{\|j} = nm_H g_i \quad , \tag{A3}$$

$$\frac{\partial}{\partial t}\left(\frac{1}{2} nm_H v_i v^i + \frac{3}{2} p\right) + \left(\frac{1}{2} nm_H v_i v^i v^j + \frac{5}{2} pv^j + q^j + \Pi_i^j v^i\right)_{\|j} = nm_H g_i v^i + \mathcal{L} \tag{A4}$$

where we have used the form of the equations given by Braginskii (1965)

and the tensor notation of Adler, Bazin and Schiffer (1965), Chapter 2. Note that all spatial derivatives are covariant derivatives and that the Einstein convention of summing over repeated indices is used.

The equations A2 - A4 simplify considerably in our case since we have no variables dependent on x^2 or x^3 and all vectors have a component in the x^1 direction only. Hence,

$$v^i = \left(v\ (x^i),\ 0,\ 0\right) \quad . \tag{A5}$$

The heat flux q_i and the stress tensor Π_{ij} are given by Braginskii (1965);

$$q_i = -\kappa T_{\|i} = \left(-\kappa \frac{\partial T}{\partial x^i},\ 0,\ 0\right) \quad , \tag{A6}$$

and

$$\Pi_{ij} = \eta\left(v_{i\|j} + v_{j\|i} - \frac{2}{3} g_{ij} v^k_{\|k}\right) \quad , \tag{A7}$$

hence,

$$\Pi_{ij} = \eta \begin{pmatrix} 2\frac{\partial v}{\partial x^1} - \frac{2}{3}\frac{1}{A}\frac{\partial}{\partial x^1}(Av) & 0 & 0 \\ 0 & v\frac{dA}{dx^1} - \frac{2}{3}\frac{\partial}{\partial x^1}(Av) & 0 \\ 0 & 0 & v\frac{dA}{dx^1} - \frac{2}{3}\frac{\partial}{\partial x^1}(Av) \end{pmatrix} . \tag{A8}$$

Using equation (A5) and the metric (A1), the mass equation (A2) becomes:

$$\frac{\partial n}{\partial t} + \frac{1}{A}\frac{\partial (Anv)}{\partial s} = 0 \quad , \tag{A9}$$

where we have replaced x^1 by s. Using (A9) and (A8), the momentum equation (A3) becomes:

$$m_H n\left(\frac{\partial v}{\partial t} + v\frac{\partial v}{\partial s}\right) + \frac{\partial p}{\partial s} + \frac{1}{A}\frac{\partial}{\partial s}(A\eta w) - \frac{1}{3}\frac{\partial}{\partial s}(\eta w) = m_H n g_{\parallel} \quad , \tag{A10}$$

where

$$w = 2\frac{\partial v}{\partial s} - v\frac{\partial}{\partial s}\ell n\, A \quad , \tag{A11}$$

and we have replaced g_1 by $g_{\parallel}$.

Finally, using equations (A10), (A9) and (A6), the heat equation (A4) can be expressed as:

$$\frac{3}{2}\left(\frac{\partial p}{\partial t} + v\frac{\partial p}{\partial s}\right) + \frac{5}{2}\frac{p}{A}\frac{\partial}{\partial s}(Av) - \frac{1}{A}\frac{\partial}{\partial s}\left(\kappa\frac{\partial T}{\partial s}\right) + \frac{\eta w^2}{3} = \mathcal{L} \quad . \tag{A12}$$

Since η is small, we can neglect the viscosity terms to obtain the set of equations (3.20) - (3.22) in Section 3.6.

We now need to calculate A(s) and $g_{\parallel}(s)$ for a dipole field. Using the coordinates defined in Figure (3.1), a dipole field is given by (Jackson, 1962, p. 143),

$$\vec{B} \propto \frac{1}{r^3}\left(2\sin\theta\,\hat{\ell}_r - \cos\theta\,\hat{\ell}_\theta\right) \quad . \tag{A13}$$

The equation of a field line of height R is given by:

$$r/R = \cos^2\theta \quad . \tag{A14}$$

Letting

$$\nu \equiv \sin\theta \quad , \tag{A15}$$

the distance along the field line,

$$ds = \sqrt{(dr)^2 + r^2(d\theta)^2} \quad , \tag{A16}$$

becomes:

$$ds = R\sqrt{3\nu^2 + 1}\ d\nu \quad . \tag{A17}$$

Integrating (A17), we obtain equation (3.28). The area factor equation (3.29) can be obtained from equations (A13) and (A14) since we have

$$A \propto \frac{1}{|\vec{B}|} \quad . \tag{A18}$$

The component of gravity parallel to the field, equation (3.30), is given by

$$g_{\parallel} = - g_{\odot}\, \hat{\ell}_z \cdot \frac{\vec{B}}{|\vec{B}|} \quad , \tag{A19}$$

where $\hat{\ell}_z$ is a unit vector in the vertical direction,

$$\hat{\ell}_z = \cos\theta\, \hat{\ell}_r - \sin\theta\, \hat{\ell}_\theta \quad . \tag{A20}$$

In Figure A1, we plot $A(s)$ and $g_{\parallel}(s)$ for a dipole loop.

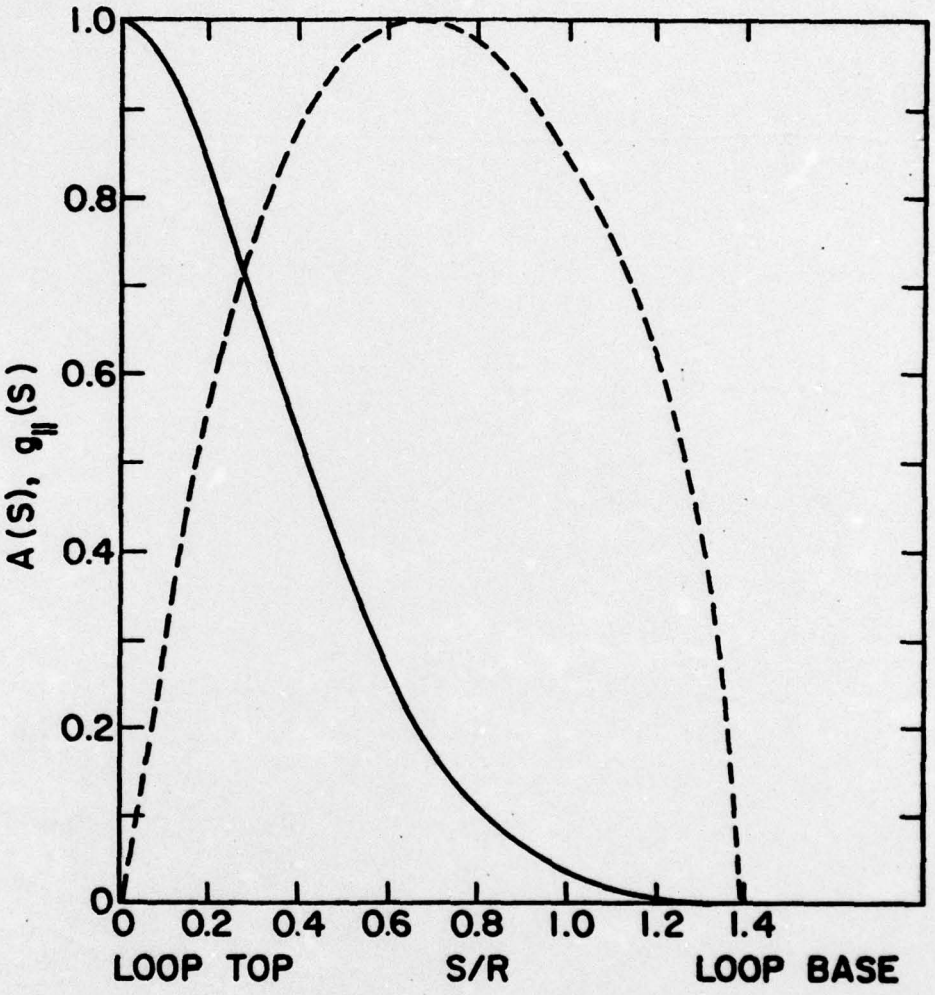

Figure A.1 PROFILES OF THE AREA OF A LOOP DUE TO A DIPOLE SOURCE AND OF THE COMPONENT OF GRAVITY PARALLEL TO THE LOOP. The solid line refers to A(S) and the broken line to $g_{\parallel}(S)$. Both A and $g_{\parallel}$ are normalized to equal unity at their respective maxima.

APPENDIX B

```
C B.1   FINITE DIFFERENCE EQUATIONS
C
C DETAILS OF DIFFERENCING SCHEME FOR EQUATIONS (4.3 - 4.7) WITH
C BOUNDARY CONDITIONS (4.18 - 4.19).  THE FOLLOWING IS THE CODE TO
C ADVANCE VALUES OF VARIABLES BY ONE TIME STEP, DT. THE VALUE OF DT
C FOR THE NEXT TIME STEP CAN BE EVALUATED USING CONDITION (4.40).
C THAT ROUTINE IS NOT INCLUDED HERE.  IN THE NEXT SECTION A ROUTINE
C FOR TABLE LOOK-UPS IS GIVEN.
C
C WE DIVIDE EACH LEG OF THE LOOP INTO 32 EQUAL MASS SLABS.  EACH SLAB
C IS OF WIDTH (MASS) DX.  WE CHOOSE THE POINT X = 0 TO BE THE TOP OF
C THE LOOP.
C
C LIST OF VARIABLES USED IN CODE:
C ALL ARRAYS HAVE 33 ELEMENTS.  (SOMETIMES NOT ALL ELEMENTS USED).
C        PRIMARY VARIABLES:
C VALUES OF PLASMA PARAMETERS AT TIME = T.  NEEDED AS INPUT TO ADVANCE
C TIME STEP.  MUST BE OUTPUTTED TO USE FOR THE NEXT STEP.
C "S(J)" = EULERIAN POSITION OF LAGRANGEAN POINT (J-1)*DX
C "V(J)" = VELOCITY AT LAGRANGEAN POINT (J-1)*DX.
C "T(J)" = TEMPERATURE AT LAGRANGEAN POINT (J-1/2)*DX.
C (NOTE THAT WE POSITION SOME VARIABLES DIFFERENTLY FOR PROPER
C CENTERING OF DIFFERENCE EQUATIONS.)
C "P(J)" = PRESSURE AT LAGRANGEAN POINT (J-1/2)*DX.
C "AN(J)" = NUMBER DENSITY AT LAGRANGEAN POINT (J-1/2)*DX.
C "Q(J)" = ARTIFICIAL VISCOSITY AT LAGRANGEAN POINT (J-1/2)*DX.
C
C       PROVISIONAL VARIABLES:
C VALUES OF PLASMA PARAMETERS AT TIME = T + DT/2.  THE SPATIAL
C POSITIONING IS SAME AS ABLVE.
C "S1(J)", "V1(J)", "T1(J)", "P1(J)", "AN1(J)", "Q1(J)"
C
C       SECONDARY VARIABLES:
C VALUES OF SECONDARY PARAMETERS AT EITHER TIME = T OR T + DT/2.
C MAY BE OUTPUTTED IF DESIRED.
C "VDER(J)" = D(V(J))/DT.
C "TDER(J)" = D(T(J))/DT.
C "AS(J)" = AREA FACTOR AT LAGRANGEAN POINT (J-1)*DX.
C "GS(J)" = COMPONENT OF GRAVITY PARALLEL TO
C           LOOP AT LAGRANGEAN POINT (J-1)*DX.
C "T12(J)" = SQUARE ROOT OF T(J).
C "T72(J)" = T(J) RAISED TO THE POWER OF 7/2.
C "ALT(J)" = COX AND TUCKER RADIATIVE LOSSES AT TEMPERATURE T(J).
C "HFLX(J)" = HEAT FLUX AT LAGRANGEAN POINT (J-1)*DX.
C
C ARRAYS USED FOR STORAGE ONLY: "V12(J)", "AV(J)", "D(J)".
C
C CONSTANTS:  CHOSEN TO MAKE VARIABLES DIMENSIONLESS.
C "DX" = 2/3,   "EQV1", "QOPO", "EQT3", "EQT32".
C "AIB" = VOLUME OF LEG OF LOOP.
C "DT" = TIME INCREMENT, CONSTANT ONLY FOR EACH TIME ADVANCE.
C "DT2" = DT/2, "DT3" = DT/3, "DT4" = DT/4.
```

```
C VARIABLES USED FOR STORAGE ONLY: "AIL, AIF, DELTV".
C
C BOUNDARY CONDITIONS: VALUES CONSTANT FOR ALL TIME
C  S(1), V(1)  HFLX(1), S(33), V(33), T(33).
C ***************************************************************************
C ROUTINE TO INCREMENT TIME BY DT/2.
C CALCULATE PROVISIONAL VARIABLES: V1(2), S1(2), AN1(1), Q1(1)
      VDER(2) = EQV1*AS(2)*(P(2) + Q(2) - P(1) - Q(1)) + GS(2)
      V1(2) = V(2) + DT2*VDER(2)
      V12(2) = V1(2) + V(2)
      S1(2) = S(2) + DT4*V12(2)
C---INSERT ROUTINE TO CALCULATE AS(2), GS(2), AIL - SEE SECTION B.2
C AIL = VOLUME OF LOOP FROM TOP TO POINT S1(2)
 310  AN1(1) = DX/(AIL)
      AV(2) = AS(2)*V1(2)
      DELTV = V1(2) - V1(1)
      IF(DELTV)330, 320, 320
 320  Q1(1) = 0.
      GO TO 340
 330  Q1(1) = QOPO*AN1(1)*DELTV*DELTV
 340  CONTINUE
C START MAIN DO LOOP 1111111111111111111111111111111111111
      DO 460 J = 1, 30
C CALCULATE V1(J+2), S1(J+2), AN1(J+1), Q1(J+1)
      VDER(J+2) = EQV1*AS(J+2)*(P(J+2) + Q(J+2) - P(J+1) - Q(J+1))
     1 + GS(J+2)
      V1(J+2) = V(J+2) + DT2*VDER(J+2)
      V12(J+2) = V1(J+2) + V(J+2)
      S1(J+2) = S(J+2) + DT4*V12(J+2)
C---INSERT ROUTINE TO CALCULATE AS(J+2), GS(J+2), AIF - SEE SECTION B.2
C AIF = VOLUME OF LOOP FROM TOP TO POINT S1(J+2)
 370  AN1(J+1) = DX/(AIF-AIL)
      AIL = AIF
      AV(J+2) = AS(J+2)*V1(J+2)
      DELTV = V1(J+2) - V1(J+1)
      IF(DELTV) 390, 380, 380
 380  Q1(J+1) = 0.
      GO TO 400
 390  A1(J+1) = QOPO*AN1(J+1)*DELTV*DELTV
 400  CONTINUE
C CALCULATE T1(J), P1(J)
      D(J+1) = AS(J+1)*AS(J+1)*AN1(J)*AN1(J+1)/(AN1(J) + AN1(J+1))
      HFLX(J+1) = D(J+1)*(T72(J+1) - T72(J))
      TDER(J) = (P(J) + Q1(J))*(AV(J) - AV(J+1)) + AN1(J)*ALT(J)
     1 + EQT3*(HFLX(J+1) - HFLX(J))
      T1(J) = T(J) + DT2*TDER(J)
      IF(T1(J)  .LT.  T(33))GO TO 440
C---INSERT ROUTINE TO CALCULATE T12(J), T72(J), ALT(J) - SEE SECTION B.2
      GO TO 450
 440  T1(J) = T(33)
      ALT(J) = ALT(33)
      T72(J) = T72(33)
 450  P1(J) = AN1(J)*(T1(J))
 460   CONTINUE
C END OF MAIN DO LOOP 1111111111111111111111111111111111111
```

```
C CALCULATE AN1(32), Q1(32)
      AN1(32) = DX/(AIB-AIL)
      DELTV = V1(33) - V1(32)
      IF(DELTV) 480, 470, 470
 470  Q1(32) = 0.
      GO TO 490
 480  Q1(32) = QOPO*AN1(32)*DELTV*DELTV
 490  CONTINUE
C CALCULATE T1(31), P1(31)
      D(32) = AS(32)*AS(32)*AN1(31)*AN1(32)/(AN1(32) +AN1(31))
      HFLX(32) = D(32)*(T72(32) - T72(31))
      TDER(31) = (P(31) + Q1(31))*(AV(31) - AV(32)) + AN1(31)*ALT(31)
     1 + EQT3*(HFLX(32) - HFLX(31))
      T1(31) = T(31) + DT2*TDER(31)
      IF(T1(31) .LT. T(33))GO TO 530
C---INSERT ROUTINE TO CALCULATE T12(31), T72(31), ALT(31) - SEE SECTION B.2
      GO TO 540
 530  T1(31) = T(33)
      ALT(31) = ALT(33)
      T72(31) = T72(33)
 540  P1(31) = AN1(31)*(T1(31))
C CALCULATE T1(32), P1(32)
      HFLX(33) = AS(33)*(T72(33) - T72(32))/(S(33) - S1(32))
      TDER(32) = (P(32) + Q1(32))*AV(32) + AN1(32)*ALT(32)
     1 + EQT32*HFLX(33) - EQT3*HFLX(32)
      T1(32) = T(32) + DT2*TDER(32)
     IF(T1(32) .LT. T(33)) GO TO 580
C---INSERT ROUTINE TO CALCULATE T12(32), T72(32), ALT(32) - SEE SECTION B.2
      GO TO 590
 580  T1(32) = T(33)
      ALT(32) = ALT(33)
      T72(32) = T72(33)
 590  P1(32) = AN1(32)*(T1(32))
C ***************************************************************************
C END OF TIME INCREMENT BY DT/2.  BEGIN INCREMENT BY DT.
C CALCULATE PROVISIONAL VARIABLES: V(2), S(2), AN(1), Q(1)
      VDER(2) = EQV1*AS(2)*(P1(2) + Q1(2) - P1(1) - Q1(1)) + GS(2)
      V(2) = V(2) + DT*VDER(2)
      S(2) = S(2) + (V12(2) + V(2))*DT3
C---INSERT ROUTINE TO CALCULATE AS(2), GS(2),AIL - SEE SECTION B.2
C AIL = VOLUME OF LOOP FROM TOP TO POINT S(2)
 620  AN(1) = DX/(AIL)
      DELTV = V(2) - V(1)
      IF(DELTV)640, 630,630
 630  Q(1) = 0.
      GO TO 650
 640  Q(1) = QOPO*AN(1)*DELTV*DELTV
 650  CONTINUE
C START OF MAIN DO LOOP 22222222222222222222222222222222222
      DO 770 J=1, 30
      VDER(J+2) = EQV1*AS(J+2)*(P1(J+2) + Q1(J+2) - P1(J+1) - Q1(J+1))
     1 + GS(J+2)
      V(J+2) = V(J+2) + DT*VDER(J+2)
      S(J+2) = S(J+2) + (V12(J+2) + V(J+2))*DT3
C---INSERT ROUTINE TO CALCULATE AS(J+2), GS(J+2), AIF - SEE SECTION B.2
C AIF = VOLUME OF LOOP FROM TOP TO POINT S(J+2)
```

```
  680  AN(J+1) = DX/(AIF-AIL)
       AIL = AIF
       DELTV = V(J+2) - V(J+1)
       IF(DELTV)700, 690, 690
  690  Q(J+1) = 0.
       GO TO 710
  700  Q(J+1) = QOPO*AN(J+1)*DELTV*DELTV
  710  CONTINUE
C CALCULATE T(J), P(J)
       HFLX(J+1) = D(J+1)*(T72(J+1) - T72(J))
       TDER(J) = (P1(J) + Q1(J))*(AV(J) - AV(J+1)) + AN1(J)*ALT(J)
      1 + EQT3*(HFLX(J+1) - HFLX(J))
       T(J) = T(J) + DT*TDER(J)
       IF(T(J) .LT. T(33))GO TO 750
C---INSERT ROUTINE TO CALCULATE T12(J), T72(J), ALT(J) - SEE SECTION B.2
       GO TO 760
  750  T(J) = T(33)
       T12(J) = T12(33)
       T72(J) = T72(33)
  760  P(J) = AN(J)*(T(J))
  770  CONTINUE
C END OF MAIN DO LOOP 22222222222222222222222222222222222222222
C CALCULATE AN(32), Q(32)
       AN(32) = DX/(AIB-AIL)
C CALCULATE T(31), P(31)
       DELTV = V(33) - V(32)
       IF(DELTV)790,780,780
  780  Q(32) = 0
       GO TO 800
  790  Q(32) = QOPO*AN(32)*DELTV*DELTV
  800  CONTINUE
       HFLX(32) = D(32)*(T72(32) - T72(31))
       TDER(31) = (P1(31) + Q1(31))*(AV(31) - AV(32)) + AN1(31)*ALT(31)
      1 + EQT3*(HFLX(32) - HFLX(31))
       T(31) = T(31) + DT*TDER(31)
       IF(T(31) .LT. T(33))GO TO 840
C---INSERT ROUTINE TO CALCULATE T12(31), T72(31), ALT(31) - SEE SECTION B.2
       GO TO 850
  840  T(31) = T(33)
       ALT(31) = ALT(33)
       T12(31) = T12(33)
       T72(31) = T72(33)
  850  P(31) = AN(31)*(T(31))
C CALCULATE T(32), P(32)
  855  HFLX(33) = AS(33)*(T72(33) - T72(32))/(S(33) - S1(32))
       TDER(32) = (P1(32) + Q1(32))*AV(32) + AN1(32)*ALT(32)
      1 + EQT32*HFLX(33) - EQT3*HFLX(32)
       T(32) = T(32) + DT*TDER(32)
       IF(T(32) .LT. T(33))GO TO 890
C---INSERT ROUTINE TO CALCULATE T12(32), T72(32), ALT(32) - SEE SECTION B.2
       GO TO 900
  890  T(32) = T(33)
       ALT(32) = ALT(33)
       T12(32) = T12(33)
       T72(32) = T72(33)
  900  P(32) = AN(32)*(T(32))
C END OF ROUTINE
C ALL PRIMARY VARIABLES HAVE BEEN INCREMENTED BY DT.
C ***************************************************************************
```

```
C B.2   ROUTINE FOR TABLE LOOK-UPS
C
C AS DISCUSSED IN SECTION 4.4 WE MUST EVALUATE 3 FUNCTIONS OF EULERIAN
C POSITION S(J); AS(J), GS(J), AND AIF (OR AIL), AND 2 OF TEMPERATURE
C T(J): T12(J) AND ALT(J).  WE FIRST TABULATE THESE 5 FUNCTIONS AT 240
C LINEARLY SPACED VALUES IN EACH OF THE FOUR INTERVALS:
C S(J) OR T(J) = 1/4096 - 1/256, 1/256 - 1/16,1/16 - 1, AND 1 - 16,
C AND THEN USE LINEAR INTERPOLATION TO FIND THE VALUE OF A FUNCTION FOR
C A PARTICULAR S(J) OR T(J).  BY SUITABLY NORMALIZING S(J) AND T(J) WE
C CAN USE THE FIRST 2 BYTES OF S(J) OR T(J) TO LOCATE THE NEAREST ENTRY IN
C THE TABLE.  FOR EXAMPLE, WE LIST BELOW THE ROUTINE FOR FINDING ALT(J)
C AND T12(J).  IN THIS ROUTINE THE TABLES ARE IN ARRAYS AL AND TSQ, THE
C POSITION OF THE NEAREST ENTRY IS EITHER "NST" OR "NST+1".
C
      REAL*4 TCH, STREF, TABSEP
      LOGICAL*1 QQ,QL(4)
      INTEGER*4 NFSET
      INTEGER*2 NN,MM
      EQUIVALENCE (TCH, NN, QQ), (TABSEP, QL(1)), (MM,STREF)
      DATA NFSET/Z00003E0F/, TABSEP/Z00010000/,
     1STREF/Z00000000/
C---ROUTINE TO CALCULATE T12(J), T72(J), ALT(J)
C FIRST WE FIND "NST", THE POSITION OF THE ENTRY NEAREST
C TO T(J) AND LESS THAN T(J).
      TCH = T(J)
      NST = NN - NFSET
C NOW WE FIND THE SEPARATION BETWEEN T(J) AND THE POSITION "NST".
      QL(1) = QQ
      MM = NN
      DIFST = TCH-STREF
C NOW DECIDE WHETHER "NST" OR "NST+1" IS CLOSER TO T(J).
C FOR EXTRA ACCURACY WE USE SECOND ORDER INTERPOLATION FOR T12(J).
      IF(DIFST+DIFST-TABSEP)720,720,730
 720  ALT(J) = AL(NST) + DIFST*(AL(NST+1) - AL(NST))/TABSEP
      TRATO = DIFST/(STREF+STREF)
      T12(J) = TSQ(NST)*(1.+TRATO*(1.-.5*TRATO))
      GO TO 740
 730  DIFST = DIFST-TABSEP
      ALT(J) = AL(NST+1) + DIFST*(AL(NST+1) - AL(NST))/TABSEP
      TRATO = DIFST/(STREF+STREF+TABSEP+TABSEP)
      T12(J) = TSQ(NST+1)*(1.+TRATO*(1.-.5*TRATO))
 740  T72(J) = TCH*TCH*TCH*(T12(J)
C--END OF ROUTINE
```

REFERENCES

Adler, R., Bazin, M. and Schiffer, M. 1965, Introduction to General Relativity (New York: McGraw-Hill).

Antiochos, S.K. and Sturrock, P.A. 1976a, Sol. Phys. (in press).

_____. 1976b, SUIPR No. 676, Submitted to Ap. J.

Braginskii, S.K. 1965, Rev. of Plasma Physics, 1, 205.

Bruzek, A. 1964a, Ap. J., 140, 746.

_____. 1964b, J. Geophys. Res., 69, 2386.

Bruzek, A. and Kuperus, M. 1972, Sol. Phys., 24, 3.

Cheng, C.C. and Widing, K.G. 1975, Ap. J., 201, 735.

Cox, D.P. and Daltabuit, E. 1971, Ap. J., 167, 113.

Cox, D.P. and Tucker, W.H. 1969, Ap. J., 157, 1157.

Craig, I.J.D. and Brown, J.C. 1976, Astron and Astrophys., 49, 239.

Culhane, J.L., Vesecky, J.F. and Phillips, K.J.H. 1970, Sol. Phys., 15, 394.

De, B.R. 1973, Sol. Phys., 31, 437.

Defouw, R.J. 1970a, Ap. J., 160, 659.

_____. 1970b, Ap. J., 161, 55.

_____. 1970c, Sol. Phys., 14, 42.

Dere, K.P., Horan, D.M. and Kreplin, R.W. 1974, Sol. Phys., 36, 549.

Dodson, H.W. 1961, Proc. Nat. Acad. Sci., 47, 901.

Field, G.B. 1965, Ap. J., 142, 531.

Fisher, R.R. 1971, Sol. Phys., 19, 440.

_____. 1974, Sol. Phys., 35, 401.

Goldsmith, D.W. 1970, Ap. J., 161, 41.

_____. 1971, Sol. Phys., 19, 86.

Harvey, J., Livingston, W. and Slaughter, C. 1972, "Proc. Conf. on Line Formation in a Magnetic Field", Boulder, Colo., Sept., 227.

Hirayama, T. 1972, Sol. Phys., 24, 310.

Horan, D.M. 1971, Sol. Phys., 21, 188.

Hudson, H.S. and Okhi, K. 1972, Sol. Phys., 23, 155.

Hunter, J.H., Jr. 1970, Ap. J., 161, 451.

Hyder, C.L. 1964, Ap. J., 140, 817.

Jackson, J.D. 1962, Classical Electrodynamics (New York: John Wiley and Sons, Inc.).

Jefferies, J.T. and Orrall, F.Q. 1961, Ap. J., 133, 963.

_____. 1965a, Ap. J., 141, 505.

_____. 1965b, Ap. J., 141, 519.

Kahler, S.W., Meekins, J.F., Kreplin, R.W. and Bowyer, C.S. 1970, Ap. J., 162, 293.

Kahler, S.W., Krieger, A.S. and Vaiana, G.S. 1975, Ap. J. Letters, 199, L57.

Karzas, W.T. and Latter, R. 1961, Ap. J. Suppl., 6, 167.

Kleczek, J. 1958, Bull. Astron. Inst. Czeck., 9, 115.

Lust, R. and Zirin, H. 1960, Z. Astrophys., 49, 8.

McCabe, M. 1973, Sol. Phys., 30, 439.

Moore, R.L. 1972, Stanford University, Institute for Plasma Research Report No. 463, March.

Moore, R.L. and Datlowe, D.W. 1975, Sol. Phys., 43, 189.

Moore, R.L. and Fung, P.C.W. 1972, Sol. Phys., 23, 78.

Morse, P.M. and Feshback, H. 1953, Methods of Theoretical Physics (New York: McGraw-Hill).

Neupert, W.M. 1968, Ap. J. Letters, 153, L59.

Neupert, W.M., Thomas, R.J. and Chapman, R.D. 1974, Sol. Phys., 34, 349.

Olson, C.A. and Lykoudis, P.S. 1967, Ap. J., 150, 303.

Pallavicini, R., Vaiana, G.S., Kahler, S.W. and Krieger, A.S. 1975, Sol. Phys., 45, 411.

Parker, E.N. 1953, Ap. J., 117, 431.

Petrosian, V. 1973, Ap. J., 186, 291.

Raymond, J.C., Cox, D.P. and Smith B.W. 1976, Ap. J., 204, 290.

Richtmyer, R.D. and Morton, K.W. 1967, Difference Methods for Initial-Value Problems, Second Edition, (New York: Interscience Publishers) Chapter 12.

Roy, J.R. 1972, Sol. Phys., 26, 418.

Rust, D.M. and Roy, J.R. 1971, IAU Symposium 43, 569.

Rust, D.M. and Bar, V. 1973, Sol. Phys., 33, 445.

Shklovskii, I.S. 1965, Physics of the Solar Corona, Second Edition, (Oxford: Pergamon Press), p. 411.

Spitzer, L. 1962, Physics of Fully Ionized Gases (New York: Wiley Interscience), Chapter 5.

Strauss, F.M. and Papagiannis, M.D. 1971, Ap. J., 164, 369.

Sturrock, P.A. 1968, Proc. IAU Symposium 35, "Structure and Evolution of Solar Active Regions", (Dordrecht: Reidel Publishing Co.), p. 471.

_____. 1973, Proc. Symposium on High Energy Phenomena on the Sun, Greenbelt, Maryland, Goddard Space Flight Center, March.

Svestka, Z. 1968, IAU Symposium 35, 287.

_____. 1976, Solar Flares (Dordrecht: Reidel Publishing Co.).

Tandberg-Hanssen, E. 1967, Solar Activity (Waltham, Mass: Blaisdell Publishing Co.).

_____. 1974, Solar Prominences (Dordrecht: Reidel Publishing Co.).

Teske, R.G. 1971, Sol. Phys., 17, 76.

Thomas, R.J. and Teske, R.G. 1971, Sol. Phys., 16, 431.

Thomas, R.N. and Athay, R.G. 1961, Physics of the Solar Chromosphere (New York: Interscience), p. 142.

Tucker, W.H. and Koren, M. 1971, Ap. J., 168, 283.

Vorpahl, J.A., Gibson, E.G., Landecker, V.B., McKenzie, D.L. and Underwood, J.H. 1975, Sol. Phys., 45, 199.

Waldmeier, M. 1973, Sol. Phys., 30, 129.

Weymann, R. 1960, Ap. J., 132, 452.

Zauman, W.T. and Acton, L.W. 1974, Sol. Phys., 36, 139.

Zirin, H. 1961, Soviet Astr.-AJ., 5, 660.

SECURITY CLASSIFICATION OF THIS PAGE (When Data Entered)

REPORT DOCUMENTATION PAGE

READ INSTRUCTIONS BEFORE COMPLETING FORM

1. REPORT NUMBER: SUIPR Report No. 679
2. GOVT ACCESSION NO.:
3. RECIPIENT'S CATALOG NUMBER:

4. TITLE (and Subtitle): THERMAL INSTABILITY IN POST-FLARE PLASMAS

5. TYPE OF REPORT & PERIOD COVERED: Scientific, Technical

6. PERFORMING ORG. REPORT NUMBER:

7. AUTHOR(s): Spiro K. Antiochos

8. CONTRACT OR GRANT NUMBER(s): N00014-75-C-0673

9. PERFORMING ORGANIZATION NAME AND ADDRESS:
Institute for Plasma Research
Stanford University
Stanford, California 94305

10. PROGRAM ELEMENT, PROJECT, TASK AREA & WORK UNIT NUMBERS:

11. CONTROLLING OFFICE NAME AND ADDRESS:
Phil Surra, Office of Naval Research
Durand 165, Stanford University

12. REPORT DATE: December 1976

13. NO. OF PAGES: 111

14. MONITORING AGENCY NAME & ADDRESS (if diff. from Controlling Office):

15. SECURITY CLASS. (of this report): UNCLASSIFIED

15a. DECLASSIFICATION/DOWNGRADING SCHEDULE:

16. DISTRIBUTION STATEMENT (of this report)
This document has been approved for public release and sale; its distribution is unlimited.

17. DISTRIBUTION STATEMENT (of the abstract entered in Block 20, if different from report)

18. SUPPLEMENTARY NOTES

19. KEY WORDS (Continue on reverse side if necessary and identify by block number)
Solar Activity, Thermal Instability, Flare Cooling

20. ABSTRACT (Continue on reverse side if necessary and identify by block number)

Satellite x-ray observations indicate that most solar flares produce a hot, ~~$\geq 10^7$ K,~~ dense plasma high up in the sun's corona. ~~We~~ It is believed that this gas originates from lower regions of the atmosphere, specifically the chromosphere, where it is heated by a flare and evaporated into the corona. Optical observations have shown that the post-flare plasma does not cool uniformly rather, small cold condensations form at the top of magnetic field arches while the bulk of the plasma remains at high temperature. Loop Prominence Systems are an example of this phenomenon. Dynamical processes connected with the → next page

DD FORM 1 JAN 73 1473
EDITION OF 1 NOV 65 IS OBSOLETE

UNCLASSIFIED
SECURITY CLASSIFICATION OF THIS PAGE (When Data Entered)

19. KEY WORDS (Continued)

20 ABSTRACT (Continued)

flare event have been proposed as a mechanism for these types of active prominences. This report ~~We have~~ investigated the cooling of post-flare plasmas, and attempted to explain the formation of loop prominences as due to a thermal instability. At certain temperatures ~~between 10^5 to 10^7 K,~~ the solar plasma is known to be unstable to thermal perturbations because the radiation losses of this gas increase with decreasing temperature. A simple perturbation analysis is insufficient to account for the evolution of the solar plasma, because observed differences of temperature and density exceed an order of magnitude. Additionally, the plasma is always in a non-equilibrium state, so that, we must solve numerically the equations of motion and heat transfer.

~~We have developed~~ a one-dimensional model is developed for active loop prominences. Magnetic fields present in post-flare regions are strong enough to dominate the plasma; hence, only motion and heat fluxes parallel to the field need to be considered. The relevant size scales and time scales are such that single-fluid MHD equations are valid. ~~We have included in~~ the model includes the effects of gravity, the geometry of the field and conduction losses to the chromosphere. A computer code for the solution of our set of equations has been constructed. Basically, we treat the system as an initial value problem (with certain boundary conditions at the chromosphere-corona transition region), and use a two-step time differencing scheme.

Our calculations indicate that the thermal instability mechanism is, by itself, sufficient to account for the behavior of active loop prominences. Under certain conditions, initial perturbations in the temperature and density profiles of small amplitude ($\leq 5\%$) and large size scale ($\geq 2 \times 10^9$ cm.) can grow into condensations with temperature and density differences of over an order of magnitude and size scales of less than 10^8 cm. In agreement with observations, the conditions that must be satisfied are such that Loop Prominence Systems are likely to occur only in large flares. The velocities, densities, and lifetimes that we obtain for the loop material are also in agreement with observations.

From ~~our~~ the results ~~we~~ it is concluded that the non-uniform cooling of the post-flare corona can be understood as a direct consequence of the temperature and density dependence of the radiative losses from a high-temperature solar plasma.